

Formation of Intermetallic Phases in Al-10Si-0.3Fe based Alloys

vorgelegt von

Master of Engineering

Jiamin Yu

von der Fakultät III - Prozesswissenschaften
der Technischen Universität Berlin
zur Erlangung des akademischen Grades

Doktor der Ingenieurwissenschaften

-Dr.-Ing.-

genehmigte Dissertation

angefertigt am Helmholtz-Zentrum Berlin für Materialien und Energie
Institut für Angewandte Materialforschung

Promotionsausschuss:

Vorsitzender: Prof. Dr. -Ing. Walter Reimers

Berichter: Prof. Dr. rer. nat. John Banhart

Berichter: Prof. Dr. rer. nat. Dieter Herlach

Tag der wissenschaftlichen Aussprache: 16 December 2016

Berlin 2016

献给我最挚爱的父亲母亲

To my beloved parents

Abstract

The emphasis of the work lies on finding out how impurities and the addition of Sr influence the formation of Fe-rich intermetallic phases and the formation of the eutectic Si phase in Al-Si casting alloys. A further objective of this study was the understanding of the influence of the cooling rate on the formation of intermetallic phases. For this purpose, four Al-10Si-0.3Fe-based casting alloys (high-purity alloy with and without addition of 200 ppm Sr and corresponding commercial alloys) have been chosen for this study. The experimental work was focused on the three-dimensional analysis of Fe-rich intermetallic phases using tomographic methods on the micrometer scale such as serial slicing with a Focused Ion Beam and Scanning Electron Microscopy imaging as well as synchrotron X-ray tomography. The three-dimensional analyses were supported by two-dimensional studies using a combination of optical microscopy, scanning electron microscopy and transmission electron microscopy.

Besides the well-known phases, i.e. the α intermetallic phase, the tetragonal δ phase and the β phase, **a new γ phase** was found. The composition of the γ phase is $\text{Al}_{4.35}\text{FeSi}$, which is close to that of the β phase ($\text{Al}_{4.5}\text{FeSi}$), but the morphology of the γ phase looks like the one of the α intermetallic phase. It features a trigonal R-centered crystal structure with hexagonal lattice parameters $a = 1.034(5)$ nm, $c = 1.983(8)$ nm and $V = 1.836(25)$ nm³.

The α intermetallic phase is dominant in the high-purity alloy, while in the modified alloy Sr promotes the formation of the δ phase. Additionally, Sr was found to suppress the formation of the β phase in the commercial alloy.

Impurities play an effective role in the nucleation of the eutectic grains, which lead to an advantage for the formation of the coarse β phase.

Cooling conditions influence the formation of intermetallics. Their formation is suppressed and refined during fast solidification. In contrast, a slow cooling rate promotes the formation of the coarse β phase.

Focused Ion Beam tomography and synchrotron X-ray tomography have been used to characterize the three-dimensional morphologies, the locations and the volume fractions of the intermetallic phases formed in each investigated alloy.

In-situ synchrotron X-ray tomography allowed for the observation of phase separation from the melt during solidification in real time. The nucleation of β and δ phases was observed

Abstract

and the phase solidification sequence has been clarified. β plates nucleate on or near the dendrite whereas the δ phase was observed to nucleate on the eutectic Si.

Contents

Abstract	I
Contents	III
1 Introduction	1
2 Background	5
2.1 Binary Al-Si alloy system.....	5
2.2 Ternary Al-Si-Fe alloy system.....	6
2.3 Formation of eutectic microstructure and intermetallic phases	8
2.3.1 α intermetallic phase	12
2.3.2 β intermetallic phase	14
2.3.3 δ intermetallic phase	16
2.4 Effect of Sr on the eutectic microstructure and the intermetallic phases.....	17
3 Materials	21
4 Experimental methods	23
4.1 Optical Microscopy.....	23
4.2 Scanning Electron Microscopy	24
4.3 Transmission Electron Microscopy	25
4.3.1 TEM system.....	26
4.3.2 Sample preparation	27
4.4 Focused Ion Beam	27
4.4.1 FIB system	27
4.4.2 Data processing.....	29
4.5 Synchrotron X-ray Tomography.....	31
4.5.1 Synchrotron system.....	32
4.5.2 Synchrotron X-ray tomography beamline	34
4.5.3 Sample measurement	35

Contents

4.5.4 Data processing.....	37
5 Results.....	39
5.1 Microstructure characterization	39
5.1.1 Optical microscopy.....	39
5.1.2 Scanning Electron Microscopy.....	41
5.1.3 Transmission Electron Microscopy	44
5.2 Three-dimensional visualization of intermetallic phases (ex-situ tomography).....	56
5.2.1 Unmodified high-purity alloy (FIB tomography).....	56
5.2.2 Sr-modified high-purity alloy (FIB tomography).....	58
5.2.3 Sr-modified commercial alloy (FIB tomography).....	61
5.2.4 Summary (FIB tomography).....	64
5.2.5 Synchrotron tomography	66
5.3 Three-dimensional visualization of intermetallic phases (in-situ tomography)	69
5.3.1 Phase separation in the unmodified commercial alloy	72
5.3.2 Evolution of β - and δ -intermetallics	75
6 Discussion.....	85
6.1 In-situ synchrotron tomography / slow cooling.....	85
6.1.1 Effect of slow solidification on microstructure	85
6.1.2 Nucleation and growth of the Fe-rich intermetallic β phase.....	88
6.1.3 Nucleation and growth of the Fe-rich intermetallic δ phase.....	93
6.2 Ex-situ observations of the microstructure in the as-cast alloys / fast cooling.....	97
6.2.1 Effect of Sr on Al-10Si-0.3Fe-based alloy	97
6.2.2 Effect of impurities on Al-10Si-0.3Fe-based alloys	99
6.2.3 Formation of α and γ intermetallics	100
6.2.4 Formation of δ intermetallics.....	101
6.2.5 Formation of β intermetallics.....	102
6.3 Effect of cooling rates on the formation of the intermetallic phases	102
7 Summary.....	105

References	111
Acknowledgements	121
Declaration	123

1. Introduction

Al-Si alloys are widely used for making automotive and aerospace components because of their low weight and good mechanical and processing properties [1, 2]. Commercial Al-Si alloys always contain some amounts of Fe as a natural impurity, which cannot be removed from the primary aluminium metal in a cost efficient way. Iron tends to precipitate in combination with other elements during solidification, forming complex intermetallic phases of various types [3-5]. These intermetallic phases can markedly degrade the mechanical properties and give rise to casting defects [3, 6]. More than twenty types of Fe-containing intermetallic phases with different compositions and crystal structures, including at least twelve types of stable ternary intermetallics, have been identified [7-9]. The most common intermetallic Al-Si-Fe-phases are α , β and δ , which differ by their chemical composition and their morphology. Their formation path also differs and depends on the amount of Fe, the cooling rate during solidification, other impurities in the alloys and additions of further transition elements. Transition elements are always present in the commercial Al-Si alloys and are partly responsible for the observed diversity of intermetallics.

The most commonly occurring intermetallic phase is α -Al₈Fe₂Si. It has been identified as either bcc [10, 11] or as a hexagonal structure [12, 13]. All of these α -phases are characterized by the so-called “Chinese script” morphology in two dimensions (2D). In addition, some researchers reported a phase α -Al₁₅(Fe,Mn)₃Si₂, showing a compact blocky shape and appearing as polyhedral crystals [14]. Many different compositions of α -phases in the stable ternary and quaternary systems have been reported [15-18].

The second type of phase is the Fe-rich δ -phase. Depending on its orientation in the transmission electron microscope (TEM) foil the Fe-rich δ -phase (Al₄FeSi₂), also termed Al₃FeSi₂ [10, 19], exhibits a lath or an acicular shape in two dimensions. In three dimensions (3D) the phases are plates or blades. It has been reported that the δ -phase has a tetragonal PdGa₅-type structure [19] or an orthorhombic structure with a pseudo-tetragonal cell [20].

The last common Fe-rich intermetallic phase is the β phase, which has often been designated as Al_{4.5}FeSi [21, 22] with needle-like or acicular morphology in two dimensions and inter-

1 Introduction

connected plates or blades in three dimensions. It has been found that this phase has a monoclinic structure [21]. However, the β phase sometimes comes with a tetragonal [23], B-centered orthorhombic [24], or A-centered orthorhombic [17] structure in multiphase composites.

The β phase is the most studied phase. Many attempts have been made to prevent the formation of the coarse brittle β phase or to neutralize the negative effect on casting porosity, castability and mechanical properties. While the negative effects of the Fe-rich β -phase are well known, its nucleation and growth is still under discussion. Many mechanisms have been proposed for nucleation and sometimes there are contradictory results. Campbell et al. [25, 26] suggested that nucleation and growth of the Fe-rich β phase take place on the external oxide films. Samuel et al. [27] found that P or AlP particles serve as nuclei of the β phase. Lu and Dahle [28] investigated the interaction between transition elements like Mn, Cr, Be, Ni, Mg, P and Fe and their influence on the nucleation of the Fe-rich intermetallic phases. They found that neither the addition of P increases the number of the β plates, nor do AlP particles serve as nuclei of the β phase.

Beside the impurities the solidification cooling rate plays an important role for the formation of Fe-rich intermetallic phases. An influence of the Si and Fe content on the formation of Fe-rich intermetallic phases at different cooling rates is reported in Ref. [29]. The β phase has been obtained at a cooling rate < 1 K/min and an amount of Fe 0.25 wt. % and is independent of the Si content. An increase of the cooling rate to > 6 K/min leads to the formation of the β and additionally the α phase. Finally, at cooling rates > 9 K/min the α phase is the only phase that forms.

To overcome the negative effect caused by β intermetallic phases some researchers [3, 30] proposed to add traces of transition elements such as Mn, Cr, Cu or Co, which can neutralize the embrittlement of alloys and promote the formation of the α phase with a compact morphology. For commercial applications, elements such as Sr or Na are always added to Al-Si alloys prior to casting to improve their mechanical properties by modifying the eutectic Si phase. It has been found that the addition of Sr to the Al-Si alloys positively influences the volume fraction as well as the size of the Fe-rich intermetallic phases [26-28, 31]. The influence of Sr on the formation of intermetallic phases, however, is still under debate [28, 32, 33].

The visualization of the microstructure and the phases has long been possible only with microscopic methods (optical microscopy (OM), scanning electron microscopy (SEM) and

TEM). More recent studies have used tomographic methods to investigate the microstructure of the eutectic Si as well as the Fe-rich intermetallic phases on a μm scale. Ex-situ investigations of unmodified and Sr-modified eutectic microstructures of as-cast Al-Si alloys were usually performed by Focused Ion Beam (FIB) tomography [10, 34-38]. The complete microstructure in Al-Si alloys, the morphology of the eutectic Si phase and the real morphology of Fe-rich intermetallic phases was clearly visualized. However, the nucleation and growth of Fe-rich β intermetallic phases could only be observed by in-situ X-ray tomography [39-42]. To clearly follow the nucleation and growth process of all phases a huge number of pictures and a longer experimental time is required. Therefore, the melt has to be cooled very slowly during solidification. The results of in-situ X-ray measurements published in Ref.'s [39-42] describe only the formation of the β intermetallic phase. However, the cooling rate during solidification of in-situ experiments is not high enough to compare the microstructure with that obtained under industrial conditions. The cooling rate used in the in-situ experiments was either $1.4^\circ\text{C}/\text{min}$ [42] or lies between $3^\circ\text{C}/\text{min}$ and $20^\circ\text{C}/\text{min}$ [40], while the cooling rate of industrial castings is $\sim 400^\circ\text{C}/\text{min}$. As mentioned above the increase of the cooling rate results in the preferential formation of one or the other Fe-rich intermetallic phase.

In summary, from the knowledge of the nucleation and growth of Fe-rich intermetallic phases in Al-Si alloys we learn that every effect (impurities, modifier and cooling rate during solidification) must be examined separately.

For this purpose four alloys of different compositions are going to be compared, i.e. the well defined pure alloys Al-10Si-0.3Fe and Al-10Si-0.3Fe-200 ppm Sr and the two corresponding commercial alloys containing additional impurities such as Mn, Ni, Zn, Ga and P, etc. This will allow us to assess the influence of the modifier Sr and the commercial impurities on the precipitation sequence.

The overview of the microstructure, the location of the intermetallic phases has been examined by OM and SEM on the mm or the μm scale. The structure and the chemical composition of the intermetallic phases were determined by diffraction in the TEM and energy dispersive X-ray (EDX) spectroscopy, respectively. The characterization of the microstructure and their results obtained by OM, SEM and TEM are presented in chapter 5.1.

The morphology of the eutectic Si and the intermetallic phases in the pure unmodified as well as in the modified alloys and the corresponding commercial alloys was investigated in three dimensions by FIB tomography. At much larger scales of ~ 1 mm ex-situ synchrotron

1 Introduction

tomography measurements have also been carried out on all casting alloys. The results obtained from ex-situ tomographic measurements are illustrated in chapter 5.2.

To understand the nucleation and growth of the Fe-rich intermetallic phases in Al-10Si-0.3Fe casting alloys during phase separation from the melt, in-situ X-ray microtomography has been used for different solidification cooling rates. The present research was designed to compare the density, shape, location and connectivity of Fe-rich phases precipitating from the melt. The results of in-situ synchrotron tomography are shown in chapter 5.3.

Chapter 6 provides a discussion of the Fe-rich intermetallic phase formation influenced by the cooling rates, by the addition of Sr and by the impurities in Al-Si alloys. The microstructure development during phase separation is explained. Based on the three-dimensional tomographic measurements the mechanisms of phase nucleation can be discussed.

2. Background

This chapter provides the fundamental properties of the microstructure in the Al-Si based alloy system. Section 2.1 presents the structural components in the binary equilibrium phase diagram of Al-Si alloys. The formation of the stable phases will be presented as a function of the temperature and the composition. However, in practice, commercial Al-Si based alloy systems consist not only of two alloying elements, but they include several additional elements or impurities which form intermetallic phases. Especially Fe plays the role of a natural impurity element. Section 2.2 shows the isothermal section of the ternary Al-Si-Fe equilibrium phase diagram obtained at 600°C. The ternary diagram describes the existence areas of all possible Fe-rich intermetallic phases. Section 2.3 schematically presents the nucleation and growth process of Al-Si eutectic phases based on the temperature profile during the eutectic solidification. In addition, the phase separation sequence including the formation of intermetallic phases will be explained. The existence of one or the other intermetallic phase depends not only on the composition of the alloy (Si content, amount of impurities like Fe) but also on the cooling rate of the melt, and will be presented in Section 2.4. The influence of Sr addition on the eutectic solidification will be discussed in Section 2.5.

2.1 Binary Al-Si alloy system

The Al-Si binary system is a simple eutectic system with two solid solution phases, i.e. fcc (Al) and diamond cubic (Si). The phase diagram shown in Fig. 2.1 [43] is mainly calculated from the Gibbs energies of the phases based on the equilibrium state. It displays the formation condition of the stable phases in the binary system in dependence of the temperature and composition.

There is a eutectic point at 12.5 wt. % Si at which only eutectic Si and eutectic Al can form when the temperature is decreasing. In the hypoeutectic Al-Si alloy, there is formation of primary Al dendrites and then eutectic Si and eutectic Al phases. In the hypereutectic Al-Si alloy there is formation of primary Si and then eutectic Si and eutectic Al. The temperature

2 Background

at 577 °C is called the eutectic temperature, at which eutectic Al-Si crystallizes from the melt and separates into two phases. In summary, during equilibrium solidification the Al-Si liquid solidifies and crystallizes along the liquidus-solidus line and the eutectic line. Primary Al dendrite/primary Si and eutectic Al-Si are separated.

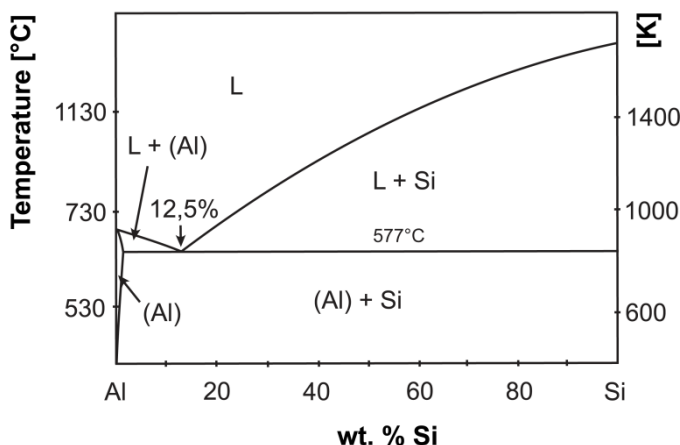


Fig. 2.1 Binary Al-Si phase diagram [43].

The solubility of Si in Al decreases sharply with decreasing temperature, and almost no solubility of Si in Al is to be expected at room temperature. At the other end of the phase diagram, Al is practically insoluble in Si.

2.2 Ternary Al-Si-Fe alloy system

Commercial Al-Si alloys always contain some Fe as natural impurity. Sometimes Fe is also added on purpose as an additional alloying element in certain Al-Si alloys [14]. Therefore it is necessary to understand the ternary Al-Si-Fe system before the examination of the formation of Fe-rich intermetallic phases.

The ternary Al-Si-Fe system shown in Fig. 2.2 is characterized by a large number of ternary and, considering the impurities, also quaternary intermetallic phases. Due to its low solubility in the solid alloy, Fe tends to precipitate in combination with other elements during solidification. It forms complex intermetallic phases of various types, both stable and metastable. At least twenty invariant Fe-containing intermetallics can form during solidification, which leads to difficulties in establishing the phase equilibrium of the system [44-47]. Several nomenclatures were proposed to try to unify the name for these

intermetallic phases, such as Greek alphabet letters: α , β , δ ..., or letters τ_i ($i = 1, 2, 3, \dots$) [44-50].

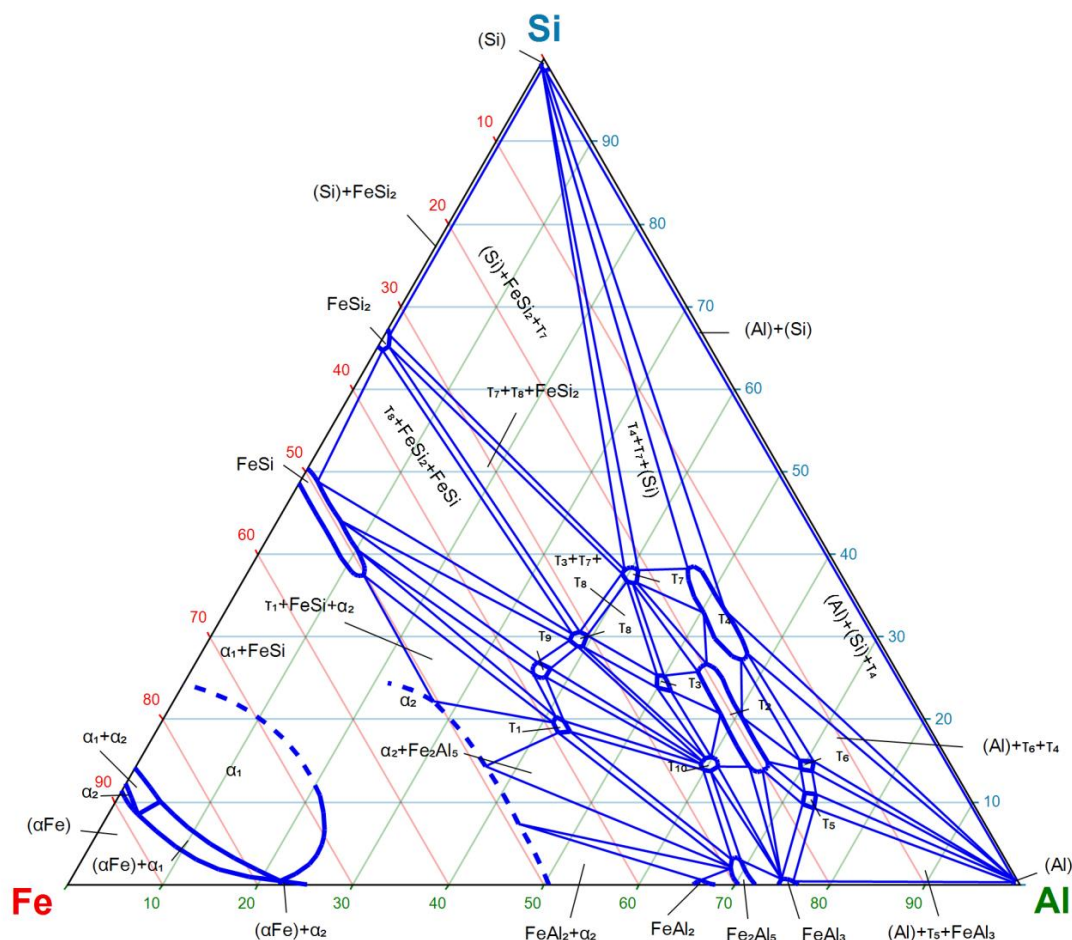


Fig. 2.2 Isothermal section of the Al-Fe-Si system at 600°C, scale in at.% [51]

Fig. 2.2 shows the isothermal section of the Al-Fe-Si system at 600°C [51] and illustrates that, at low concentrations of Fe, τ_6 (β -AlFeSi), τ_5 (α -AlFeSi), τ_4 (δ -AlFeSi) and θ -Al₃Fe can form in the hypoeutectic Al-Si alloy. The most detrimental phase of all intermetallics is the τ_6 (β -Al₅FeSi) phase. Even small amounts of Fe in the alloy lead to the formation of the τ_6 (β -Al₅FeSi) phase; their size and density increases with the Fe content. Furthermore, the critical Fe level is directly related to the Si concentration in the alloy, as can be seen from the section of the liquidus projection of the ternary Al-Si-Fe phase diagram for Al-rich alloy as shown in Fig. 2.3 [14]. The critical Fe level is marked by the dashed red line. An increase of the Si amount increases the critical level. For example, for the present alloy with 10 wt. % Si (blue dashed line) the critical Fe level reaches ~ 0.7 wt.%. The formation temperature of the β phase (called v-v' line in the present work), prior to the Al/Si eutectic, also decreases with the Si content as can be seen from the Fig. 2.3.

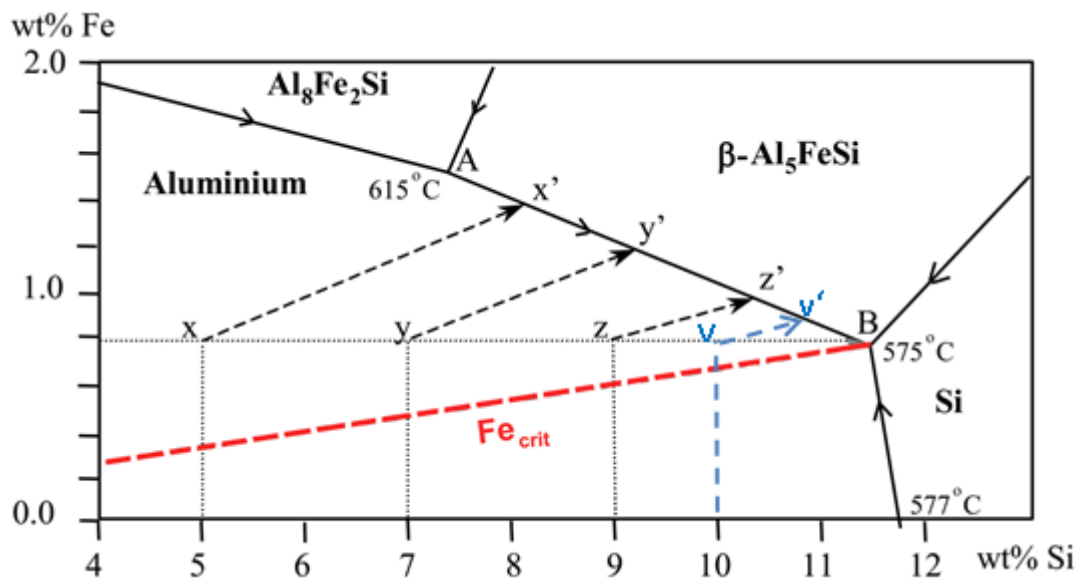


Fig. 2.3 Simplified liquidus projection of the ternary Al-Si-Fe system, showing the Al solidification paths (using Scheil assumptions) for alloys with Fe_{crit} iron levels (red dashed line). The points of intersection with the AB line are where the formation of large β phase platelets starts to occur prior to the formation of the ternary eutectic at B [14]. The dashed blue line corresponds to the Si content of the present alloy.

2.3 Formation of eutectic microstructure and intermetallic phases

Eutectic Al-Si is very important for the determination of the mechanical properties of Al-Si foundry alloys. The composition of the most Al-Si casting alloys is in the vicinity of the eutectic point, in order to take full advantage of its excellent castability. The Al-Si eutectic of such alloys often amounts to more than 50 vol. % of the microstructure. Furthermore, the formation of the eutectic is generally completed at the final stage of solidification process. It is expected that the eutectic significantly influences the formation of casting defects, particularly porosity. Moreover, formation and growth of the eutectic phases have a huge impact on the formation of intermetallic compounds. Therefore, the understanding of the formation of the eutectic is very important.

Eutectic solidification of unmodified Al-Si alloys takes place in two sequential stages: nucleation and growth. Fig. 2.4a schematically illustrates the process of nucleation and growth of spherical eutectic grains during cooling, using the eutectic solidification temperature curve [52, 53]. Under non-equilibrium conditions, a eutectic grain nucleates at

the beginning of eutectic solidification (time $t = t_N$; temperature $T = T_N$) and grows until the end of eutectic solidification ($t = t_E$; $T = T_E$), as shown in Fig. 2.4a. In order to achieve the critical nucleus size an undercooling of the melt is required. Nucleation begins at a temperature (T_N) below the eutectic equilibrium temperature T_{eq} . The nucleation temperature is determined by the nuclei distribution and the cooling conditions (e.g. the heat release rate). It is assumed that during the progressing undercooling new crystallization nuclei are formed continuously [52, 54]. In the temperature interval $T_N \leq T \leq T_M$ (marked in red in Fig. 2.4a) there is a continuous formation of potential crystallization nuclei during the steady decrease in temperature, along with the growth of already existing nuclei. In this interval nucleation and growth of the eutectic grains occurs at the same time, until the minimum temperature prior to recalescence (t_M, T_M) is reached. After reaching T_M there is no further nucleation.

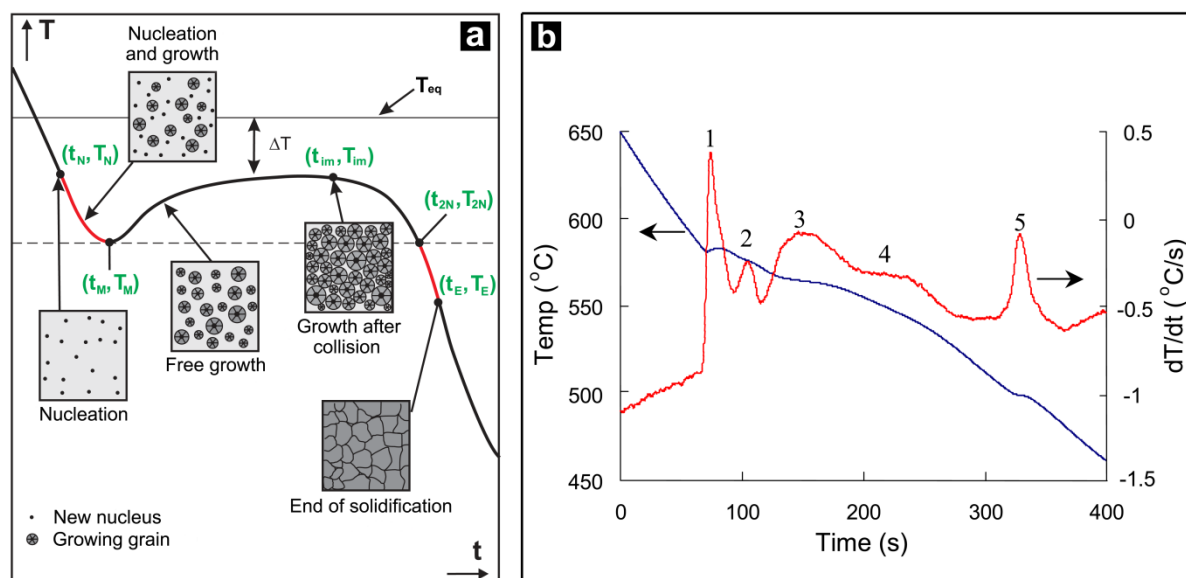


Fig. 2.4 (a) Schematic temperature profile of the typical cooling curve in Al-Si alloy with eutectic composition. It shows the nucleation and spherical growth of the eutectic grains during solidification [52]. The indices of the temperature T at time t_i refer to: T_N = nucleation temperature; T_M = minimum temperature prior to recalescence; T_{in} = the beginning of the collision of grains; T_{2N} = start of secondary nucleation. T_E = end of the eutectic solidification. ΔT corresponds to the sub-cooling of the melt in relation to the eutectic equilibrium temperature T_{eq} . (b) Typical phase separation sequence during solidification of Al-9Si-3Cu-0.5Mg-1.0Fe alloy: (1) primary Al dendrites; (2) β -Al₅FeSi; (3) Al-Si eutectic; (4) complex Mg₂Si eutectic; (5) complex Al₂Cu eutectic [14].

2 Background

However, the growth of the eutectic grain continues, called “free growth” in Fig 2.4a. This is because of an equilibrium at T_M : the generating rate of latent heat is equal to the heat release rate. Eutectic solidification starts at that moment, till T_{eq} . The eutectic grains continue to grow down to T_{2N} , where recalescence ends. The eutectic solidification is finally completed in the temperature region from T_{2N} to T_F .

The morphology of the eutectic Si phase within the eutectic grains can vary, i.e. it can form coarsened and refined morphologies [55, 56]. The changing of the morphology is primarily due to the change of the growth speed of the eutectic solidification front (s-l boundary surface) during solidification of the entire system [55]. According to a postulate in Ref. [56] the maximum attainable eutectic grain radius may be smaller if a grain nucleates after the t_N temperature or ceases to growth before t_E , i.e. fast solidification.

Fig. 2.4b illustrates the typical phase separation sequence during solidification (from 650°C to 450°C) of the Al-9Si-3Cu-0.5Mg-1.0Fe alloy, during which primary Al dendrites (peak 1), then β -Al₅FeSi phase form (peak 2) prior to the solidification of Al-Si eutectic while Al dendrites are still growing [14]. Peak 3 corresponds to the Al-Si eutectic. In this special alloy with high amounts of Cu and Mg there is formation of a complex Mg₂Si eutectic at peak 4 and a complex Al₂Cu eutectic at peak 5 [14]. In the present alloy peaks 4 and 5 are not expected to appear because of the low content of impurity elements.

Generally, intermetallic particles that form prior to or at the same time as solidification of the Al dendritic phase are relatively large. Particles that form much later, i.e. during or after the period of Al-Si eutectic solidification, are comparatively smaller because there is less liquid space available for growth during later stages.

As mentioned above, the Al-Si-Fe system is characterized by a large number of complex intermetallic phases, which differ by chemical composition, morphology and crystal structure. However, the frequently occurring intermetallic phases in Al-Si alloys are α , β and δ . The various morphologies of the different intermetallics are partly responsible for the impact of iron on castability and mechanical properties. The formation path of intermetallic phases is different and depends, on the one hand on the amount of Si and Fe, and on the cooling rate during solidification, on other impurities in the alloy, and on additions of further transition elements.

Detailed investigations of intermetallic phases existing in Al-xSi-0.25Fe alloys with different Si content and cooling rates have been reported in Ref. [29]. The intermetallics in Al-xSi-0.25Fe (x=2-12.5 wt%) are τ_5 (α -AlFeSi) and τ_6 (β -AlFeSi) phases. Their evolution at

several solidification cooling rates is shown in a schematic diagram in Fig 2.5. Based on the observations of the solidified microstructure it shows the conditions at which the intermetallic phases show up. Clearly the Si content and the cooling rate have a strong influence on the formation of either α -intermetallics or β -intermetallics along a critical band line, marked by a dashed line in the image. For Al-10%Si, the only β -intermetallic phase exists at cooling rates below 0.017 K/s, independently of the Si content. However, this phase

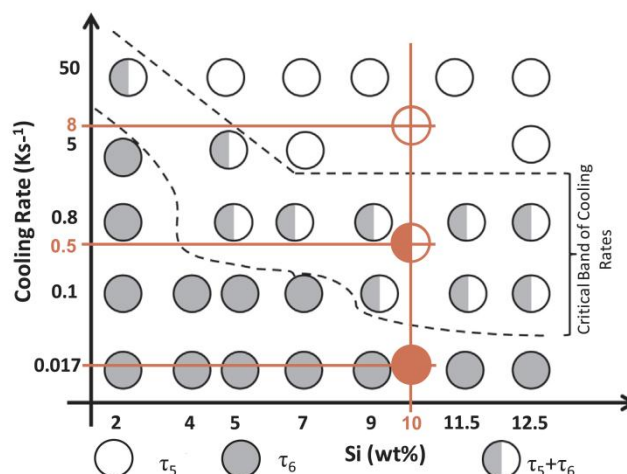


Fig. 2.5. Schematic diagram of the cooling rate as a function of the Si concentration demonstrating the existence of different types of intermetallic phases in Al-10Si-0.25Fe alloys, cooled from a temperature of about 1093 K (820 °C) after a melt holding time of 2 h. The band framed by the dotted line presents the conditions in which both the τ_5 (α -AlFeSi) and the τ_6 (β -AlFeSi) phases co-exist in the sample [29]. The alloy composition and the cooling rates used in the present work are marked in orange.

can also be obtained at much higher cooling rates but at low Si contents (i.e. at 2 wt. % Si). The area between the two dashed lines shows the existence of α - and β -intermetallic phases. Finally, the high cooling rate promotes only the formation of α -intermetallic phase (area above the dashed line). The δ - intermetallic phase has also been found in a similar alloy of composition Al-10Si-0.25Fe [19]. It has been proposed [5, 57] that the δ -intermetallic phase is dominant at a high Si content and a high cooling rate while β is dominant at a high Fe content and a low cooling rate. The increase of the cooling rate enhances the formation of intermetallic phases on some inclusions [33]. The combination of parameters (level of Si and Fe and cooling rate) determines the final microstructure which may contain the α phase, the β phase, the δ phase, or a combination of them. Low cooling rates result in larger sized

intermetallic phases whereas high cooling rates lead to a higher density of intermetallics and smaller sizes [5].

2.3.1 α intermetallic phase

It has been reported that the α phase exhibits many different compositions and structures in the stable ternary and quaternary systems [15-18]. The α -intermetallic phase was designated as α (FeSi) or c-AlFeSi and was attributed a cubic unit cell with $a=1.2578$ nm by earlier researchers [58, 59]. Almost at the same time Robinson et al. [60] almost found an α -AlFeSi intermetallic with a hexagonal unit cell and lattice parameters $a=1.23$ nm and $c=2.62$ nm.

Al-Si-Fe alloys containing Mn produce several α phases. Cooper [58] reported an α -Al₁₉Fe₄MnSi with space group $Im\bar{3}$ and a lattice parameter $a=1.256$ nm. Later, Kral [11] revised this composition to α -Al₁₉(Fe,Mn)₅Si₂ and another α -Al₁₅(Fe,Mn)₃Si₂ phase was reported in Ref. [61] with space group $Im\bar{3}$ and a lattice parameter $a=1.25$ nm.

The most common α -intermetallic phase is α -Al₈Fe₂Si, which has either been identified as body-centered cubic with space group $Im\bar{3}$ and a lattice parameter around $a = 1.25$ nm [10, 11] or as a hexagonal structure, space group $P6_3/mmc$, with lattice parameters around $a = 1.2404$ nm and $c = 2.6234$ nm [12, 13]. The α phases all exhibit the so-called "Chinese script" morphology in two dimensions. In addition, some researchers reported a phase α -Al₁₅(Fe,Mn)₃Si₂ showing a compact blocky shape and looking like polyhedral crystals [14]. It has been suggested that traces of transition elements such as manganese, chromium, copper or cobalt can promote the formation of the α phase [18, 62]. Such transition elements in Al-Si alloys are partly responsible for the observed diversity of intermetallics since they are always present in commercial alloys.

Recently, tomographic methods like FIB tomography or synchrotron X-ray tomography are increasingly used to visualize the morphology of intermetallic phases. One example of the morphology of α -AlFeSi intermetallic phase is displayed in Fig. 2.6 [10]: in two dimensions (SEM) it exhibits "Chinese script" and in three dimensions (FIB tomography) "thin sheets". The size of α phases was reported from several hundreds of nm to several millimeters depending on cooling rates and the Fe content as well as impurities contained in the alloy [14].

It has also been reported that the α phase can exhibit blocky structure and a convoluted branched structure in 3D [34]. Dinnis et al. [34] explain that this blocky structure of the α

phase forms before the Al dendrites begin to solidify while the convoluted branched structure of the α phase forms after the Al dendrites have begun to solidify. In addition, Gorny et al. [29] observed two distinct morphologies of the α phase, namely large phases

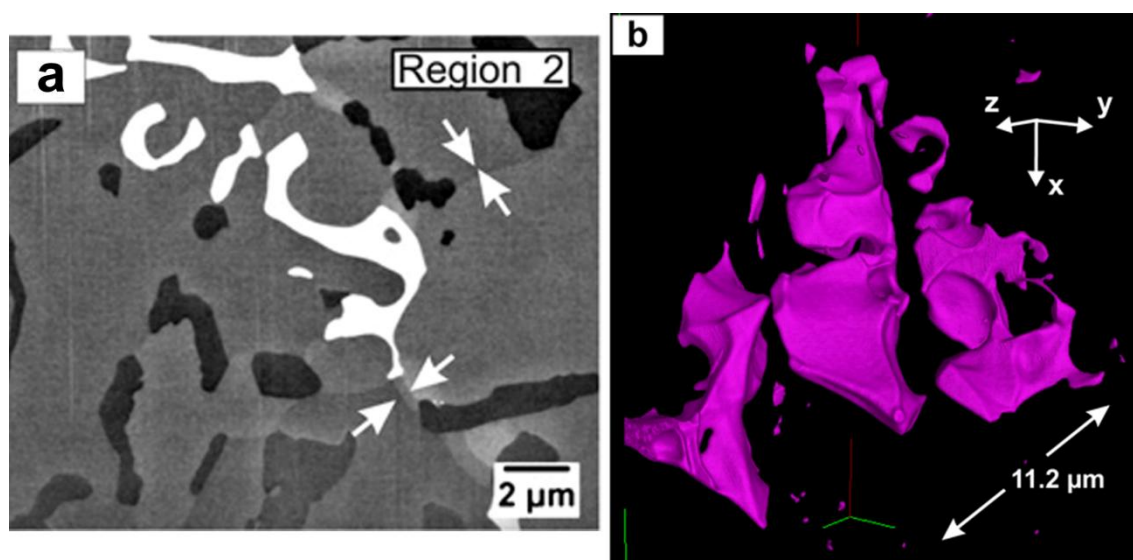


Fig. 2.6. The morphology of α -AlFeSi intermetallic phase visualized in a) 2D (α in bright white, imaged by the Zeiss InLens detector) [30]; and b) 3D (reconstruction based on FIB tomography; α in magenta) [10].

with a bulky morphology and a finer one with “Chinese script” morphology. Their explanation was that the large bulky morphology forms prior to the eutectic reaction and the finer with “Chinese script” morphology forms during the eutectic reaction. Based on the observation that the α phase exhibits thin sheets aligned along the surfaces of the Si plates and the eutectic Al grains, Timpel et al. [19] proposed that the α phase forms in isolated pockets among adjacent Al-Si eutectic during the last solidification stage. Their morphology therefore depends on the flat Si interface and on the growing polycrystalline eutectic Al–Al interfaces.

Furthermore, the formation of the α phase is also influenced by impurities and cooling rates. Cao et al. [62] reported that some oxides such as MgO, MgO·Al₂O₃, or α -Al₂O₃ might be good substrates for the nucleation of the α phase. Narayanan et al. [63] reported that in the presence of manganese, the simple α phase crystallizes at low cooling rates and the complex combination of α - and β - phases forms at high cooling rates.

2.3.2 β intermetallic phase

The β -Al₅FeSi intermetallic phase was first identified in an AlFeSi alloy by Rosenhain et al. [64]. The formation of β -Al₅FeSi intermetallic phase and its structure was of primary interest in many research studies. Rømming et al. [21] reported a monoclinic structure of the β -Al_{4.5}FeSi phase with lattice parameters $a=0.6161$ nm, $b=0.6175$ nm, $c=2.0813$ nm, and $\beta=90.42^\circ$ as determined by a combination of X-ray and electron diffraction. It was reported that the β phase contains faults and twins [17, 21, 22], which might be the reason why the β phase has such a variety of unit cell parameters. Hansen et al. [22] used the simplest fault model to describe why the anti-phase structure will destroy the monoclinic symmetry of the β phase and become triclinic with lattice parameters $a=0.61676$ nm, $b=0.61661$ nm, $c=2.08093$ nm, and $\beta=91^\circ$ (slightly different from the monoclinic structure). However, there were still some reports that the β phase sometimes exists as a tetragonal structure [23], a B-face centered orthorhombic [24], or even an A-centered orthorhombic structure in multiphase composites [21]. β -Al₅FeSi was often designated as Al_{4.5}FeSi or Al₉Fe₂Si₂ [22, 64].

The β -Al₅FeSi intermetallic phase is described as needle-like or having an acicular morphology in 2D, interconnected plates or blades in 3D, as can be seen in Fig. 2.7. β -Al₅FeSi is considered to be the intermetallic phase most detrimental to mechanical properties. Therefore the formation of this phase has been of primary interest for many researchers in the past decades. Sigworth and Campbell [65] proposed that the presence of phosphorus (P) in the melt leads to the nucleation of the β -intermetallic on an aluminium phosphide (AlP) nucleant. Cho et al. [66] also found the "P-rich particle" (probably AlP) that serves as nucleation spot for the β -intermetallic. Cao et al. [62] proposed a theory that β plates nucleate on the wetted surfaces of oxide bifilms, based on an observation of the central cracks of β plates. Miller et al. [67] deliberately added α -Al₂O₃ and MgAl₂O₄ oxide particles into the melt in order to verify the role of oxides in serving as nuclei for β -intermetallics. Their results suggested that the β -intermetallic is associated with both added oxides, which agrees with a previous hypothesis by Cao et al. [62]. Samuel et al. [68] and Narayanan et al. [63] reported that many fine β needles nucleate on γ -alumina, but γ -alumina turns to α -alumina when the melt is superheated above at 850°C. This confirms that α -alumina is a poor nucleus for β phase crystallization. Khalifa et al. [33] have extensively investigated the influence of inclusions (α -Al₂O₃, γ -Al₂O₃, MgO, CaO, TiC, TiB₂, etc.) on the nucleation of intermetallic phases. They found that nucleation of the intermetallics does not strongly depend on the types of inclusions. Rather the increase of the cooling rate enhances heterogeneous nucleation of intermetallic phases.

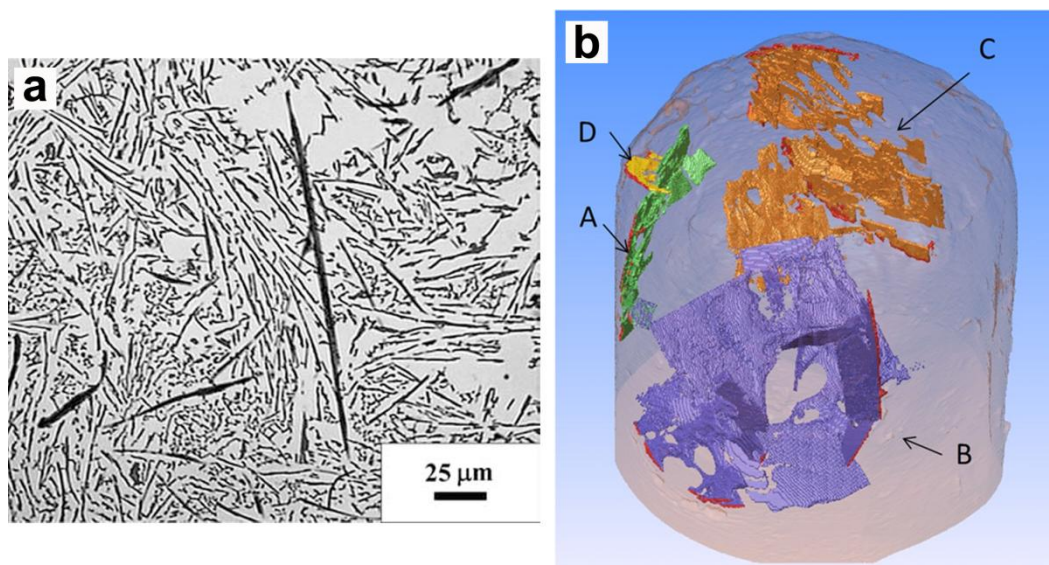


Fig. 2.7(a) β -AlFeSi intermetallic phase visualized in 2D (deep dark: blades) by SEM [67] and (b) three-dimensional visualization of β plates using in-situ synchrotron X-ray tomography (marks A, B, C and D indicate different separated plates) [42].

The answer to the question of nucleation of intermetallic phases cannot easily be found by only ex-situ investigations of final solidified microstructures. Therefore, recently in-situ X-ray radiography and synchrotron X-ray tomography have been performed to reveal the mechanism of intermetallics formation. Based on in-situ radiography observations, Kim et al. [69] observed that the β phase and the α -Al dendrite nucleate and grow together in the mode of a eutectic couple. It has been observed that β plates occur in the region between the arms of secondary α -Al dendrites in the supersaturated area of solute atoms. Terzi et al. [42] used in-situ synchrotron tomography to observe the formation process of β plates. Their conclusions are:

1. All β plates initiate at/near the outer oxide surface of the sample
2. Nucleation and growth of β plates is uncoupled with the nucleation and growth of α -Al dendrites
3. Some β plates form by growth and branching of existing plates. Branching of plates is observed to occur at various angles, i.e. high, medium, low and quasi-parallel. The occurrence and direction of branching appear to be dictated by physical obstruction of Al dendrite arms.

2 Background

4. β plates can grow around dendrite arms to a wide growth front after passing through.
5. A thickening of β plates can result in imprinted images on the surrounding dendrites being formed on their surface. Depressions and ridge lines marking adjacent dendrite arms can be observed.
6. The interaction between plates, dendrites and the outer oxide boundary can result in the formation of curved, bent, or fractured plates.

Puncreobutr et al. [40] observed four nucleation modes of the β phase:

1. Surface oxide nucleation (probably Al_2O_3)
2. On/near α -Al dendrites
3. Self-nucleation
4. Oxide skin of pores.

A quantification of all nucleation events demonstrated that the main mechanism of nucleation was on/near Al dendrites. Furthermore, the morphological texture indicates an orientation relationship of β plates growing parallel to the secondary dendrite arms. From the observation in [40] the authors proposed two types of plate interaction mechanisms: 1) impingement; 2) branching (new plates initiated at the existing plates, which is in agreement with the observations by Terzi et al. [42]).

2.3.3 δ intermetallic phase

The last and most common Fe-rich intermetallic phase in Al-Si-based alloys is δ - Al_4FeSi_2 or Al_3FeSi_2 [10, 19] which exhibits a needle-like or acicular morphology in 2D and plates or blades in 3D, similar to the β phase. It has been reported that δ has a PdGa_5 -type tetragonal structure with lattice parameters $a=0.615$ nm and $c=0.947$ nm [19]. Day et al. [20] re-determined the symmetry and proposed an orthorhombic structure with a pseudo-tetragonal cell $a=0.6061$ nm, $b=0.6061$ nm, and $c=0.9525$ nm and space group $Pbcn$.

It has been reported that the formation of the β phase is dominant at low cooling rates and high Si content, whereas the formation of the δ phase is dominant at high cooling rates and high Si content in the Al-Si-Fe system [33]. Choi et al. [57] investigated two hypereutectic types of Al-Si-Fe alloys with very high amounts of Fe. The alloys are Al-20Si-8Fe and Al-

30Si-5Fe. It has been found that in the Al-20Si-8Fe alloy at a relatively low cooling rate (0.17 K/s) the δ phase formed first, prior to primary Si precipitation. The remaining liquid solidified into an irregular ternary eutectic consisting of α -Al, Si and δ phase. In the Al-30Si-5Fe alloy the δ phase formed after primary Si precipitation, followed by the ternary eutectic α -Al, Si and δ phases. The ratio of Si to Fe played an important role in the formation of the δ phase. It has also been shown that the δ phase is meta-stable and transforms into equilibrium β phase with a monoclinic structure during further heat treatments. It was previously proposed that the δ phase can nucleate on oxide bifilms [62]. Khalifa et al. [33] investigated a series of inclusions that might be potent nucleation substrates. They found that the δ phase can nucleate on various different inclusions such as CaO, TiB₂, and α -Al₂O₃.

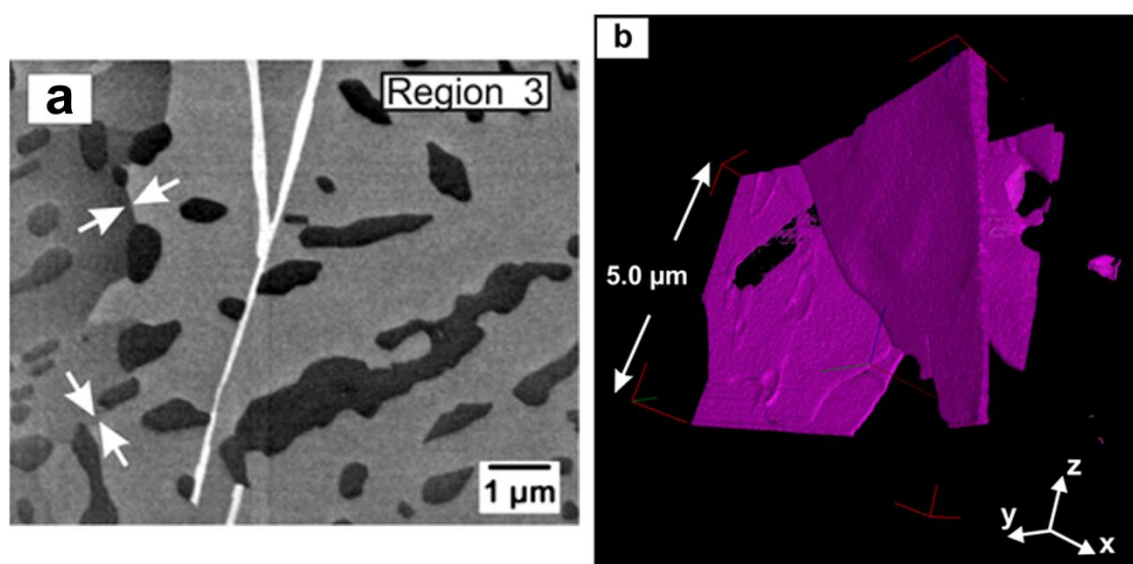


Fig. 2.8 The morphology of δ -AlFeSi intermetallic phase visualized in a) 2D (imaged by the Zeiss InLens detector; δ in bright white); and b) three-dimensional reconstruction using FIB tomography; δ in magenta) [10].

2.4 Effect of Sr on the eutectic microstructure and the intermetallic phases

Strontium is generally added as a trace element to commercial hypoeutectic Al-Si alloys in order to modify the eutectic Si morphology from coarse interconnected plates to fine fibrous and coral-like networks [36, 70, 71]. Even small amounts of Sr (100 ppm) change the mechanism of eutectic Si nucleation and growth and thus improve the strength and ductility

2 Background

of the final products. Modification of the eutectic microstructure has been investigated by many researchers for about 90 years. Only recently, the Sr modification effect was further explained by applying high resolution methods on the atomic scale. It has been found that it is intermetallic Sr-Al-Si co-segregation that inhibits and restricts growth of the eutectic Si phase [72-74], and not single Sr atoms as postulated in the past.

The modification effect of Sr, especially on the transformation of the eutectic microstructure, is extremely important. However, the knowledge of the Sr influence on the formation of Fe-rich intermetallic phases is equally important for industrial application. As mentioned earlier, the presence of intermetallic phases has deleterious effect on the mechanical properties and detrimentally impacts the castability of Al-Si alloys [3, 6, 14]. Elimination of plate-shaped and large “Chinese-script”-style intermetallic phases results in an improvement of the mechanical properties of Al-Si castings. Addition of alloying elements such as Mn, Cr, Sr, etc to Al-Si alloys suppresses the formation of the most harmful β plates and causes the fragmentation of β plates, or even changes the types of intermetallics from most harmful β plates to less harmful $\text{Al}_{15}(\text{Fe}, \text{Mn})_3\text{Si}_2$ or $\text{Al}_{13}(\text{Fe}, \text{Cr})_4\text{Si}_4$ phases [68].

A sufficiently high concentration of Sr leads to a breaking of the β needles into smaller and thinner fragments [75, 76]. The mechanism of fragmentation was explained by the diffusion or the rejection of Si from the β plates.

The addition of Sr is also effective in reducing the number, size and volume fraction of the β - Al_5FeSi phase as has been reported in [31, 33].

The distribution of intermetallic phases in unmodified Al-Si alloys is homogeneous. In contrast, the addition of Sr leads to a heterogeneous distribution of secondary intermetallic phases within the eutectic grains of the Al-Si alloys [10, 55]. Recently Timpel et al. [10] reported that the modified eutectic grains can be classified into three parts:

- 1) well-modified central regions with fine fibers, free of intermetallic phases;
- 2) a transition region where the α phase precipitates at the eutectic cell boundaries in the eutectic grain;
- 3) an outer region, where the δ phase forms after a severe segregation of Fe into a Si-rich melt during a second interval of nucleation.

McDonald et al. [53, 55] presented a similar grain cellular structure, in which numerous β phase plates and isolated pores can only be observed in the outer region (region 3).

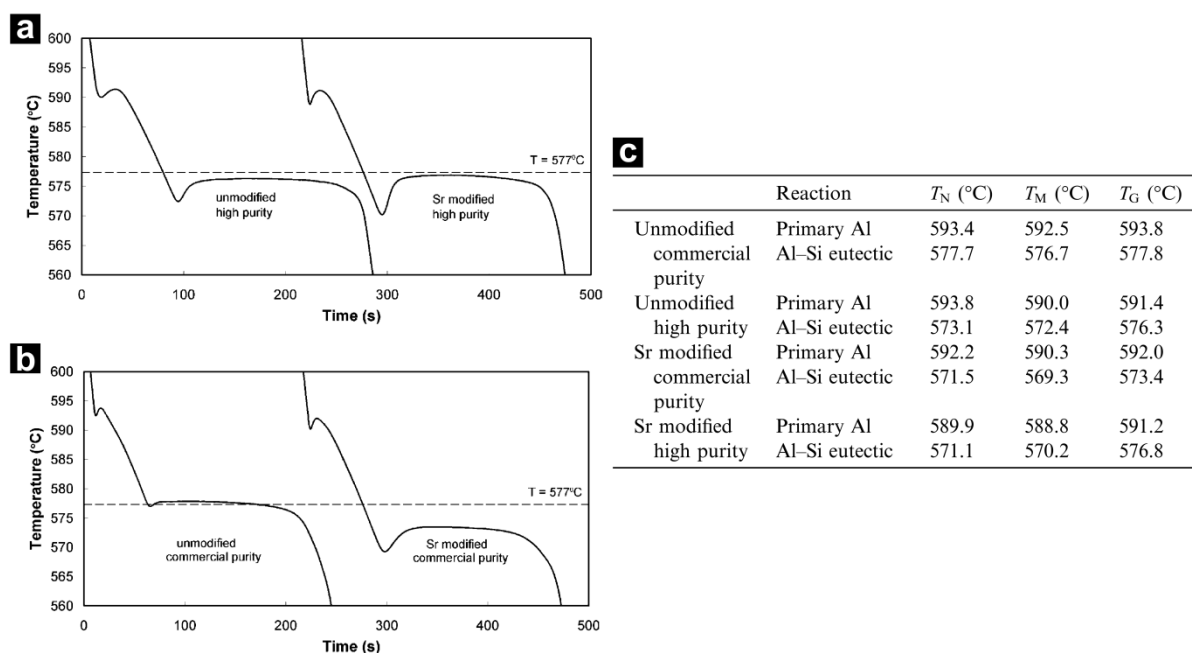


Fig 2.9 Typical cooling curves [71] for: (a) the unmodified and the Sr-modified high-purity Al-10Si alloys; (b) the unmodified and the Sr-modified commercial Al-10Si alloys. The dashed line indicates the equilibrium eutectic temperature of 577°C in binary Al-Si system. The second cooling curve has been displaced along the time axis for the sake of clarity. (c) Reaction temperatures (nucleation, minimum and growth) for the primary and eutectic reactions in each of the four experimental alloys. Nucleation temperature T_N , defined as the first noticeable change on the derivative of the cooling curve, the minimum temperature prior to recalescence T_M , and the growth temperature T_G , defined as the maximum reaction temperature reached after recalescence.

The effect of impurities and Sr modification on the nucleation and growth of eutectic grains in commercial and high purity Al-Si alloys has been investigated in Ref. [71]. The phosphorus content in these alloys was less than 10 ppm. The eutectic in the unmodified high-purity alloy exhibited extremely refined Si flakes, whereas the eutectic microstructure of the unmodified commercial alloy was a typical mixture of coarse silicon flakes. The addition of Sr to both the high-purity alloy and the commercial alloy modified the eutectic Si phase, resulting in a flake-fibrous morphology of the eutectic Si phase. The average cooling rate for both commercial and high-purity alloys prior to solidification was 1.5 K/s. The typical cooling curves obtained during solidification of the above unmodified high-purity alloy and Sr-modified high-purity alloy are shown in Fig. 2.9a. The unmodified commercial alloy and the Sr-modified commercial alloy are shown in Fig. 2.9b. The characteristic

2 Background

temperatures for the primary and eutectic reactions obtained from these curves are shown in Fig. 2.9c.

The comparison of the cooling curves of the commercial alloys (Fig. 2.9b) indicates an increase in recalescence at the eutectic temperature and the repression of the eutectic growth temperature when Sr is added. In contrast to the unmodified commercial alloy, the unmodified high-purity alloy (Fig. 2.9a) shows a significant amount of recalescence and a negligibly decrease of growth temperature. The addition of Sr to the high-purity alloy increases the recalescence but does not reduce the growth temperature.

3. Materials

This chapter describes the preparation of hypoeutectic Al-10Si-0.3Fe – based alloys which were chosen for the investigations. In order to examine the influence of impurities on the formation of Fe-rich intermetallic phases, a high purity alloy and a commercial alloy were used for experiments. Sr was added to the both alloys to study its influence on the evolution of Fe-rich intermetallic phases. In total, four Al-10Si-0.3Fe-based alloys have been produced externally:

- 1" High-purity Al-10Si-0.3Fe alloy named "P"
- 2" High-purity Al-10Si-0.3Fe alloy with Sr addition, named "PS"
- 3" Commercial Al-10Si-0.3Fe alloy, named "C"
- 4" Commercial Al-10Si-0.3Fe alloy with Sr addition, named "CS"

The detailed fabrication is as follows:

Al-10 Si-0.3 Fe (in wt.%) alloys with alloying elements of high purity (> 99.99 purity) and alloying elements of commercial purity (> 99.70 purity) were manufactured separately by Hydro Aluminium, Germany. For the modification of the eutectic Si, an Al-10Sr (wt.%) master alloy was added to the unmodified alloy. The ratio between both the unmodified and the master alloy has been chosen in such a way that at the end the alloy contained only 200 ppm Sr. The unmodified and the Sr-modified melt were cast into a cylindrical permanent mold with a diameter of 30 mm and a height of 200 mm. The total solidification time was approximately ~40 s. The chemical compositions of both the unmodified and the Sr-modified Al-10Si-0.3Fe casting alloys as measured by optical emission spectrometry are listed in Table 3.1.

3 Materials

Table 3.1 Chemical composition of the Al–10Si–0.1Fe alloys with and without Sr additions. The main elements Al, Si and Fe are given in wt. % and impurities in ppm.

Alloy	Al	Si	Fe	Cu	Mn	Mg	Ni	Zn	Ti	Cr	V	Ga	P	Sr
	wt. %			ppm										
P	89.7	10.0	0.3	7	7	4	17	33	11	4	21	80	<4	<1
PS	89.8	9.9	0.3	7	7	4	17	33	11	4	21	81	<4	197
C	89.8	9.9	0.3	16	16	4	49	96	21	9	65	92	7	<1
CS	89.6	10.1	0.3	16	15	4	47	96	20	8	63	90	8	221

4. Experimental methods

Various microscopic methods scaling the size range from mm to nm were used for the investigation of the influence of the modifying element Sr and the impurity elements on the formation of the intermetallic phases in Al-Si alloys. Thus it is possible to characterize the complete intermetallic phases and the distribution of the eutectic phases around the associated intermetallic phases. The activities undertaken in this PhD thesis and the methods used are divided into two areas:

- 1) The investigation of the microstructure, consisting of intermetallics with/without the related eutectic areas, scaling in the range from nm to mm was carried out by optical microscopy and Scanning Electron Microscope to reveal the detailed microstructure. Additional TEM analysis was used to identify the type of the Fe-containing intermetallic phases.
- 2) A three-dimensional visualization of the intermetallic phases with/without the related eutectic areas was implemented to gain insight into the morphology of the precipitates and their spatial arrangement, scaling from submicron to submillimeter using the methods of FIB tomography and synchrotron X-ray tomography. In particular, In-situ synchrotron tomography was performed to image in real time the shape, the location and the interactivity of the intermetallic phases precipitating in the melt during phase separation. Thus it is possible to study these parameters as a function of the solid fraction as the temperature decreases during solidification.

Specimens used in this work are prepared in many different and complex ways, depending on the requirements of the instruments and the facilities that are involved as described below.

4.1 Optical Microscopy

Optical microscopy analysis allows one to get a rough overview of the microstructure and to obtain 2D images of the morphology of phases on different size scales from the investigated

4 Experimental methods

samples. A Zeiss microscope Axiophot 2, equipped with a digital camera AxioCamHRc was used for image acquisition from the microstructure of the samples investigated in this work.

For the investigations by means of optical microscope, the cast rods were sectioned perpendicular to their axes, ground using standard metallographic procedures and finally polished with a colloidal silica suspension with a particle size of 50 nm (OP-U). All specimens investigated in this work were extracted from the centers of the castings, 15 mm from the bottom of the initial cast ingot.

The optical microscopic examination of the samples was performed in differential interference contrast mode (Differential Interference Contrast, DIC). Basically near-surface regions of the sample could be mapped very well using the DIC contrast without etching.

4.2 Scanning Electron Microscopy

A Zeiss 1540EsB CrossBeam® workstation combined with an ultra-high-resolution GEMINI® field emission column was used to characterize the microstructure of the Al-Si alloys.

In a scanning electron microscope, depending on the material and the selected acceleration voltage, the primary electron beam scans the sample surface in a raster pattern while secondary electron products are created in a so-called interaction volume (excitation bulb), as illustrated in Fig 4.1, which can be used for imaging and analysis.

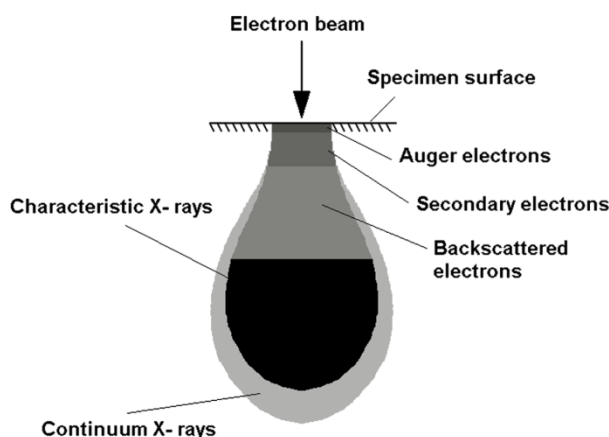


Fig. 4.1 Excitation bulb of an electron beam impinging on a solid surface [77]

The electron beam is created by applying an electric field of about 0.2 – 40 keV to a thin needle of different types. The beam is then focused by lenses and arrives at the sample surface with a diameter of 0.4 to 5 nm. In the interaction volume with the material it creates Auger electrons, secondary electrons (SE) and backscattered electrons (BSE), the two latter are being the most used for investigations. Different detectors are necessary for different types of electrons, as shown in Fig. 4.2.

In this work we use secondary electrons, which, in the Zeiss Gemini, are collected in two ways: either at the SE detector grid situated at the side of the sample chamber, or in the so-called InLens detector, which is situated inside the column.

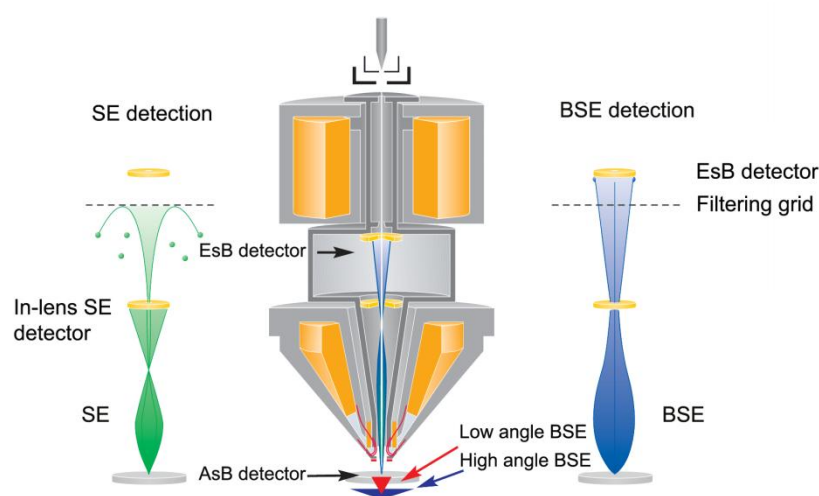


Fig. 4.2 Trajectories of the electron in every detector ([78] modified)

BSE electrons can be collected either at low backscattering angles, close to the sample surface (Angular selective Backscatter (AsB) detector) or inside the column at high backscattering angles (EsB detector).

Sample preparation for SEM is the same as for OM.

4.3 Transmission Electron Microscopy

In order to identify the intermetallic phases present in the investigated alloys unambiguously, the crystal structures of the intermetallics were determined by selected-area electron diffraction (SAED). Every interplanar spacing d was calibrated using SAED patterns of eutectic Al or Si crystallites surrounding the corresponding phase. The chemical composition

4 Experimental methods

of the constituent phases was analyzed by TEM–EDX using a minimum of five measurements for every intermetallic phase.

4.3.1 TEM system

As shown in Fig 4.3, a transmission electron microscope usually contains four parts: electron source, electromagnetic lens system, specimen stage, and imaging system. The electron beam in the TEM is produced in a similar way as in the SEM. The applied electric field is much higher, in our case 300 kV, and the electron source is an LaB₆ cathode. After passing through the anode the electron beam is focused by a combination of lenses and apertures.

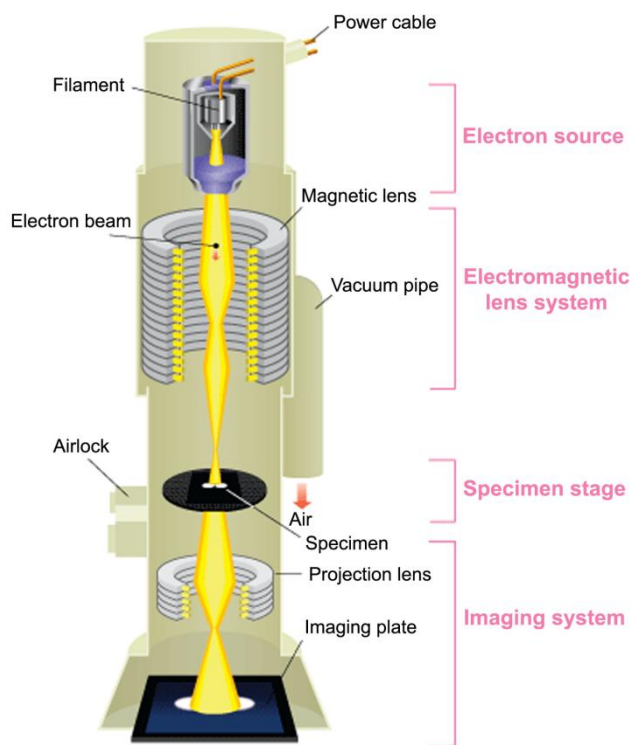


Fig. 4.3 Schematic outline of a TEM. A TEM contains four parts: electron source, electromagnetic lens system, specimen stage, and imaging system [79].

Samples are usually placed in a double-tilt sample holder which allows for tilting of the crystallographically interesting regions towards the electron beam. After the beam has hit the sample the image or the diffraction pattern can be recorded by either the Gatan Retractable Slow-Scan CCD camera (Model 694) or the Fuji imaging plates. Additionally it is possible to record the elements' specific x-ray lines to perform local chemical analysis by using the

EDAX energy dispersive x-ray spectroscopy (EDX) detector, which is placed to the side and above the specimen level.

In this work, a Philips CM30 TEM microscope operating at 300 kV and equipped with an EDAX Genesis EDX system was used.

4.3.2 Sample preparation

A TEM specimen must be thin enough to let a sufficient number of electrons pass through to form an image with minimum energy loss. Therefore specimen preparation is an important aspect of TEM analysis. Samples for TEM investigation were prepared in two steps. In the first step, they were cut into pieces of $1 \times 1 \text{ mm}^2$ area and mechanically ground to $30 \mu\text{m}$ thickness using the T-tool technique [80]. In the second step, they were thinned to electron transparency with a voltage of 5 kV by using Ar-ions at a current of 2.5 mA and an angle of incidence of $\pm 6^\circ$. Ion milling was carried out in a Bal-Tec Res101 machine.

4.4 Focused Ion Beam

To obtain the morphology of intermetallic phases in three dimensions a serial sectioning technique developed quite recently by means of FIB tomography has been used [19, 35-36]. Sample preparation is the same as in the SEM part.

4.4.1 FIB system

The system of focused ion beam, as illustrated in Fig. 4.4, is analogous to the scanning electron microscope, but instead of an electron beam, the FIB uses a focused beam of Ga^+ ions to scan the surface of a specimen. The Ga^+ ion source is a liquid-metal ion source and the ions are retracted by an high electric field. The Ga^+ ions are then accelerated to 30 keV and focused onto the sample via electrostatic lenses. The whole system operates in vacuum to prevent the ions from any interactions with other ions or molecules.

Unlike an electron microscope, the FIB is inherently destructive to the specimen. When the high-energy Ga^+ ions strike the sample, surface collision with energetic ions leads to the sputtering away of atoms from the sample surface. For this reason a high primary ion beam

4 Experimental methods

enables a precise material milling and cutting of slices from the sample surface in a controlled way.

For the current FIB tomography experiment, a Zeiss 1540EsB CrossBeam® workstation was used. This workstation combines a FIB column and an additional SEM column. This combination allows one to simultaneously use the FIB for milling and the SEM for high-resolution imaging. As illustrated in Fig 4.5, the FIB, which is positioned perpendicular to the milling direction of sample, is set at 54° with the SEM. As a result, the serial cross-

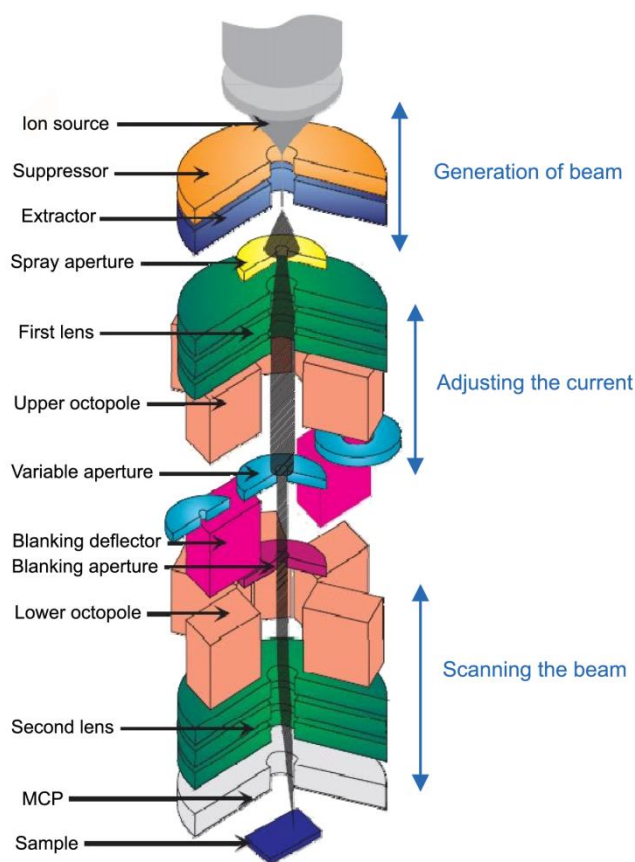


Fig 4.4 Schematic diagram of a FIB system [81]

section plane of the sample prepared by FIB serial milling and serial sectioning normal to the sample surface can be characterized by the SEM to obtain serial two-dimensional information. Slices of about 20 nm thickness were cut with a 30 keV Ga^+ ion beam and an ion current of 500 pA. The SEM used in the FIB-SEM system is the same as the one that we mentioned in chapter 4.2, the detectors used for SEM in the FIB tomography system are the Inlens and the EsB detectors mentioned before. Inlens and EsB electron detectors were used

at an accelerating voltage of 2 kV and a grid voltage of ~1.5 kV in the scanning electron microscope.

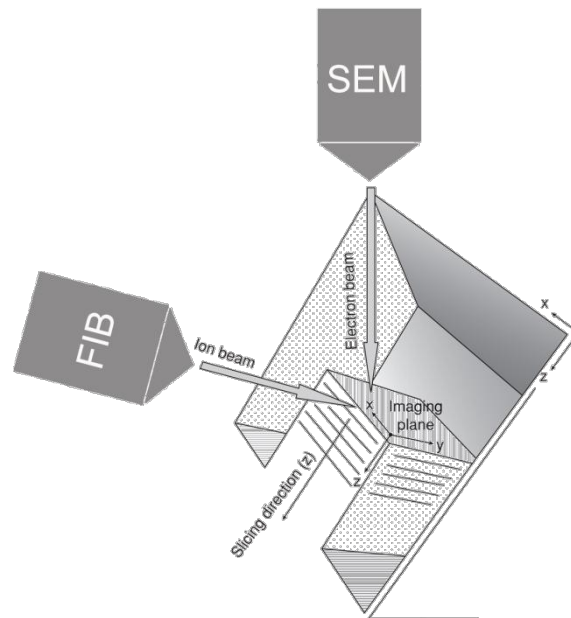


Fig. 4.5 Illustration of FIB serial sectioning with a dual beam FIB-SEM system ([82] modified).

4.4.2 Data processing

FIB-SEM imaging, yielding 3D data stacks from measured electron signals, captured by InLens and EsB detectors, provides the possibility for three-dimensional visualization. By alternating imaging and milling the FIB-SEM system can be used to reconstruct a 3D image of the removed material. In order to get a three-dimensional image, some necessary work has to be done.

- 1) Alignment of individual images by ImageJ
- 2) Correction of image defects (noise reduction with Gauss-filter)
- 3) Three-dimensional reconstruction and analysis by VGStudio 2.1

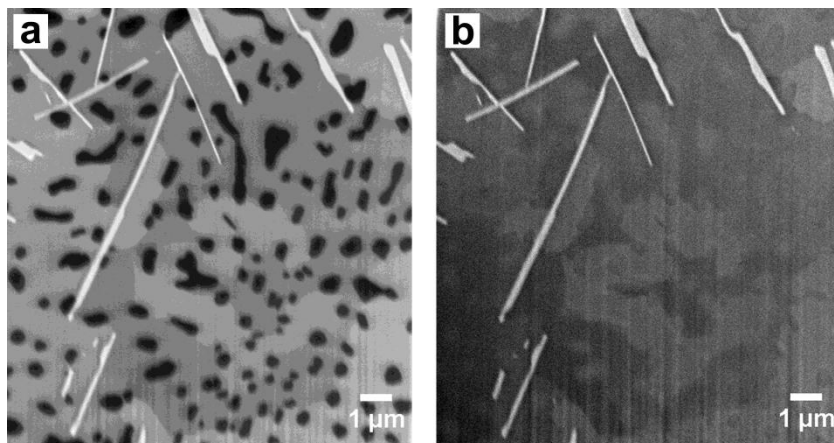


Fig. 4.6 image based on the same view using the (a) InLens detector or (b) EsB detector

After recording the FIB serial sections acquired by the InLens and EsB detectors, grayscale image stacks are obtained. In this work, the InLens images have a better contrast for eutectic Si while EsB images are better for exhibiting the Fe-containing intermetallic phases. These 2D images were first calibrated using the software "ImageJ" to eliminate the drift of a time-lapse image stacks caused during recording. The ImageJ plugin called "Template matching" [83], which can utilize the matching function to do slice registration (alignment) is based on a selected landmark and was used to fix the drift of the sample during recording. The landmark pattern will thus be the same position throughout the whole stack since this function finds the landmark or the most similar image pattern in every slice and translate every slice that is badly positioned accordingly.

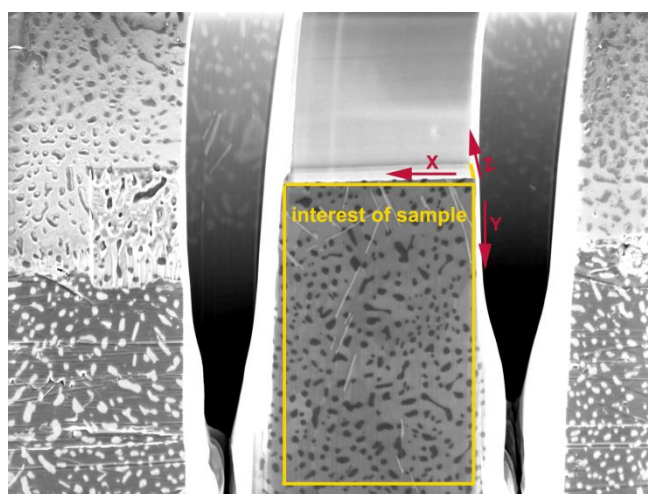


Fig. 4.7 Sectioning of SEM imaging plane X-Y for 2-D-FIB tomography

After the alignment of the image stack is done, the polished edge of the samples has to be removed by ImageJ, only leaving the interesting part of the sample (see Fig. 4.7). To reduce the noise, filters with 3D Gaussian blur selected as 15x15x15 for all image stacks are carried out using ImageJ.

After data processing, the 3D reconstruction of the investigated volume was performed using the software "VGStudio MAX 2.1". 3D reconstruction is based on the linear interpolation of the light intensity of every pixel [84]. The serial sectioned volumes in this work are basically smaller than around $10 \times 10 \times 10 \mu\text{m}^3$, 1 voxel (volumetric pixels) being about $25 \times 25 \times 25 \text{ nm}^3$ in size. The X-Y pixel sizes of the 3-D voxels are determined from the SEM images, as seen in Fig 4.6. The voxel size in the Z-direction is defined by the distance between the FIB serial sections. The intermetallic phases used for segmentation in VGStudio Max 2.1 pass through a suitable selection of a global threshold in the grayscale histogram of the tomogram determined by ImageJ. The 3D median filter given by VGStudio Max 2.1 at $3 \times 3 \times 3$ for the reduction of noise was the last step of data processing.

4.5 Synchrotron X-ray Tomography

The size range of the intermetallic phases in the investigated materials ranges from about 0.3 μm to 30 μm , which is partly beyond the observation limits of FIB tomography (in our case: less than 10 μm). Another powerful tool enabling the use of tomography was considered: X-ray tomography. Since conventional laboratory X-ray sources are not comparable with synchrotron radiation sources concerning highly collimated X-rays and high X-ray brightness/flux, the visualization of a big volume, far beyond the FIB tomography limits, was performed by synchrotron X-ray tomography. The comparison of the visualized volumes by FIB-tomography and by synchrotron X-ray tomography is given in Fig 4.8.

Synchrotron tomography was carried out at beamline ID 19 of the European Synchrotron Radiation Facility (ESRF), France, and all facilities and mechanisms introduced below are from ESRF. The main advantage of this facility is the possibility of imaging the microstructural evolution during solidification by in-situ measurement.

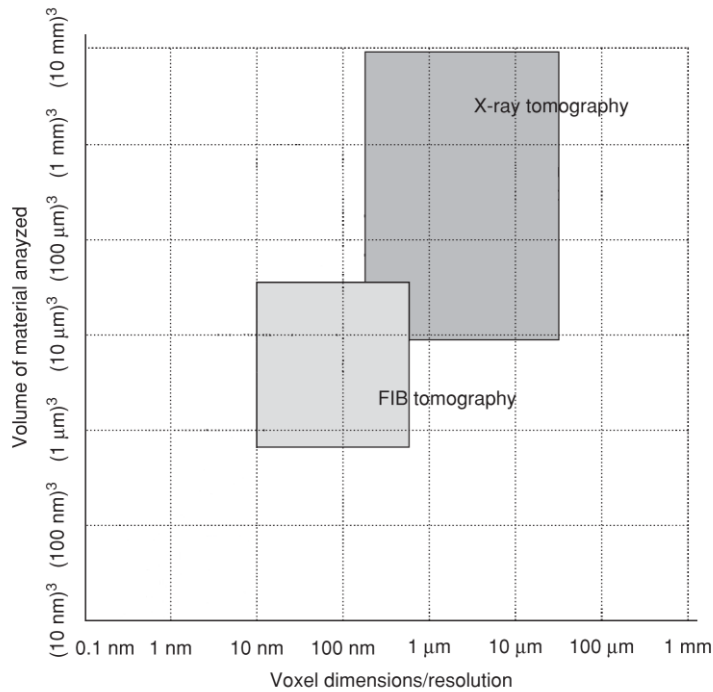


Fig 4.8 Comparison of FIB-tomography and synchrotron x-ray tomography. ([82] modified).

4.5.1 Synchrotron system

The shape of synchrotrons is like a large torus [85]. Synchrotrons accelerate a beam of electrons in order to let them pass through straight vacuum tubes and insertion devices such as bending magnets [86]. The synchrotron ring thus has the shape of a large polygon that approximately looks like a torus. Modern third generation synchrotrons have four major parts:

1. Linear Accelerator
2. Booster Ring
3. Storage Ring
4. Beamline workstation

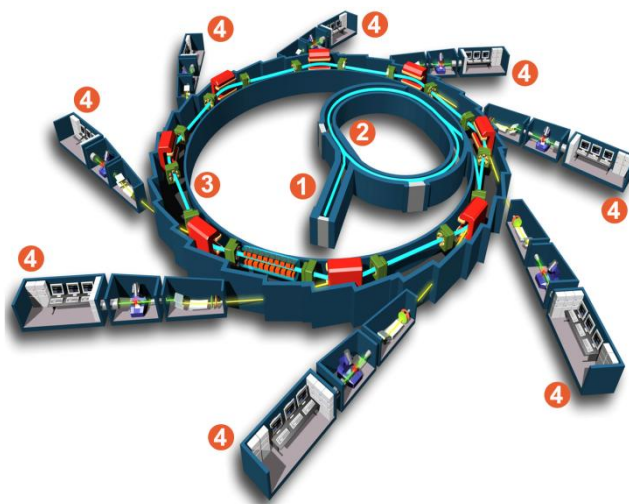


Fig 4.9 A general representation of a typical synchrotron. (1) Linear accelerator; (2) Booster ring; (3) Storage ring and insertion devices; (4) Beamline workstations [87]

1. Linear Accelerator

In this part the electron beam is produced. The acceleration voltage is about 100 keV and the frequency is either 1 or 10 Hz at ESRF. After the beam has passed two accelerating sections they transfer into the booster ring. The injection system for the ESRF storage ring comprises a 200 MeV linear accelerator [88].

2. Booster Ring

The main feature of the ESRF booster has a 10 Hz cycling frequency and a low natural beam emittance. The booster provides the incoming electrons with the necessary energy. Once they have the same energy as the electrons inside the storage ring, they can be injected. This method of having a separate booster ring allows the "top-up" mode, which means that it is not necessary to shut the ring down for injections [85].

3. Storage Ring

The electrons travel through the storage ring and change their direction when they pass through the bending magnets [85]. In order to allow for the production of different types of x-rays for different purposes, insertion devices are placed in the electron beam. There are two main types of insertion devices, i.e. undulators and wigglers. Both are made of

4 Experimental methods

permanent magnets, like a series of alternating bending magnets, and they incite a sinusoidal oscillation of the electrons. This allows for the creation of x-rays in every part of the trajectory where the electron changes its direction [89]. The difference between the two lies in the force of the magnets and thus in the type of the created x-ray spectra: wigglers use strong magnets, which induce a high deviation from the initial trajectory of the electrons. The created x-rays form a high angle with the axis of the wiggler and thus cannot interfere with each other. This implies a broad x-ray spectrum. The aim of the undulator, however, is to provoke interference of the x-rays, which is made possible by smaller deviation angles. This implies a smaller photon energy, but a higher brilliance and a sharp spectrum. In this work we have used a beamline that can use up to four undulators and one wiggler.

The storage ring at the ESRF has a circumference of 844.4 m and an electron energy of 6 GeV [88].

4. Beamline workstation

This is the final part of the synchrotron, the one which is used for research. This end station can be close to the ring, or, in case of ID19 that we used in our work, several meters away. The long distance allows for a good focusing of the beam. Monochromators can be used to choose the wavelength of the beam that is used for experiments. In this work, the beamline workstation of ID 19 was used for microtomography imaging.

4.5.2 Synchrotron X-ray tomography beamline

Synchrotron X-ray tomography is a non-destructive imaging technique that enables three-dimensional analysis of the microstructural interior of materials with a high spatial resolution. The basis of X-ray tomography is X-ray radiography, which has the same principle as the medical scanner, but with a higher resolution. For tomography, a series of radiographs are collected during sample rotating through 180°. This produces a set of projections that can be reconstructed to reveal the 3D structure of the sample [90].

The set-up for our synchrotron tomography at ID19 is illustrated in Fig 4.10. The X-ray beam, coming from the synchrotron ring and improved by a series of up to four undulators and one wiggler (as discussed in last section) is used to illuminate the sample. The transmitted beam, after having been attenuated by the sample, is recorded with a CCD

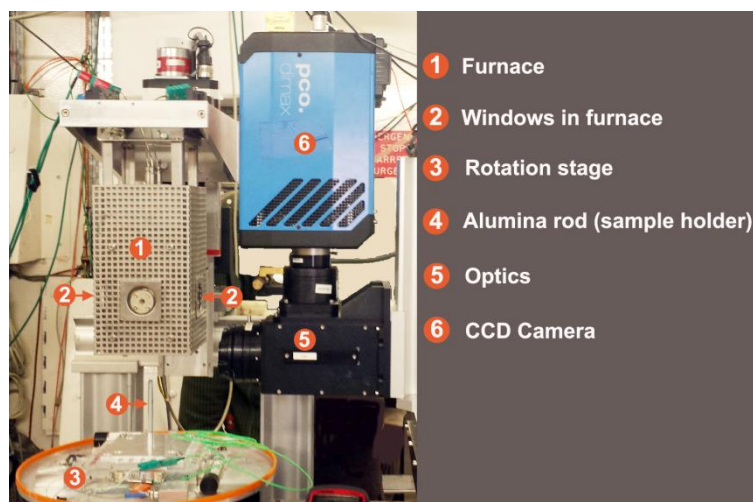


Fig 4.10 Set up for synchrotron tomography

camera. A most important device in the setup is the high-resolution detector that consists of a luminescent screen coupled to a cooled CCD by magnifying optics. The camera at ID 19 (FreLoN: fast readout low noise [91]) has 2048 x 2048 pixels with a fast readout (0.22 frame/s), low dark current (3 electrons/s) and low readout noise (22 electrons). The optimum resolution is of the order of $\sim 1 \mu\text{m}$. The applied beam energy at the measurement was 20.5 keV and the distance between sample and detector was 90 mm.

4.5.3 Sample measurement

A small cylindrical pin sample (3.2 mm long, 1.5 mm in diameter) was machined from the casting and used in the synchrotron tomography solidification experiment. For the experiment, the sample was glued with zirconia paste to the top of an alumina rod placed on the rotating stage. During melting and solidification, the sample was supported by its own oxide skin, i.e. no container was used.

Three-dimensional visualization was carried out by ex-situ and especially in-situ synchrotron tomography experiments to image the density, the shape, the location and the interconnection of the intermetallic phases. This is a strong tool for gaining insight into the morphology of the precipitates and their spatial arrangement. Samples were heated up and in-situ measurements were performed on the cooling samples. The experiments can be classified into two groups: 1) slowing cooling rate; 2) fast cooling rate.

1) Slow cooling rate:

4 Experimental methods

In this part, samples were first gradually heated (at 20 K/min) to 666 °C and then held for 5 minutes at this temperature to ensure complete melting and homogenization. Then the samples were cooled separately at a rate of 1 K/min, 9 K/min and 30 K/min down to 450 °C while microtomography image data was gathered throughout the complete cooling process. The low cooling rate is necessary to ensure that the microstructure does not evolve too much during image acquisition. The entire cooling process took 221 minutes, 24 minutes and 7.2 minutes separately corresponding to above each cooling rates, leaving enough time for a sufficient number of high-resolution tomographs. The parameters used are listed below in detail:

Table 4.1 Parameters of the in-situ synchrotron tomography measurements with a slow cooling rate.

Scan	Parameter
Numbers of projections per scan	1000
Duration of one scan	60s
Scan angle range	180°
Number of scans	216
Number of turns between scans	1
Download data between scans	1
(region of interest): X-axis	1632 pixels
(region of interest): Y-axis	1632 pixels
Numbers of dark images (no beam)	20
Numbers of flat images (without sample)	21
Numbers of dark images before scan	1
Numbers of flat images before scan	1

2) Fast cooling rate:

The fast cooling rate measurements differ from the slow cooling rate experiments by the cooling rate for solidification and the associated scanning parameters. Samples were first gradually heated (at 20 K/min) to 700 °C to ensure complete melting and homogenization (sample temperature measured by a type K thermocouple located close to the sample). Then the samples were cooled at a rate of 400 K/min down to 450 °C (solidus temperature) while microtomography image data was gathered throughout the complete cooling process. This fast cooling rate is close to commercial casting condition. The entire cooling process, down to room temperature takes about 10 minutes.

The parameters that we used are listed below in detail:

Table 4.2 parameters of fast cooling rate for in-situ synchrotron tomography measurements

Scan	Parameter
Numbers of projections per scan	1000
Duration of one scan	28s
Scan angle range	180
Number of consecutive scans	37
Number of turns between scans	1
Download data between scans	0
(region of interest): X-axis	1152 pixels
(region of interest): Y-axis	800 pixels
Numbers of dark(no beams)	20
Numbers of flats(without sample)	21
Numbers of dark images before scan	1
Numbers of flat images before	1
Exposure time of each projection	0.001s
Number of flat (no beam)	101
Number of dark (without sample)	50

4.5.4 Data processing

The raw data was reconstructed by the standard ESRF tomography reconstruction software pyHST (High Speed Tomography in python version) [92].

After reconstruction of the raw data, all image stacks were first treated to reduce the noise. This was performed with a 15 x 15 x 15 3-D Gaussian blur filter for all image stacks using ImageJ. Then every image stack was introduced into VGStudio MAX 2.1 for 3D visualization. The intermetallic phases used for segmentation in VGStudio Max 2.1 pass through a suitable selection of a global threshold in the grayscale histogram of the tomogram determined by ImageJ. For the current tomography, 1 voxel is $0.55 \times 0.55 \times 0.55 \mu\text{m}^3$. Some of the initial room temperature state measurements have the following voxel size: 1 voxel = $1.1 \times 1.1 \times 1.1 \mu\text{m}^3$. Different phases were rendered by different colors as will be seen in the following section.

5. Results

5.1 Microstructure characterization

In this part, the microstructure of four alloys is characterized separately by OM, SEM and TEM. The microstructure features among unmodified alloys and Sr-modified alloys, pure alloys and commercial alloys are compared.

5.1.1 Optical microscopy

The microstructures of all four investigated alloys obtained by OM at low and high magnification are shown in Fig. 5.1 and Fig. 5.2 and classified into four images as unmodified pure and Sr-modified pure alloy, unmodified commercial and Sr-modified commercial alloy. The images illustrate the typical eutectic microstructure of all Al-10Si-0.3Fe alloys.

The difference between pure alloys and commercial alloys is that the pure alloys in this study are nearly without any impurities. However, the microstructure of the eutectic Si phase is very similar to that exhibited in the literature [10, 71]. In the unmodified pure alloy, eutectic Si appears as needles in two dimensions in Fig. 5.1a and 5.2a, whereas in the unmodified commercial alloy (Fig. 5.1c and 5.2c) eutectic Si exhibits huge coarse platelets with bigger spacing, embedded in the Al matrix. The addition of strontium to both the pure alloy and the commercial alloy leads to the transition from needles (Fig. 5.1a and 5.2a) and huge coarse platelets (Fig. 5.1c and 5.2c) to a fine microstructure of eutectic Si (Fig. 5.1b and 5.2b, Fig. 5.1d and 2d). The microstructure in Sr-modified pure alloy and in Sr-modified commercial alloy is quite similar, only the eutectic in the unmodified pure alloy is slightly finer than that in the Sr-modified commercial alloy, as seen in Fig. 5.2b and 5.2d.

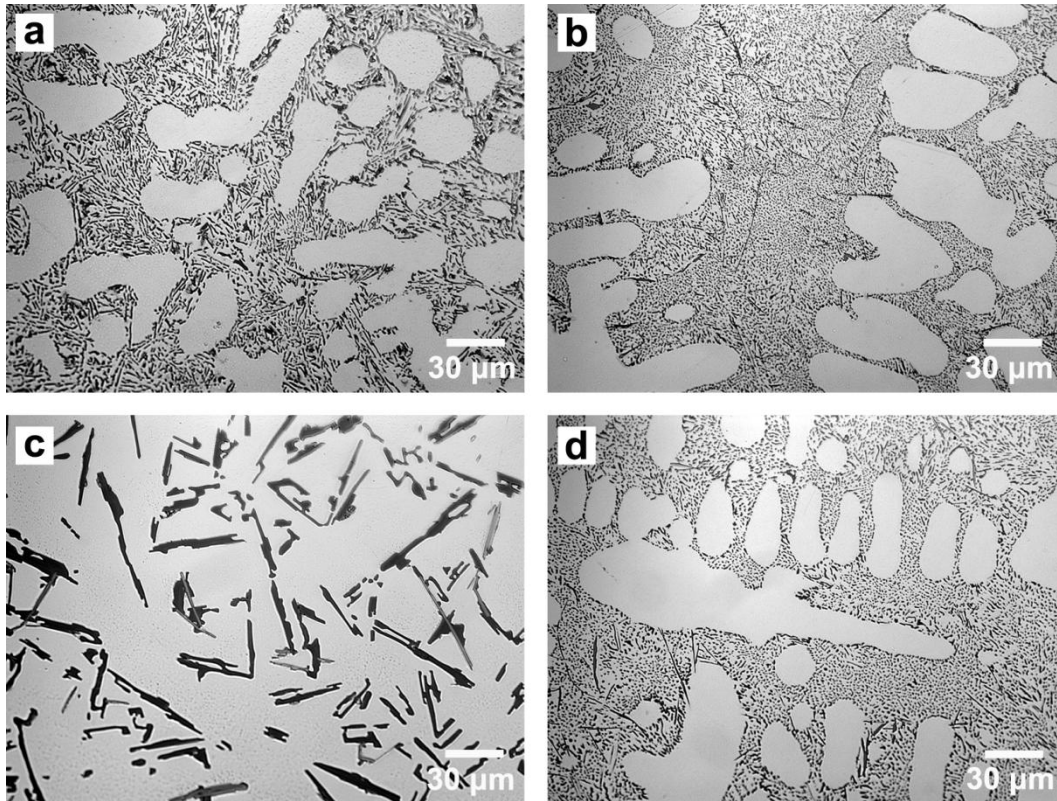


Fig. 5.1. Optical micrographs of the microstructure of (a) unmodified pure and (b) Sr-modified pure, (c) unmodified commercial and (d) Sr-modified commercial Al-10Si-0.3Fe alloys. (Al matrix in bright gray; eutectic Si in black; intermetallics in dark gray)

While the OM images of all alloys in Fig. 5.1 and Fig. 5.2 clearly show primary Al dendrites as bright regions, the intermetallic phases are difficult to distinguish because of the low contrast difference to eutectic Si (both dark in contrast). In order to observe intermetallic phases more clearly, SEM has been used.

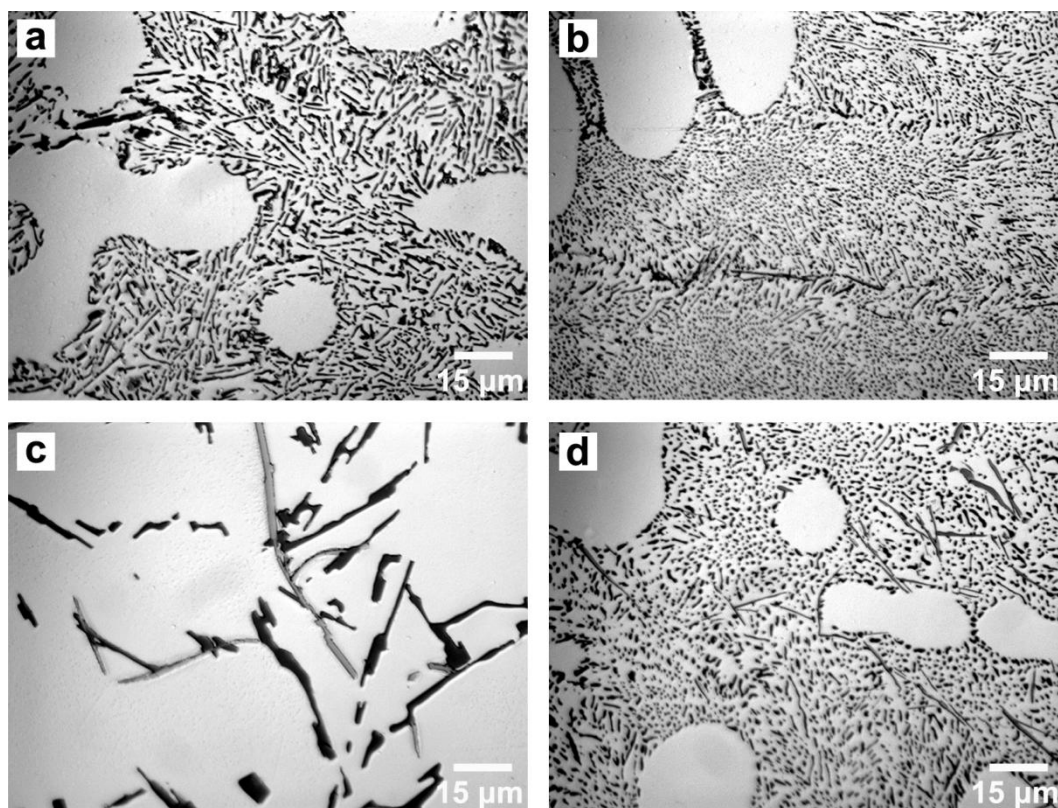


Fig. 5.2 Optical micrographs of the microstructure of (a) unmodified pure and (b) Sr-modified pure, (c) unmodified commercial and (d) Sr-modified commercial Al-10Si-0.3Fe alloys. (Al matrix in bright gray; eutectic Si in black; intermetallics in dark gray)

5.1.2 Scanning Electron Microscopy

Figure 5.3 illustrates the microstructures of unmodified (Fig. 5.3a) and Sr-modified (Fig. 5.3b) Al-10Si-0.3Fe alloys as imaged using the InLens detector of the SEM. The microstructure consists of eutectic Si, eutectic Al as well as Fe-rich intermetallic phases that can be distinguished by different contrast and morphology. The intermetallic Fe-rich phases appear brightest. While the α phase in Fig. 5.3a has a “Chinese script” morphology in 2D, the δ phase in Fig. 5.3b is needle-like, which are described in Fig. 5.3c and Fig. 5.3d too. The eutectic Si phase is uniformly dark in contrast. The morphology of the eutectic Si phase changes from plates in the unmodified alloy (Fig. 5.3a) to fibres in the Sr-modified alloy (Fig. 5.3b). The eutectic Al phase appears light grey and varies slightly in contrast from one grain to the other because of the different crystallographic orientations of the individual grains.

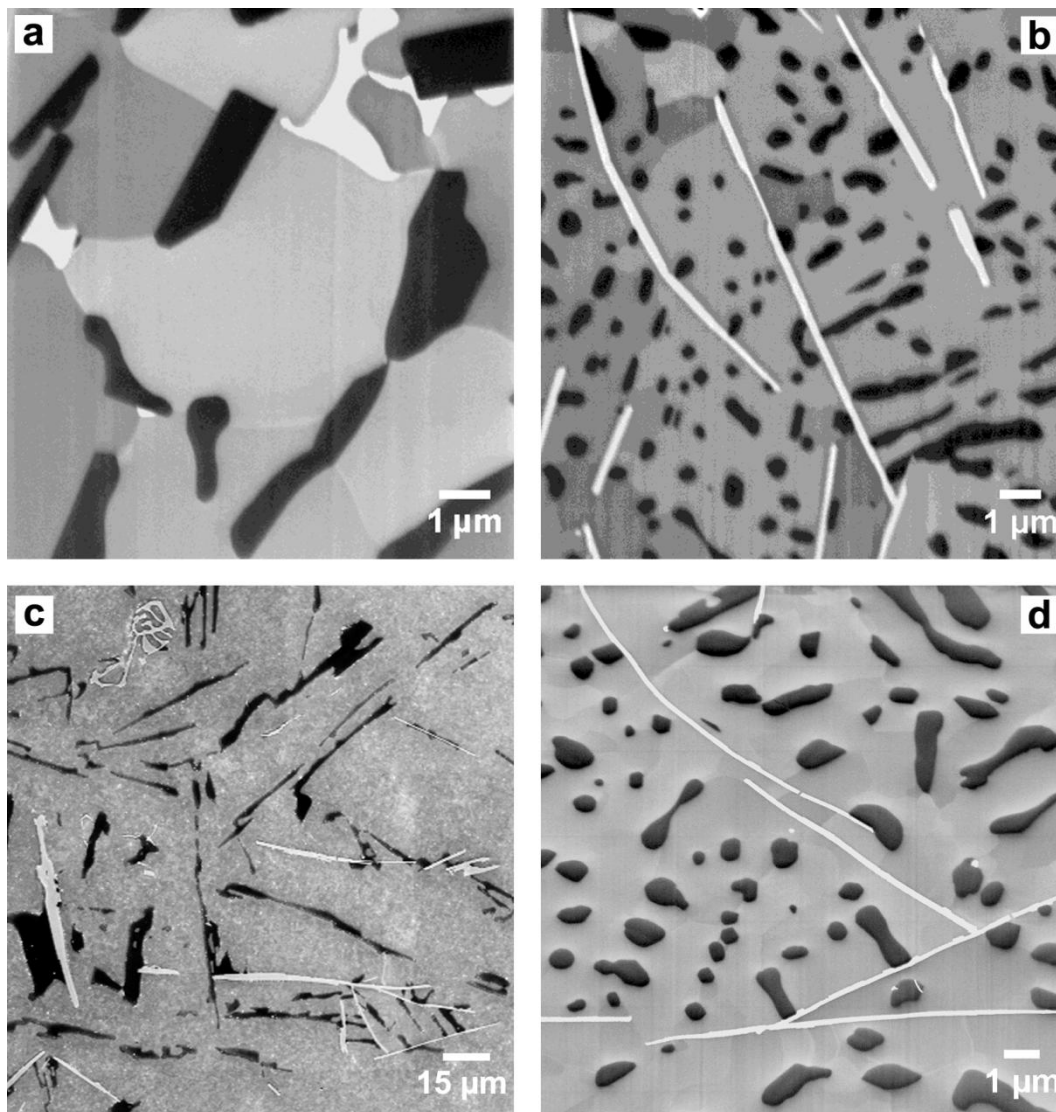


Fig. 5.3. Microstructure of intermetallics (in white), eutectic Si (in black) and Al matrix (in various gray) in Al-10Si-0.3Fe alloys acquired by SEM with the InLens detector: (a) unmodified pure and (b) Sr-modified pure alloy; (c) unmodified commercial and (d) Sr-modified commercial alloy.

The intermetallic phases in Fig. 5.3 are displayed in bright contrast using the InLens detector of the SEM. As can be seen in Fig. 5.3 the intermetallic phases differ in morphology amongst the four alloys. A “Chinese Script” morphology is exclusively present in the unmodified pure alloy (Fig. 5.3a), whereas a needle-like morphology (in 2D) is dominant in the Sr-modified alloy and commercial alloy (Fig. 5.1(b-d)), especially in volume. Instead of intermetallics exhibiting “Chinese Script” morphology in unmodified alloy (Fig 5.3a and Fig 5.3c), intermetallics exhibiting small rounded morphology is observed in Sr-modified alloy (Fig 5.3b and Fig 5.3d). The size of the “Chinese Script” phases in the Sr-modified pure

alloy and the Sr-modified commercial alloy is about 18 times less than in the unmodified pure alloy. The sizes of eutectic Si and the intermetallics are listed in Table 5.1.

Table 5.1 Maximum measured lengths (in 2D) of eutectic Si and intermetallics in Al-10Si-0.3Fe alloys (in μm)

alloys	eutectic Si	"Chinese Script" phases	needle-like intermetallics
unmodified pure alloy	4.6	3.6	-
Sr-modified pure alloy	2.1	0.17	10.7
unmodified commercial alloy	64.5	34.6	84.1
Sr-modified commercial alloy	2.3	0.19	11.7

Note: “-” means no such phase found in alloy.

Intermetallic phases with “Chinese Script” morphology are homogeneously distributed within the grains, which corresponds to observations reported for unmodified commercial alloys [71]. In both Sr-modified alloys the needle-like intermetallic phases are located at the

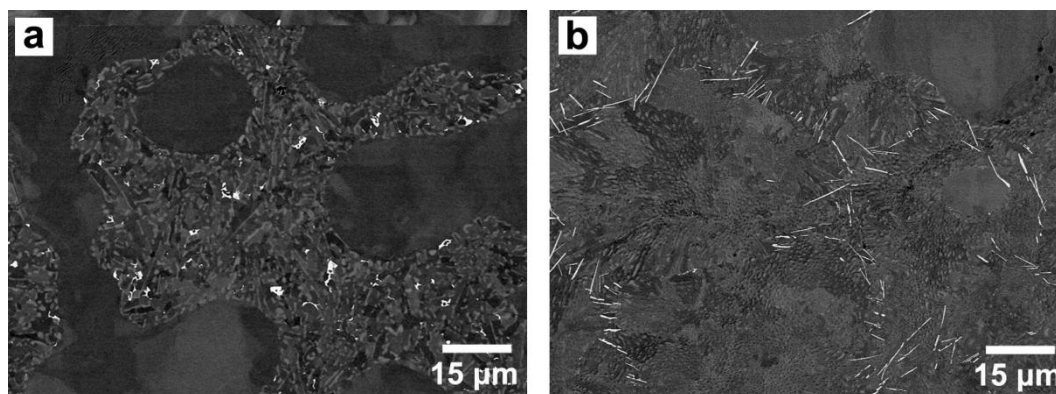


Fig. 5.4. Distribution of intermetallic phases (in white) among Al dendrites (in black) and eutectic Si (in gray) in Al-10Si-0.3Fe alloys obtained by SEM with the AsB detector: (a) unmodified pure and (b) Sr-modified pure alloy.

boundaries of the eutectic cells and the eutectic grains. While in the commercial alloys both the needles and the "Chinese Script" phases were observed in about equal proportion [55, 71], in the pure alloy of the present study the needles are dominant.

5.1.3 Transmission Electron Microscopy

Detailed investigations of the structure and the composition of the intermetallic phases were carried out using TEM. The typical microstructures of intermetallic phases embedded in the eutectic Al and Si of the various Al-10Si-0.3Fe alloys are illustrated in Fig. 5.5-5.9 by bright-field TEM images.

5.1.3.1 Unmodified high-purity alloy

Intermetallic phases containing Fe are darker than the surrounding eutectic matrix due to the atomic number contrast, which makes it easy to locate them. Figure 5.5a shows an intermetallic phase in the center of the image. The corresponding SAED pattern indicates a body-centered cubic structure with space group $Im\bar{3}$ and lattice parameter $a = 1.2531$ nm. The chemical composition of this phase has been determined to be $Al_{14}Fe_{2.8}Si_2$ by TEM/EDX. Although the stoichiometry of this phase is slightly different from that reported in the literature [10, 15, 16, 18, 19, 58], the measured lattice parameter $a = 1.2531$ nm is within the specified range for the α -intermetallics $Al_{15}(Fe, Mn)_3Si_2$, where $a = 1.2500 - 1.2800$ nm [93]. The morphology of this phase in 2D is that of “Chinese Script”. The formation of the τ_5 phase (α phase) has recently also been reported in high purity Al-ySi ($y = 5 \div 12.5$ wt.%) alloys for a cooling rate above 5 Ks^{-1} [29]. However, the structure of the τ_5 phase with the chemical composition $Al_{12.2}Fe_{3.6}Si_2$ has been found to be hexagonal, unlike

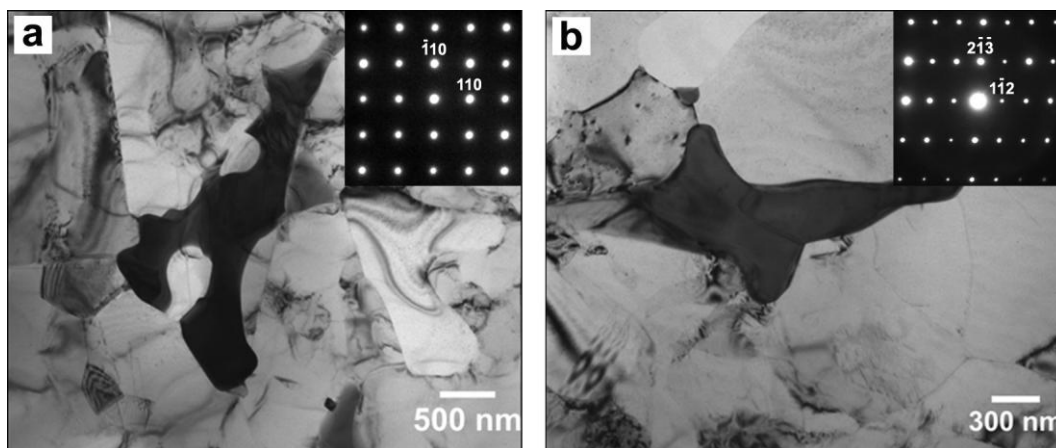


Fig. 5.5. Bright-field TEM images of the intermetallic phases (dark in contrast) embedded in the eutectic Al and Si of unmodified pure Al-10Si-0.3Fe alloy: (a) α -intermetallic and the corresponding diffraction pattern along [001] of the bcc structure in the inset; (b) γ -intermetallic and the SAED pattern along [571] of the trigonal R-centered structure.

the bcc α phase with $\text{Al}_{14}\text{Fe}_{2.8}\text{Si}_2$ composition found in the present study. Small differences in the Al and Fe content in this phase possibly cause the formation of different structures.

5.1.3.1.1 γ -AlFeSi (τ_2 intermetallics)

Another intermetallic phase shown in Fig. 5.5b was found in the present work and given the preliminary designation γ -AlFeSi. The chemical composition of this phase, as measured by TEM/EDX, corresponds to $\text{Al}_{4.35}\text{FeSi}$. This is close to the composition of the β - $\text{Al}_{4.5}\text{FeSi}$ phase. However, SAED patterns showed that the crystal cell is different. Furthermore the morphology of the phase (Fig. 5.5b) differs from that of the β phase, because the β phase appears needle-like in 2D, with lengths of a few hundred μm , and plate-like in 3D. The morphology and the size of the observed phase γ -AlFeSi in 2D (only a few micrometers) is thus rather comparable to that of the α phase, but the composition is different. The determination of the cell parameters from a set of SAED patterns resulted in a trigonal cell. The hexagonal R-centered setting of this cell is:

$$a = 1.034(5) \text{ nm}, c = 1.983(8) \text{ nm}, V = 1.836(25) \text{ nm}^3, c/a=1.918(17)$$

The primitive rhombohedral setting is

$$a = 0.891(6) \text{ nm}, \alpha = 71.0(5)^\circ, V = 0.615(8) \text{ nm}^3$$

Since $60^\circ < \alpha < 109.47^\circ (= \arccos(-1/3))$ this is simultaneously the unique reduced cell which does not depend on the setting of the initial cell. Unless stated otherwise all notes concerning this cell in the following refer to the hexagonal R-centered setting. At first sight the cell parameters did not match the values for any phase in the system Al-Fe-Si, as compiled in 2007 by Krendelsberger et al. [46]. When checking the reduced cells of all Al-Fe-Si phases listed in [46] we realized that the “new” phase is identical with the phase τ_2 , also called γ -AlFeSi - by chance our preliminary name. The space group of this phase is not known, only the Pearson lattice designation mC (monoclinic C-centered) is given. The average cell parameters for the C-centered setting are:

$$a = 1.78(1) \text{ nm}, b = 1.025(5) \text{ nm}, c = 0.890(5) \text{ nm}, \beta = 132^\circ (\sigma \text{ not given}).$$

The six references cited in [94] use the A-centred setting (a and c interchanged).

The range of composition is given as $\text{Al}_{53.9-65.3} \text{Fe}_{19.5-20.5} \text{Si}_{15.2-22.5}$.

The matrix $\begin{pmatrix} 1/2 & -1/2 & 1 \\ 1/2 & 1/2 & 1 \\ 0 & 0 & 1 \end{pmatrix}$ transforms the C-centered cell into the reduced cell.

5 Results

$$a = 0.887 \text{ nm}, b = 0.887 \text{ nm}, c = 0.890 \text{ nm}, \alpha = 70.61^\circ, \beta = 70.61^\circ, \gamma = 70.59^\circ$$

which is nearly identical with the rhombohedral cell we obtained from the evaluation of SAED patterns. The special value $\alpha \approx \beta \approx \gamma \approx 70.60 \approx \arccos(1/3) = 70.53^\circ$ causes the following relations between the cell parameters of the monoclinic setting:

$$a = b \cdot 3^{1/2}, c = a/2, \beta \approx \arccos(-2/3)$$

The R-centered representation of the rhombohedron is directly obtained from the monoclinic

cell using the matrix $\begin{pmatrix} 0 & -1 & 0 \\ 1/2 & 1/2 & 0 \\ 1 & 0 & 3 \end{pmatrix}$.

$$a = 1.025 \text{ nm}, b = 1.027 \text{ nm}, c = 1.984 \text{ nm}, \alpha = 90.16^\circ, \beta = 90.00^\circ, \gamma = 119.94^\circ; c/a \approx 1.9337$$

In Fig. 5.6, the “monoclinic” (Fig. 5.6a) and the trigonal (Fig. 5.6b) indexing of a prominent SAED pattern are compared. The auxiliary line in Fig. 5.6a clarifies the lack of any mirror planes, when considering the intensities of the diffraction spots. The two-dimensional point group is quite clearly 6. This does not necessarily mean that the structure is trigonal or hexagonal or cubic. In fact it means that the symmetry of the structure projected along the employed zone axis is very close to $p6$.

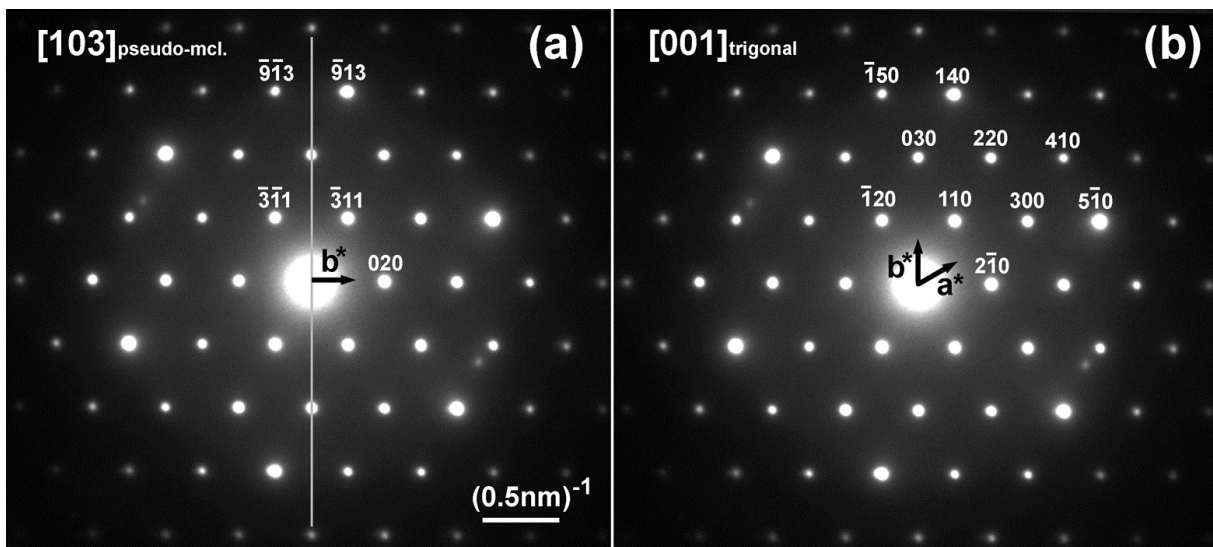


Fig. 5.6. SAED pattern of the γ -AlFeSi phase, indexed using (a): the published C-centered monoclinic cell. Note that intensities hkl and $h-kl$ are different; (b): the R-centered hexagonal cell. Note the six-fold symmetry and the lack of mirror planes.

As the reciprocal space of monoclinic space groups displays the symmetry $2/m$, even if the point group of the structure is 2 or m , the auxiliary line in Fig. 5.3a should represent the mirror plane. As this is not the case, monoclinic symmetry is excluded. Hence the structure is either trigonal or triclinic. The lack of mirror planes limits the possible space groups to $R\bar{3}$, $R3$, \bar{P} or $P\bar{1}$. (In space group $R32$ mirror planes are missing, despite that the diffraction pattern of zone $[001]$ displays the symmetry $6m$).

5.1.3.1.2 Proposed Structure Type for γ -AlFeSi (τ_2 intermetallic)

A structure determination of γ -AlFeSi has not yet been published. A reason might be that a structure determination based on X-ray powder data is complicated by the fact that the angle α of the rhombohedral setting of the published cell is very close to $\arccos(1/3)=70.529^\circ$ (the well-known angle between the faces of a tetrahedron). This implies that for the hexagonal setting the ratio $c/a \approx 1.9337$ is very close to $c/a = (15/4)^{1/2} = 1.93649$, and that the value of $d^2 = d^2(a,h,k,l)$ is very close to $d_{hkl}^2 = (15/4) \cdot a^2 / K_{hkl}$ with $K_{hkl} = 5 \cdot (h^2 + k^2 + hk) + l^2$.

All powder lines with common K_{hkl} coincide. Since K_{hkl} is an integer the situation is similar to the cubic case where non-equivalent lines with a common value of $(h^2 + k^2 + l^2)$ coincide. In contrast, in the hexagonal case coincidence only occurs for a very special value of the free parameter c/a . Deviations from this value cause an increased splitting of the multiplets with increasing K_{hkl} . However, if this value is exactly met, the overlap is perfect. Coincidences are much more abundant than in the cubic system, in particular for low h, k, l . Among the first 400 lines of a hexagonal R -centred lattice there are only 10 ‘‘singulets’’ (hkl and $ik-l$ counted as one line): 101, 110, 015, 122, 131, 315, 324, 505, 345, 5 1 10. Multiplets with multiplicities > 2 are the rule. For $K_{hkl} = 261$ ($d=0.123$ nm), e.g., the 7 lines 6 2 1, 7 0 4, 3 5 4, 6 0 9, 4 2 11, 3 1 14, 1 0 16 coincide. For a monoclinic setting there are no singulets at all.

By a search-match procedure which uses an indexibility criterion (and therefore is not sensitive to the setting of cells) a scan through a crystal structure data base was performed. If only phases containing nothing but metals and metalloids are included a group of nearly isostructural rhombohedral phases can be found. The space group of these phases is $R\bar{3}$. (The τ_2 phase was not contained in the data base.) The matches are:

- $\text{Mo}_{30.4}\text{Co}_{51.3}\text{Cr}_{18.3}$: 1.0903 nm, 1.9342 nm, $c/a = 1.774$, Komura et al. (1960) [94]
- $\epsilon\text{-Mg}_{23}\text{Al}_{30}$: 1.2825 nm, 2.1748 nm, $c/a = 1.686$, Samson et al. (1968) [95]

- $\text{Mn}_{85.5}\text{Si}_{14.5}$: 1.0871 nm, 1.9180 nm, $c/a = 1.764$, Shoemaker et al. (1978) [96]

In 1951 the Mo-Co-Cr phase was first encountered and named “*R* phase” by Rideout et al. [97]. Even though later the structure turned out to be trigonal *R*-centered the name “*R*-phase” does *not* stand for this fact. In 1960 the structure was determined by Komura et al. [94]. If $\text{Al}_{68.6}\text{Fe}_{15.7}\text{Si}_{15.7}$ (Table 5.2) is written $(\text{Al,Fe})_{84.3}\text{Si}_{15.5}$ the similarity to $\text{Mn}_{85.5}\text{Si}_{14.5}$ [96] becomes evident. There is additional crystallographic evidence for a relationship: In Fig. 5.3b, reflection 140 and its equivalents, which underline the six-fold symmetry, are clearly the strongest in zone [001]. This matches the findings in the Fo-Fc listings reproduced in Refs. [94] and [95]. (In Ref. [95], hkl has to be replaced by $kh-l$ due to a different setting of the structure.)

Furthermore we compared calculated powder diffractograms of the *R* phases using the parameters from [94], [95] and [96] with a measured powder diffractogram of an alloy $\text{Al}_{61}\text{Fe}_{22}\text{Si}_{17}$ which was given to us by Prof. J. C. Schuster (Vienna). The predominant phase in this material is γ -AlFeSi. A common feature is a very characteristic group of strong lines between $d \approx 0.19$ nm and $d \approx 0.22$ nm. However, although the calculated intensity for the doublet 202, 113 at 0.404 nm displays the highest intensity in the range $d > 0.22$ nm, it is very much weaker than the observed line. Nevertheless these findings corroborate the view point that the structure of the γ -AlFeSi phase is at least strongly related to the structure of the *R* phases. As stated in Refs. [94-96] these structures are built from 11 sites. The *R*-centered setting of the cell contains 159 atoms, many sites with mixed occupancy. The structures exhibit 12- to 16-fold atomic coordination and only tetrahedral interstices.

5.1.3.2 Sr-modified high-purity alloy

Figure 5.7 shows bright-field TEM images and the SAED patterns of different types of intermetallic phases embedded in the eutectic matrix of the pure alloy modified by Sr. The corresponding SAED images of every intermetallic phase along the zone axes [111], [110] and $[\bar{1}11]$ are shown in the inset. The intermetallic phase in Fig. 5.7a is a Fe-rich α phase. Its chemical composition is close to $\text{Al}_{14}\text{Fe}_3\text{Si}_2$ as measured by EDX in the TEM. According to the SAED the lattice parameter of the bcc structure is $a = 1.253$ nm. The phase located in the center of Fig. 5.7b is a Fe-rich δ phase with composition Al_4FeSi_2 . The lattice parameters of the tetragonal phase are $a = 0.6146$ nm and $c = 0.9509$ nm. Both α and δ phases have also been observed in the commercial Sr-modified alloy (containing further elements) investigated in [19].

The third intermetallic phase is located in the center of Fig. 5.7c. By SAED it was identified as the γ -AlFeSi phase. The existence of this phase in the Sr-modified pure alloy is therefore confirmed. Its chemical composition is about $\text{Al}_{4.65}\text{FeSi}$, which is close to that measured in the unmodified alloy. Its crystal structure is trigonal R-centered, as in the unmodified pure alloy. Of a total of 84 observations the following numbers of sightings of phases occur: α phase: 4; γ phase: 5; and δ phase: 75. The most frequently occurring phase in the Sr-modified alloy is therefore the δ phase, unlike in the unmodified pure alloy, where the α phase is dominant.

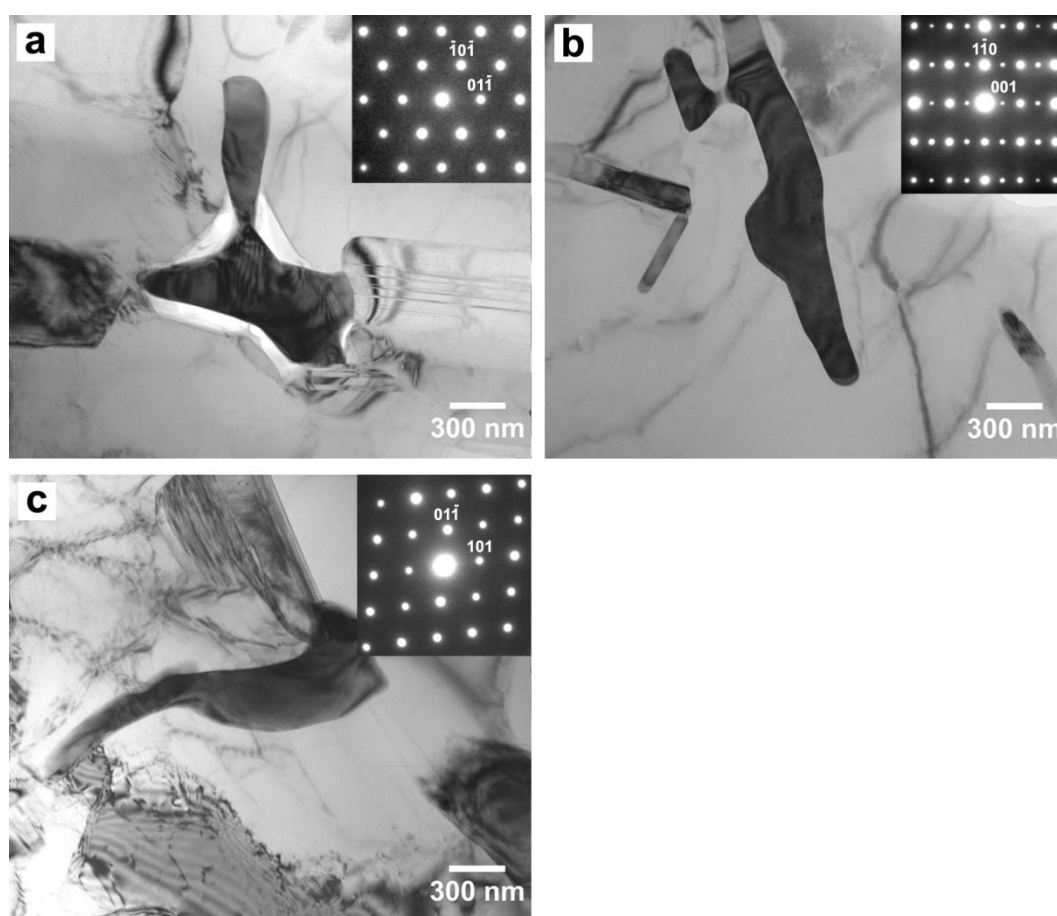


Fig. 5.7. Bright-field TEM images of intermetallic phases (dark in contrast) found in the Sr-modified pure Al-10Si-0.3Fe alloy: (a) an α -intermetallic and the corresponding diffraction pattern along $[111]$ of the bcc structure in the inset; (b) a δ -intermetallic and the SAED pattern along $[110]$ of the trigonal R-centered structure; (c) a γ -intermetallic and the SAED pattern along $[\bar{1}11]$ of the trigonal R-centered structure.

In the present study, neither the primary β phase nor a refinement of primary β plates has been observed, in contrast to the observations reported in Refs. [17, 31, 33, 66]. The formation of the intermetallic β phase in pure alloys during solidification depends on many

parameters as reported in Ref. [29]. According to this study the β phase forms at cooling rates up to 50 K/s during solidification in alloys containing about 2 wt.% Si and 0.25 wt.% Fe [29]. For alloys with Si contents around 10 wt.% Si the β phase has been found in samples cooled at < 5 K/s. The present alloys have been solidified at a cooling rate of ~ 8 K/s and the β phase cannot be observed. Based on the results in this study, our conclusion is that without commercial impurities the formation of the intermetallic β phase can be observed neither in the unmodified nor in the Sr-modified alloy. Chemical and crystallographic information of the intermetallic phases observed in the Sr-modified alloy are given in Table 5.2.

5.1.3.3 Unmodified commercial alloy

Figure 5.8 shows the bright-field TEM images and corresponding SAED patterns of different types of intermetallic phases in the unmodified commercial alloy. Fig 5.8a displays an α phase with corresponding SAED pattern along [001] of the bcc structure. This α phase exhibits a more complex morphology, known as fish skeleton or complex “Chinese script”. It is thin and compact, corresponding to an observation previously reported [18] and probably due to various impurities in the alloy. The chemical composition of the α phase is similar to that in the unmodified pure alloy, which is $\text{Al}_{14}\text{Fe}_3\text{Si}_2$ as measured by EDX in the TEM. According to SAED the lattice parameter of the bcc structure is $a = 1.2487$ nm.

Figure 5.8b displays a needle-like morphology of the δ intermetallic phase in bright field TEM images and the corresponding SAED pattern along the zone axis [010] of the tetragonal structure in the inset of Fig. 5.8b. The chemical composition of the δ phase is $\text{Al}_{3.6}\text{FeSi}_2$ as measured by EDX in the TEM which is similar to that in the pure alloy. According to SAED the lattice parameters of the tetragonal phase are $a = 0.6092$ nm and $c = 0.9538$ nm.

The third intermetallic phase in the unmodified commercial alloy is the β intermetallic phase which is shown in Fig. 5.8c. The chemical composition of the β phase is close to $\text{Al}_{4.7}\text{FeSi}$ as measured by EDX in the TEM, which corresponds to Al_5FeSi , which has often been designated as $\text{Al}_{4.5}\text{FeSi}$ [21, 22]. The morphology of the β phase has been described as needle-like or acicular in 2D and as very large interconnected plates or blades in 3D. However, central oxide cracks in the middle of the β phase [62], branching of β phase or β distributing around oxides [68] are not found in the present work. Compared to the δ phase, which also has a platelet appearance, the β intermetallic generally exhibits coarser platelets

without any curved morphology [98]. Many crystallographic structures of the β phase have been reported in the literature [16, 17, 21-24]. The corresponding SAED pattern in Fig. 5.8c determines the lattice parameters of the β phase along the [100] zone axis of the monoclinic phase, with $a = 0.6148$ nm, $b=0.6145$ and $c =2.0808$ nm and $\beta=91^\circ$. This phase was previously reported to contain highly faulted crystal structure with the (001) planar defects lying parallel to the plane of the platelet [16, 22], which is not found in the current alloy. Neither the multiphase composites of an A-centered orthorhombic phase [17] nor the heavily-faulted tetragonal phase [23], nor the B-centered orthorhombic [24] were found in the present alloy.

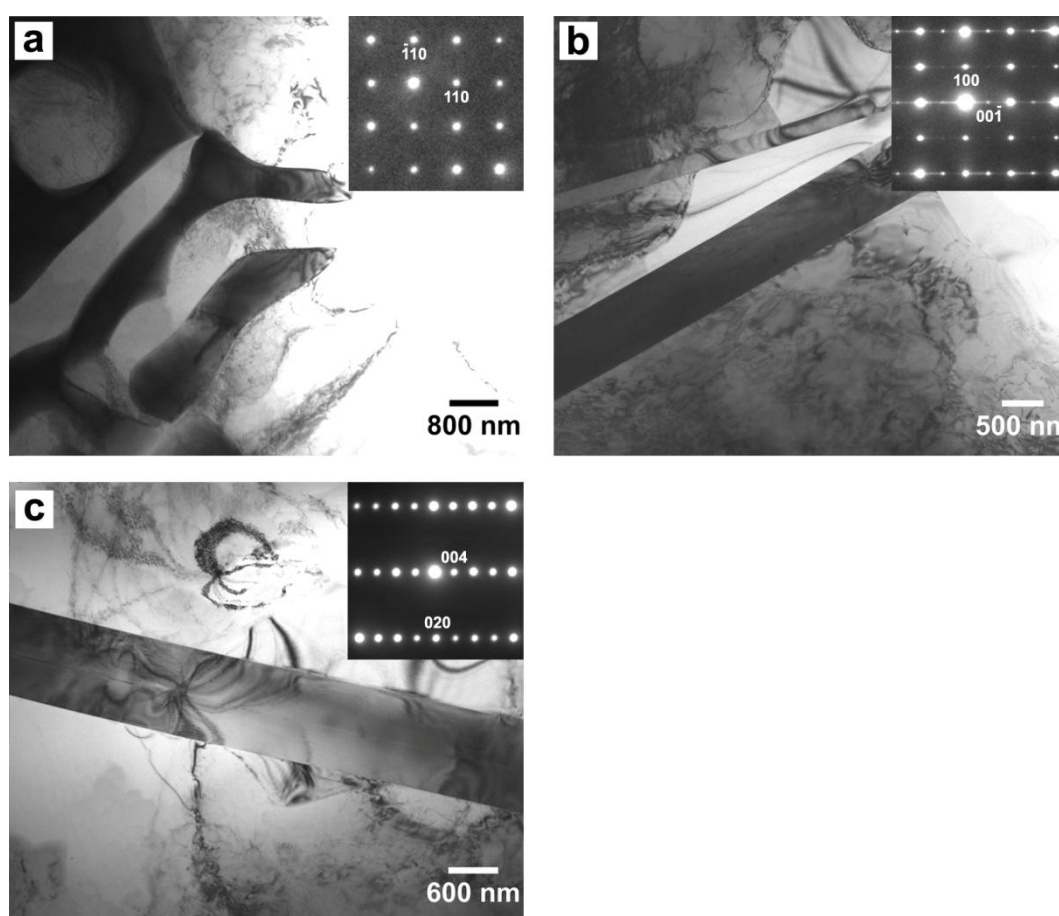


Fig. 5.8. Bright-field TEM images of the intermetallic phases (dark in contrast) found in the commercial Al-10Si-0.3Fe alloy: (a) α -intermetallic and the corresponding SAED along [001] of the bcc structure in the inset; (b) δ -intermetallic and the corresponding [010] zone axis of the tetragonal structure in the inset; (c) new Fe-rich phase identified as β -phase and the corresponding [100] zone axis of monoclinic structure in the inset.

The current investigation contains the observation of 36 intermetallics in total. The numbers of observations of every phase are: $\delta=20$; $\alpha=8$; and $\beta=8$. Obviously, the most frequently occurring phase is the δ phase. It should be noticed that in this small number of investigated intermetallic phases γ phase is not observed, but this does not mean that the γ phase does not exist in the unmodified commercial alloy, since limited amount of γ phases are too difficult to be found in current observation.

5.1.3.4 Sr-modified commercial alloy

Figure 5.9 shows bright-field TEM images and SAED patterns of different intermetallic phases in the Sr-modified commercial alloy. The dark contrast of the bright-field TEM images in Fig. 5.9a, 5.9b and 5.9c shows the morphology of “Chinese script” α phase and γ phase, and the platelet-like δ phase in the inset. The corresponding SAED patterns are displayed in Fig. 5.9 for every intermetallic phase along the zone axis $[\bar{1}13]$, $[152]$ and $[010]$, respectively, and the parameters of the phases are as follows: for the bcc structure α : $a=1.2633$ nm; for the R-centered trigonal γ phase: $a=0.8873$ nm, $\alpha =72.15(2)^\circ$; for the tetragonal δ phase: $a=0.6118$ nm, $c=0.9594$ nm.

The Al_2SrSi_2 phase was not found in the Sr-modified Al-Si alloys in contrast to the observations reported in Refs. [11, 66]. Many researchers have found this phase in Sr-modified Al-Si commercial alloy.

In the current specimens 112 observations of intermetallic phases have been made, i.e. 104 times δ phase, 6 times α phase, and 2 times γ phase. The common β phase is not present in this investigated sample.

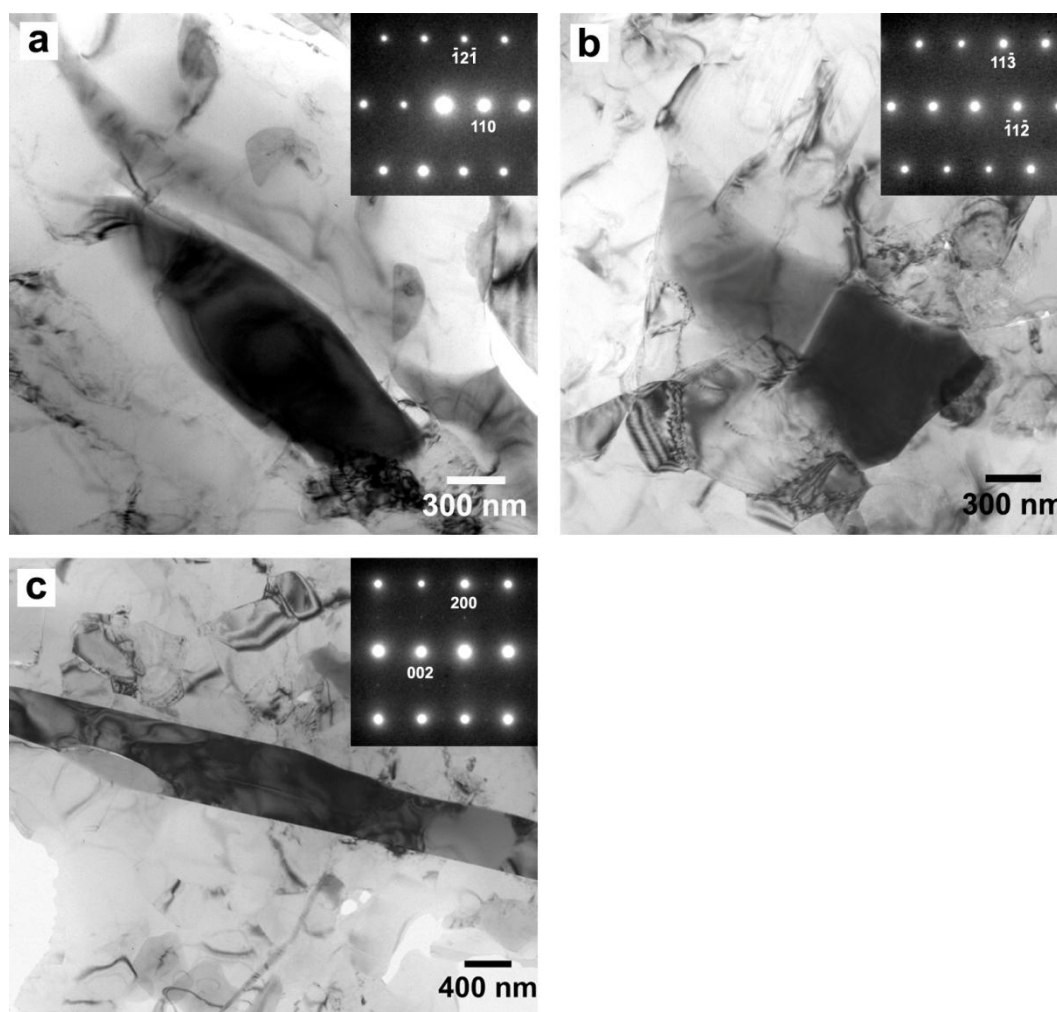


Fig. 5.9. Bright-field TEM images of intermetallic phases (dark in contrast) found in the Sr-modified commercial Al-10Si-0.3Fe alloy: (a) α -intermetallic, visible in the center and the corresponding SAED pattern along the $[\bar{1}13]$ bcc zone axis shown in the inset; (b) γ -intermetallic and the corresponding SAED pattern along the $[152]$ trigonal R-centered zone axis shown in the inset; (c) δ -intermetallics and the corresponding SAED pattern along the $[010]$ tetragonal zone axis shown in the inset.

5.1.3.5 Summary of intermetallic phases

In the Al-10Si-0.3Fe alloy, intermetallic phases are characterized in the four types, i.e. in the unmodified pure alloy, the Sr-modified pure alloy, the unmodified commercial alloy and the Sr-modified commercial alloy, including the microstructure, the crystal structure and the chemical composition.

5 Results

The statistic numbers of the intermetallic phases investigated in a small region of every alloy are listed in Table 5.3. According to these statistics, the α phase is dominant in the unmodified pure alloy and the δ phase is absolutely dominant in the Sr-modified alloy, no matter whether it is the pure alloy or the commercial alloy. In the unmodified commercial alloy, the intermetallic phases are all comparable in both size and numbers as observed by OM and SEM. It is likely that the γ phase exists in all of the Al-10Si-0.3Fe alloys like the α phase. Based on bright field TEM observation, β exists only in the unmodified commercial alloy.

Table 5.2 lists the lattice parameters and chemical compositions of every intermetallic phase in every alloy, the lattice parameters and the chemical composition of these intermetallic phases, e.g. α phase or δ phase, are not necessarily consistent in all the four alloys. There are small deviations between these alloys, since the Sr-modification and impurities influence the formation of the intermetallics in some ways.

Table 5.2 Detailed data of the investigated intermetallic phases in the Al-10Si-0.3Fe alloys.

Al-10Si-0.3Fe alloy	Phases	Composition/ at. %			Crystal structure	Lattice parameter /nm, Angle / °
		Al	Fe	Si		
unmodified pure alloy	α	74.11 \pm 2.42	15.71 \pm 2.31	10.17 \pm 1.18	bcc	a=1.2531 \pm 0.0059
	γ	68.54 \pm 1.22	15.73 \pm 0.61	15.73 \pm 0.61	trigonal	a=0.8873; α =72.15(2)°
Sr-modified pure alloy	α	75.75 \pm 2.25	14.50 \pm 1.30	9.75 \pm 0.95	bcc	a=1.2560 \pm 0.0050
	γ	71.14 \pm 4.79	15.31 \pm 2.81	13.55 \pm 1.98	trigonal	a=0.8873; α =72.15(2)°
	δ	58.61 \pm 6.33	14.88 \pm 2.80	26.51 \pm 5.25	tetragonal	a=0.6147 \pm 0.0057; b=0.9521 \pm 0.0064
unmodified commercial alloy	α	74.11 \pm 2.42	15.71 \pm 2.31	10.17 \pm 1.18	bcc	a=1.2487 \pm 0.0042
	γ	68.54 \pm 1.22	15.73 \pm 0.61	15.73 \pm 0.61	trigonal	a=0.8873; α =72.15(2)°
	δ	58.61 \pm 6.33	14.88 \pm 2.80	26.51 \pm 5.25	tetragonal	a=0.6092 \pm 0.0024; b=0.9538 \pm 0.0045
	β	75.75 \pm 2.25	14.50 \pm 1.30	9.75 \pm 0.95	monoclinic	a=0.6148 \pm 0.0036; b=0.6145 \pm 0.0048; c=2.0808 \pm 0.0029; β =91(2)°
Sr-modified commercial alloy	α	71.14 \pm 4.79	15.31 \pm 2.81	13.55 \pm 1.98	bcc	a=1.2633 \pm 0.0025;
	γ	68.54 \pm 1.2	15.73 \pm 0.61	15.73 \pm 0.61	trigonal	a=0.8873; α =72.15(2)°
	δ	58.61 \pm 6.33	14.88 \pm 2.80	26.51 \pm 5.25	tetragonal	a=0.6118 \pm 0.0032; b=0.9594 \pm 0.0035

Table 5.3. Statistic numbers and sizes of the investigated intermetallic phases in the Al-10Si-0.3Fe alloys.

	α		γ		δ		β	
	numbers	Size (μm)	numbers	Size (μm)	numbers	Size (μm)	numbers	Size (μm)
unmodified pure alloy	68	0.92-3.65 0.86-0.90	4	0.36-2.60 1.21-3.00	-	-	-	-
Sr-modified pure alloy	4	0.34-1.20 1.14-1.63	5	0.29-0.74 0.39-1.97	75	0.12-0.67 1.24-8.27	-	-
unmodified commercial alloy	8	1.55-12.00 2.40-42.27	?	?	20	0.50-2.00 8.00-40.0	8	0.56-1.51 18.1-31.8
Sr-modified commercial alloy	6	0.66-1.01 2.21-5.47	2	0.72-1.16 2.04-5.69	104	0.36-0.61 1.83-12.5	-	-

Note: “-” means no such phase found in alloy. “?” means that it was not found but suspected to exist.

5.2 Three-dimensional visualization of intermetallic phases (ex-situ tomography)

At room temperature, samples of pure Al-10Si-0.3Fe alloy, Sr-modified pure Al-10Si-0.3Fe alloy, commercial Al-10Si-0.3Fe alloy and Sr-modified commercial Al-10Si-0.3Fe alloy were visualized by synchrotron tomography performed at the ESRF. FIB tomography was also carried out in order to obtain more information, since details of intermetallic phases in these alloys are beyond the resolution limit of the synchrotron tomography.

5.2.1 Unmodified high-purity alloy (FIB tomography)

To examine the morphology of the intermetallic phases and the corresponding eutectic Si in 3D, a FIB tomogram was created in the region where intermetallic phases and eutectic Si are present. Stacks of images such as the ones shown in Fig. 5.3 were used for a 3D visualization of the morphology of the intermetallic phases. The obtained 3D morphology is shown in Fig. 5.10 where both the intermetallic phases with and without corresponding eutectic Si plates are displayed. The eutectic Al matrix and the dendrites have been omitted for the sake of clarity.

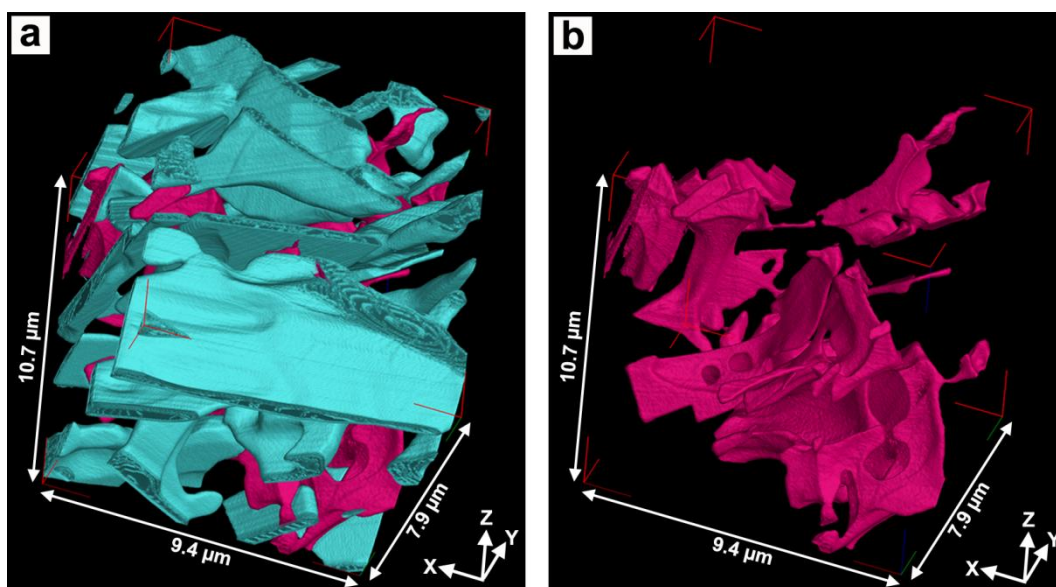


Fig. 5.10. Three-dimensional visualization of the microstructure in the unmodified pure alloy obtained by FIB tomography: (a) eutectic Si (in cyan) and intermetallics (in magenta); (b) intermetallics (in magenta).

As shown in Fig. 5.10a, the intermetallic phases and the closely attached corresponding eutectic Si plates were visualized in the unmodified high-purity alloy within an investigated volume of $9.4 \times 7.9 \times 10.7 \mu\text{m}^3$. The eutectic Si plates are interconnected, forming a network in which the intermetallic phases are embedded. The observed thickness range of Si plates is about 114-778 nm. All the plates are far longer than the investigated volume, i.e. larger than $10.7 \mu\text{m}$. The estimated volume fractions of eutectic Si and intermetallic phases in the investigated volume are 15.1 and 5.6 vol.%, respectively.

By omitting the eutectic Al matrix, the dendrites and the eutectic Si, it is possible to closely observe a full view of the intermetallic phases. Fig. 5.10b demonstrates only the morphology of the intermetallic phases in three-dimension. As described above, the intermetallic phases found in the unmodified high-purity alloy are α phase and γ phase. Both of them exhibit “Chinese Script” morphology in 2D, and we expect that their morphology in 3D is also similar. In 3D the shape of the α and possible γ intermetallic phases resembles no longer “Chinese script”, but turns out to be a very complex structure, which is present as a highly concentrated branched network in the investigated volume. The complex structure of the α phase and the γ phase with highly curved surfaces reflects the impressions of the collided eutectic Al and Si crystals. In some regions the intermetallics form edges and/or seem to serve as junction parts to the coarse eutectic Si. The thinnest width of those edge-forming or junction-building intermetallics in the investigated volume is about 80 or 130 nm. For comparison: the size of one intermetallic is far more than $10.7 \mu\text{m}$.

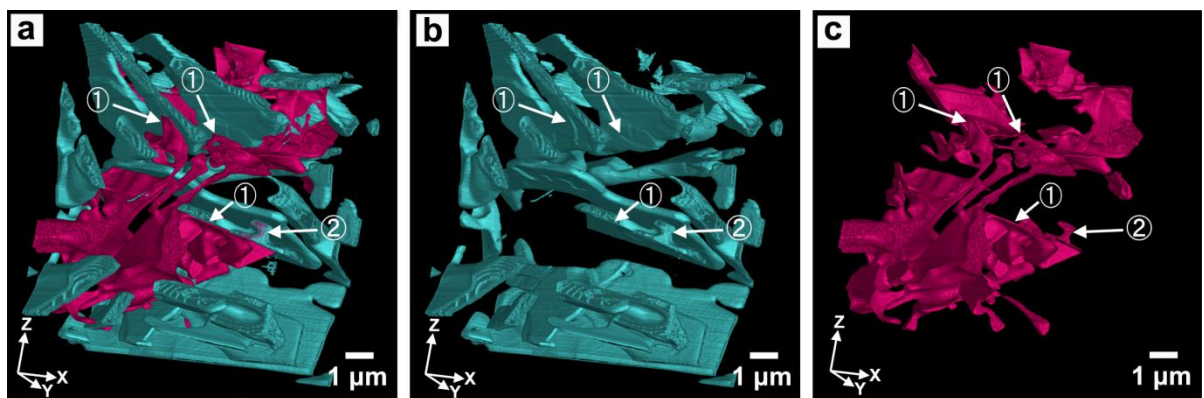


Fig. 5.11 Three-dimensional FIB tomography visualization of eutectic Si and intermetallic phases in unmodified high-purity alloy: (a) eutectic Si and intermetallics; (b) the corresponding eutectic Si; (c) the corresponding intermetallics. Arrow 1 indicates intermetallics closely attached to a coarse eutectic Si plate; arrow 2 indicates an intermetallic that is covered by eutectic Si. (eutectic Si in cyan and intermetallics in magenta).

It can also be observed that the intermetallic phases contain some so called convoluted branched structure [34] and holes extending through the intermetallics, see Fig. 5.10b. In combination with Fig. 5.10a and Fig. 5.11, it can be seen that the Al matrix fills those convoluted structures and penetrates through the holes in the intermetallics. In Fig. 5.11, as marked in the images, some intermetallic phases are attached to the eutectic Si (arrows 1), and some intermetallics are covered by eutectic Si (arrow 2).

5.2.2 Sr-modified high-purity alloy (FIB tomography)

Figure 5.12a displays a 3D FIB tomography of the eutectic Si and the corresponding intermetallic phases within an observed volume $10.9 \times 9.9 \times 9.7 \mu\text{m}^3$. The fine fibers of eutectic Si are often described as seaweed or coral structure [36, 70]. However, they are not all interconnected and do not form a unique large network. Fibers of eutectic Si are interspersed with extremely large intermetallics plates and tiny globular intermetallics. The observed thickness range of the Si seaweeds is about 200-300 nm; the estimated length of most Si fibers is in a range from 0.4 to 4 μm . It can also be observed from Fig. 5.12a that the

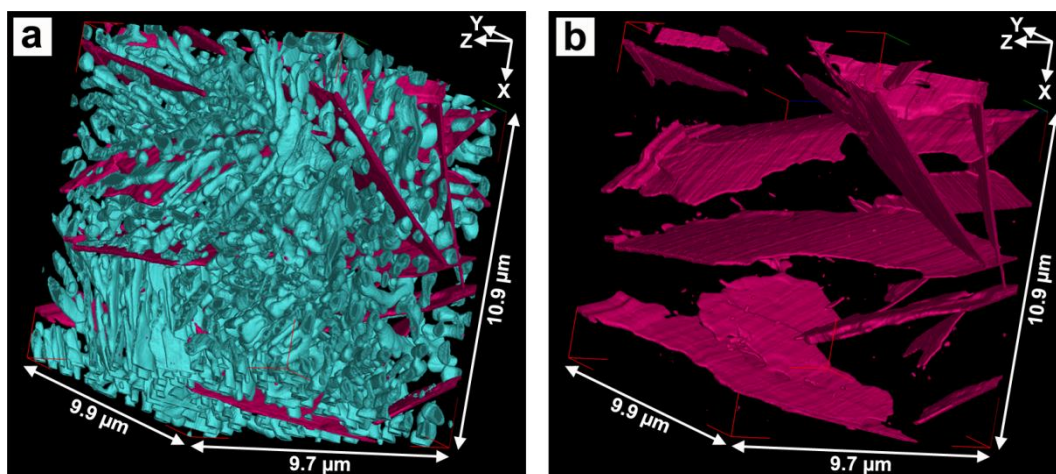


Fig. 5.12 Three-dimensional visualization of the microstructure in the Sr-modified pure alloy obtained by FIB tomography: (a) eutectic Si (in cyan) and intermetallics (in magenta); (b) intermetallics (in magenta).

eutectic Si fibers tend to have the same orientation in a local region and are connected by transition regions. In parts where the Si fibers with different orientations meet, the intermetallics plates and tiny globular intermetallics are embedded. It has previously been

reported [10, 55] that three distinct Si regions with different morphologies and sizes can be distinguished and that they separate the α phase from the δ phase. However, the cross section of this particular region in [10] has probably been misinterpreted because of the 2D effect

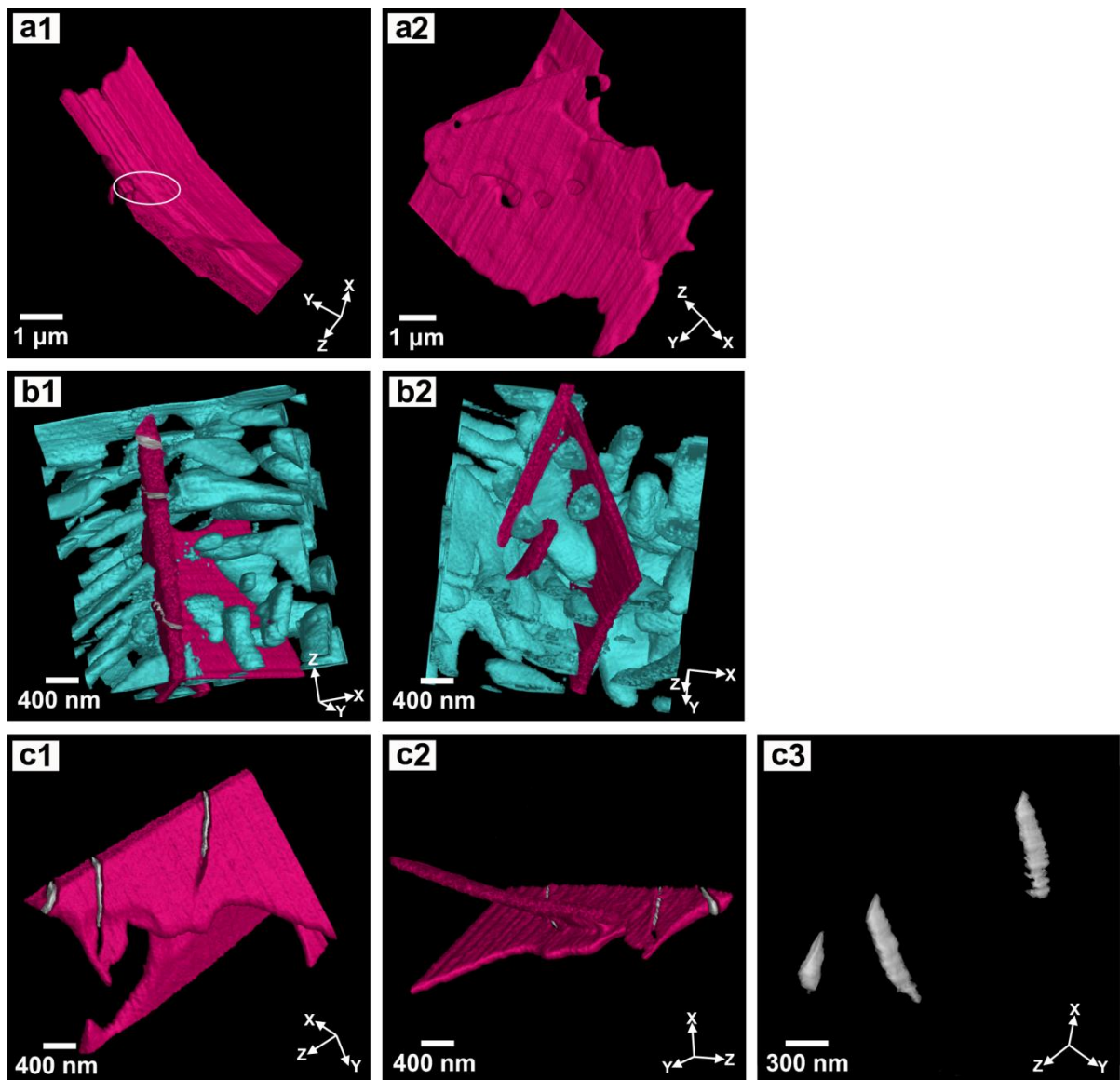


Fig. 5.13 Microstructural features of the δ phase in the modified pure alloy: (a1) a bent Al line inside the δ phase; (a2) eutectic Al passing through the δ phase; (b1) eutectic Si, having a similar orientation at one end, touching a δ plate; (b2) eutectic Si sitting in the corner of a branch of a δ plate; (c1) pores looking like long stripes in the δ phase; (c2) a branch of a δ plate intersecting with the one containing long pores; (c3) the pores extracted from (c1) and (c2). (eutectic Si in cyan, intermetallics in magenta and pores in gray, Al in black).

5 Results

and has not been recognized as differently oriented fibers of one and the same type of Si. The estimated volume fractions of the eutectic Si and the intermetallic phases are 14.8 and 4.7 vol.%, respectively.

As can be seen from Fig. 5.12b, the morphology of the δ phase consists of thin interconnected platelets. The thickness of the δ phase is in the range of 83-314 nm and their length exceeds 10.9 μm . The so called "bent phenomenon" as previously reported [40] can be observed: highly curved surfaces reflect the impressions of the collided eutectic Al and the Si crystals.

The size range of the spherical α and γ phase is about 49-571 nm. Most phases are around 57-130 nm length. Simple comparison can tell that the δ phase is at least 100 times larger than both the α and γ phase in the modified pure alloy.

Figure 5.13(a1) shows that an Al rich, curved shape was found inside the plates. In the future they will be called Al lines. The length of these usually curved Al lines is around 700 nm. Fig. 5.13(a2) shows that the eutectic Al can go through the plates. Fig. 5.13(b1-b2) shows eutectic Si fibers having a similar orientation at one end, touching the δ plate, and eutectic Si sitting in the corner of a branch of a δ plate. The δ plate is the meeting place of two differently oriented Si fibers coming from two different sides. The Si fibers at one end of the plate block the plate. It has also been observed that Si fibers block the edges of a δ plate extension. In some narrow corners of intersecting δ plates, eutectic Si and Al form a complex morphology.

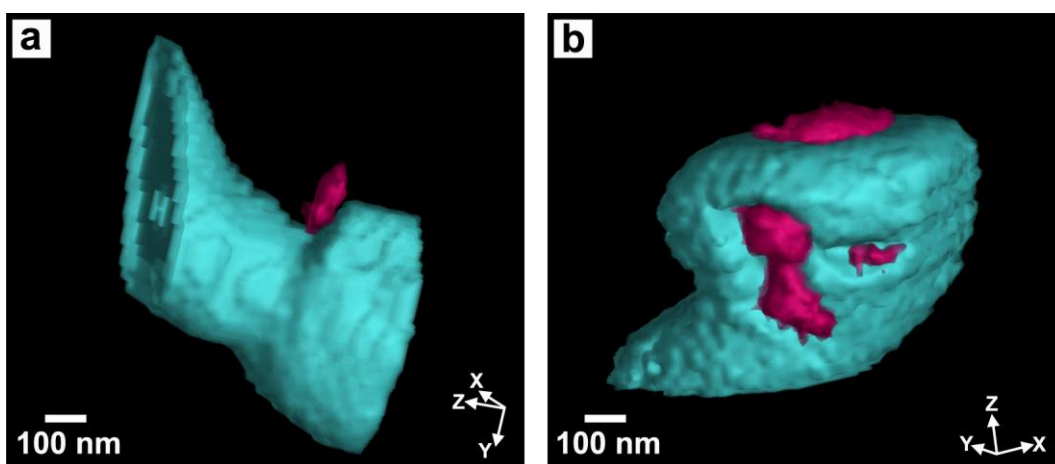


Fig. 5.14 The local microstructure features of the α phase in Sr-modified high-purity alloy: (1) α phase (in magenta) closely attached to the surface of eutectic Si (in cyan) and (b) three α phases embedded in the same eutectic Si.

There are also some defects in the δ plate. Figure 5.13(c1-c3) displays that the δ phases contain pores, exhibiting a flat-column morphology, and that the branch intersecting the plate and the corresponding pores does not influence the growth of the pores in the δ plate. The length of these pores is more than 850 nm, the width about 230 nm, and the thickness around 60 nm. The volume fraction of the pores in the observed volume $10.9 \times 9.9 \times 9.7 \mu\text{m}^3$ is smaller than 0.01%.

Figure 5.14a-b shows that the α phase and the γ phase are either closely attached to the surface of the eutectic Si or partly embedded in the eutectic Si. Sometimes more than one α phase or γ phase is attached to or embedded in eutectic Si.

Three-dimensional microstructure of unmodified commercial alloy is not shown here because dimensions of phases are too large for FIB tomography.

5.2.3 Sr-modified commercial alloy (FIB tomography)

Figures 5.15(a) and 5.15(b) show a 3D FIB tomography reconstruction of the eutectic Si and the corresponding intermetallic phases within the observed volume of $16.9 \times 14.8 \times 8.1 \mu\text{m}^3$. The eutectic Si in the modified commercial alloy exhibits a more complicated morphology of fibers than in the pure alloy, and they are not interconnected. There are many types of Si phases: some of them are plates with fibers at the edges. The distance between two neighbouring Si phases is mostly in the range of 160-300 nm. The small distance between Si is probably the reason for the previous mistaken report that eutectic Si interconnects into a network [55]. The diameter of a Si branch is about 300-600 nm and the length of a whole Si phase is between 500 nm and 11 μm .

Figure 5.15(b) shows large, thin, highly interconnected platelets of δ intermetallics and tiny globular intermetallics distributed throughout the whole observed volume. The estimated thickness of the plates is around 21-307 nm. The observed globular α and γ intermetallics are around 35-300 nm in size. The estimated volume fractions of eutectic Si and all the intermetallic phases are 15.8 and 3.2 vol.%, respectively.

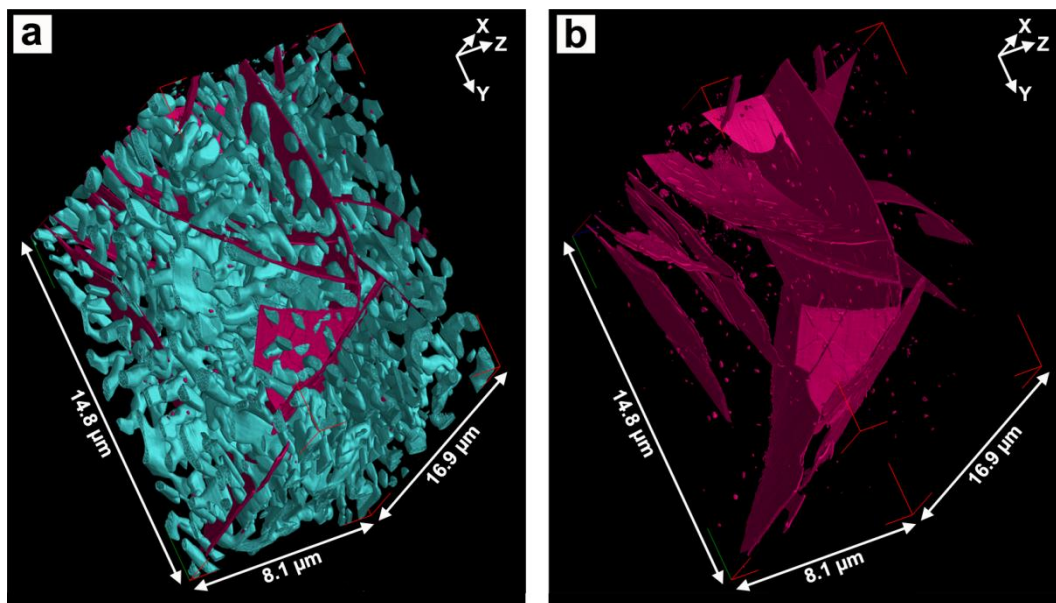


Fig. 5.15 Three-dimensional visualization of the microstructure in the modified commercial alloy obtained by FIB tomography: (a) eutectic Si (in cyan) and intermetallics (b) intermetallics (in magenta). The small dots embedded in the image are α or γ phases.

Fig. 5.16(a1) shows a part of the δ phase with a gap in the middle of the plates where eutectic Si and Al block growth. There are two separate Al lines in two parts of the δ plate. Fig. 5.16(a2) displays one δ phase closely touched and supported by eutectic Si and eutectic Al. At the place where the Si phase touches the δ plate, it is flat. Fig. 5.16(b1-b3) shows that the δ plate connects the eutectic Si phases from two sides, pressed from both sides and twisted by the eutectic Si. Fig. 5.16(c) shows that there are some Al lines contained in the δ phase.

These Al lines tend to have the same or a similar orientation, lengths of about 0.5-8 μm and widths of around 66 nm. Fig. 5.16(d) shows that the δ plate contains pores and Al lines in the same plate. Fig. 5.16(e1-e2) show one typical pore embedded in the δ plate throughout the intermetallic plates. All the pores in the observed volume $16.9 \times 14.8 \times 8.1 \mu\text{m}^3$ have a tendency to be columnar and have the same or a similar orientation. The diameters of the pores are around 100-300 nm, the lengths are around 490-3900 nm, and the estimated volume fractions of the pores in the observed $16.9 \times 14.8 \times 8.1 \mu\text{m}^3$ sized volume is 0.04 vol.%.

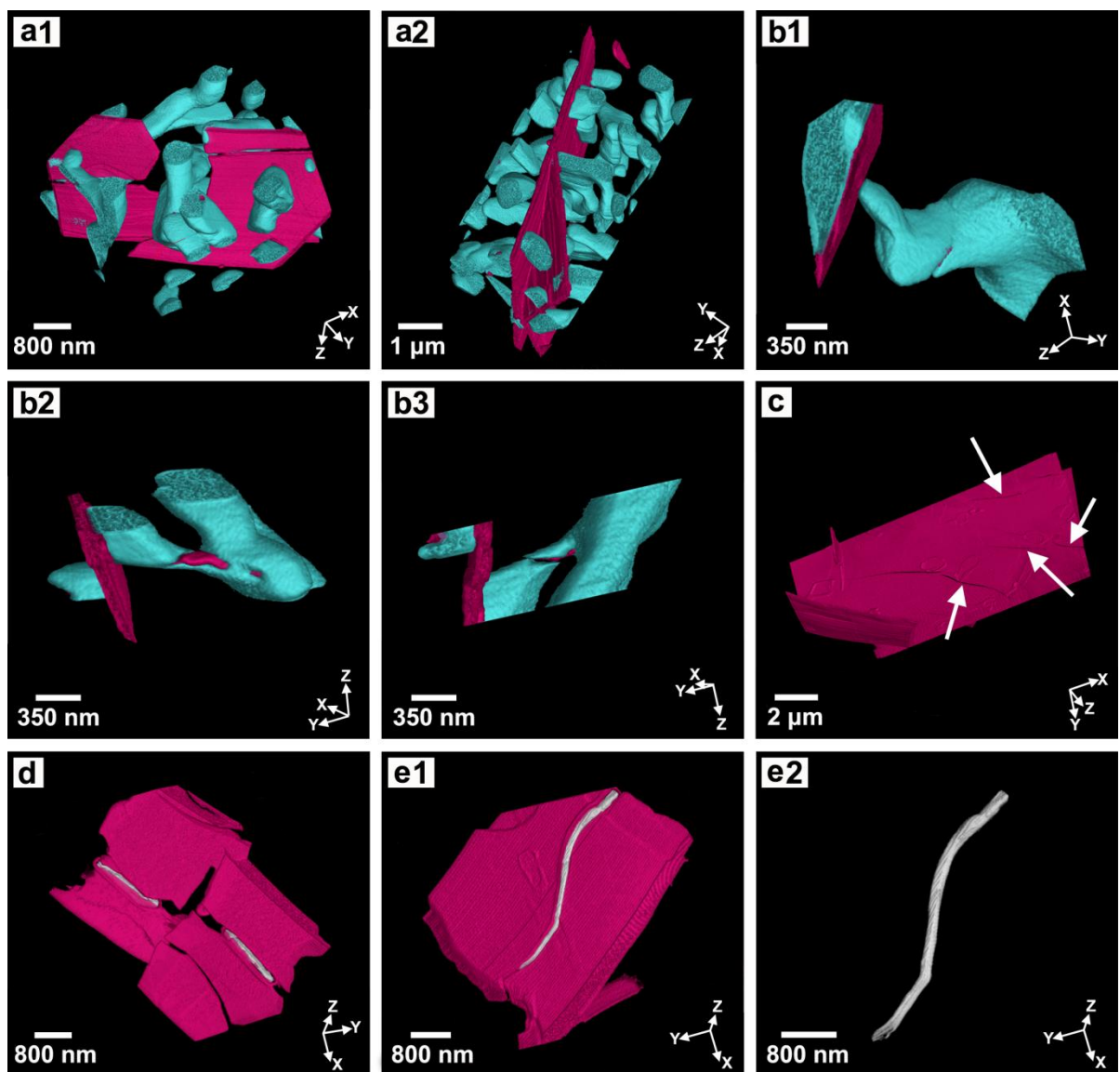


Fig. 5.16 Microstructural features of the δ phase in the modified commercial alloy: (a1) δ phase blocked by Si, and an Al line embedded in the δ phase; (a2) eutectic Si and δ phase in the middle; (b1) eutectic Si touching the δ plate at one end; (b2) Si denting on a δ phase; (b3) two eutectic Si phases twisting a δ plate; (c) Al lines in the δ plate marked by arrows; (d) pores and Al coexisting in the δ plate; (e1) pores in the δ plate; (e2) light-grey pores. (all figures: eutectic Si in cyan, intermetallics in magenta and pores in gray, Al in black).

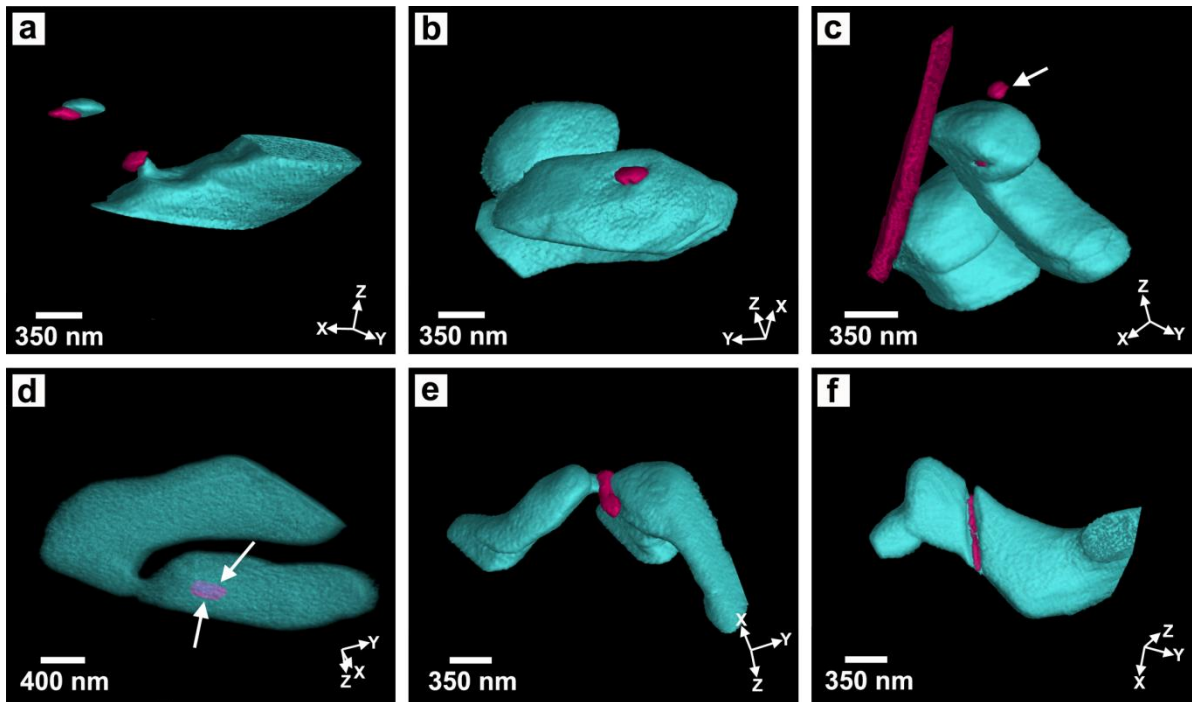


Fig. 5.17 Microstructural features of the α phase in the modified commercial alloy: (a) α phase closely attached to the surface of the eutectic Si; (b) α phase or γ phase partly embedded in eutectic Si ; (c) one α phase or γ phase embedded in the eutectic Al matrix (out of eutectic Si), marked by arrow; (d) α phase or γ phase fully inside the eutectic Si (50% transparency); (e) two eutectic Si connecting at one α phase or γ phase; (f) α or γ line embedded in eutectic Si. (eutectic Si in cyan, intermetallics in magenta and pores in gray).

It has been observed that the α or the γ phase is frequently attached to eutectic Si or partly embedded in the eutectic Si, as seen in Fig. 5.17(a-b). In addition, α phase and γ phase are also found inside the Al matrix and the eutectic Si, see Fig. 5.17(c-d). It can be observed that two Si fibers are connected by an α phase or a γ phase, see Fig. 5.17(e). Sometimes there are α or γ lines in the eutectic Si, see Fig. 5.17(f).

5.2.4 Summary (FIB tomography)

The addition of impurities and Sr to Al-10Si-0.3Fe alloy not only changes the morphology of the Si phase but also the type of intermetallic phases. The eutectic Si has platelet morphology in the pure and the commercial alloy. Its thickness in the commercial alloy is bigger than in the pure alloy. The eutectic Si has a fine fiber morphology in the modified pure alloy and the modified commercial alloy. Its size in the modified commercial alloy is

Table 5.4. The sizes of eutectic Si, intermetallics and pores in various alloys (nm).

	eutectic Si	$\alpha(\gamma)$	$\delta(\beta)$	Pore
pure alloy	Thickness \approx 114-778 Length >10700	Thinnest \approx 80 or 130 length >10700	-	-
modified pure alloy	thickness \approx 200- 300; length \approx 400- 4000	49-571(mostly 57-130)	Thickness \approx 83- 314	Width \approx 230, thickness \approx 60, length $>$ 850.
commercial alloy	Not determined			
modified commercial alloy	Diameter \approx 300- 600; length \approx 500- 11000	35-300	Thickness \approx 21- 307	Diameter \approx 100-300; length \approx 490- 3900

Note: “-” means no observation of such phase in alloy.

approximately two times larger than in the modified pure alloy. As can be seen in Table 5.4 and Table 5.5, the volume fraction of Si in the modified commercial alloy is more 1 vol.% than in modified pure alloy. α and γ phases in the pure alloy are approximately 100 times larger than in the modified pure alloy and the modified commercial alloy. In addition, the sizes of the α and γ phases in the modified commercial alloy have a slightly broader range than in the modified pure alloy. In contrast, the δ phase in the modified commercial alloy has a slightly broader size range than in the modified pure alloy, and the pure alloy has the biggest volume fraction of all intermetallic phases. The volume fraction of the pores in the modified commercial alloy is bigger than in the modified pure alloy.

Table 5.5. Volume fractions of eutectic Si, intermetallics, and pores in various alloys (vol.%)

	eutectic Si	intermetallics	pore	Volume / μm^3
pure alloy	15.1	5.6	-	$9.4 \times 7.9 \times 10.7$
modified pure alloy	14.8	4.7	< 0.01	$10.9 \times 9.9 \times 9.7$
commercial alloy	Not determined			
modified commercial alloy	15.8	3.2	0.04	$16.9 \times 14.8 \times 8.1$

Note: “-” means no observation of such phase in alloy.

5.2.5 Synchrotron tomography

In order to visualize a bigger volume of the microstructure, synchrotron tomography was performed in this work. Fig. 5.18 shows the microstructure of the as-cast alloys determined by ex-situ synchrotron tomography in (a) the pure alloy; (b) the modified pure alloy; (c) the commercial alloy and (d) the modified commercial alloy. The size of the dendrites in the

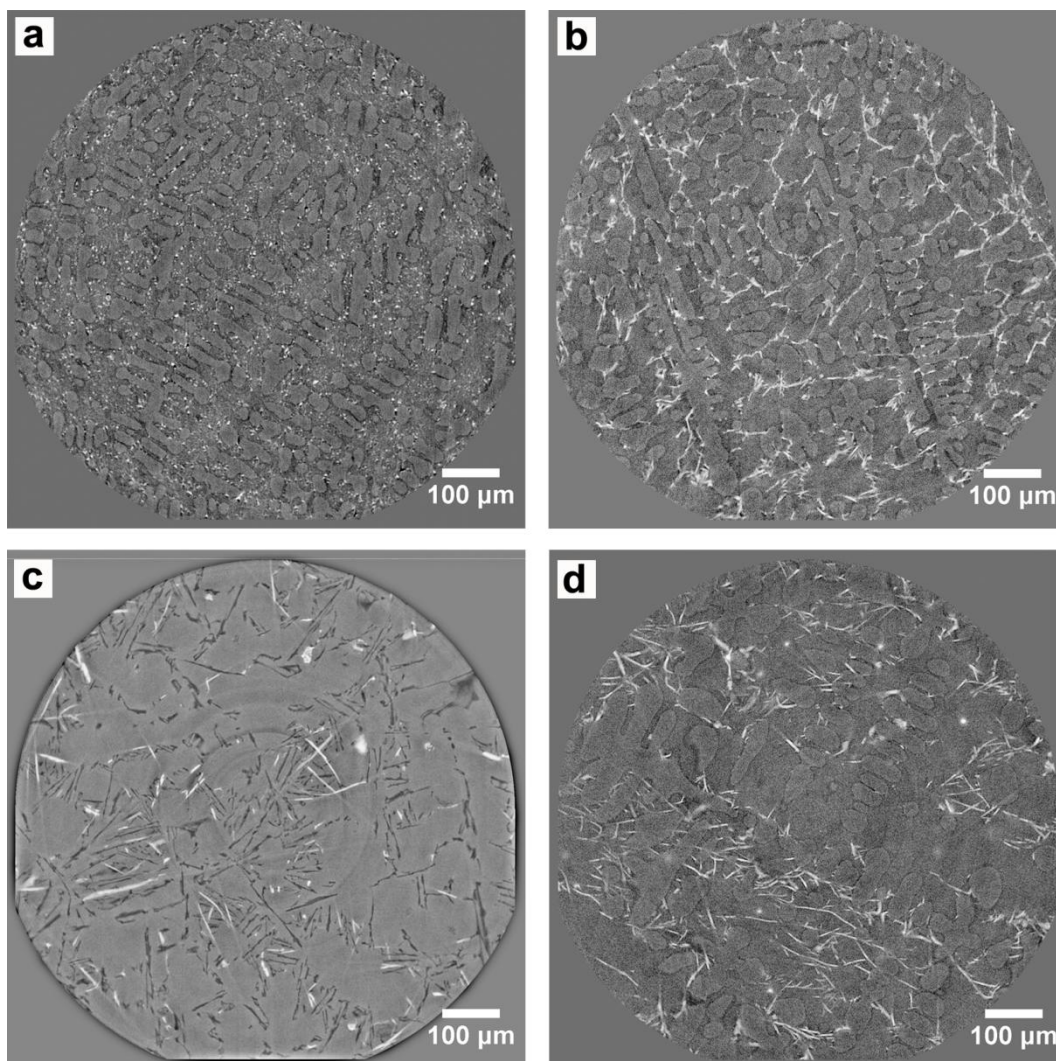


Fig. 5.18. Synchrotron tomographic visualization of the microstructure of as-cast alloys in (a) the pure alloy; (b) the modified pure alloy; (c) the commercial alloy (d) the modified commercial alloy. (Al in gray; eutectic Si in black; Intermetallics in white).

modified (pure or commercial) alloy is larger than in the unmodified (pure or commercial) alloy, while the size of the dendrites in the (modified or unmodified) commercial alloy is

larger than in the (modified or unmodified) pure alloy. Tiny spherical α and γ particles are distributed between narrow dendrites in the pure alloy. It is difficult to claim that α and γ particles do not interconnect but are isolated and distributed in the eutectic area, since the thin parts of α and γ are thinner than 500 nm, which is beyond the limitation of the

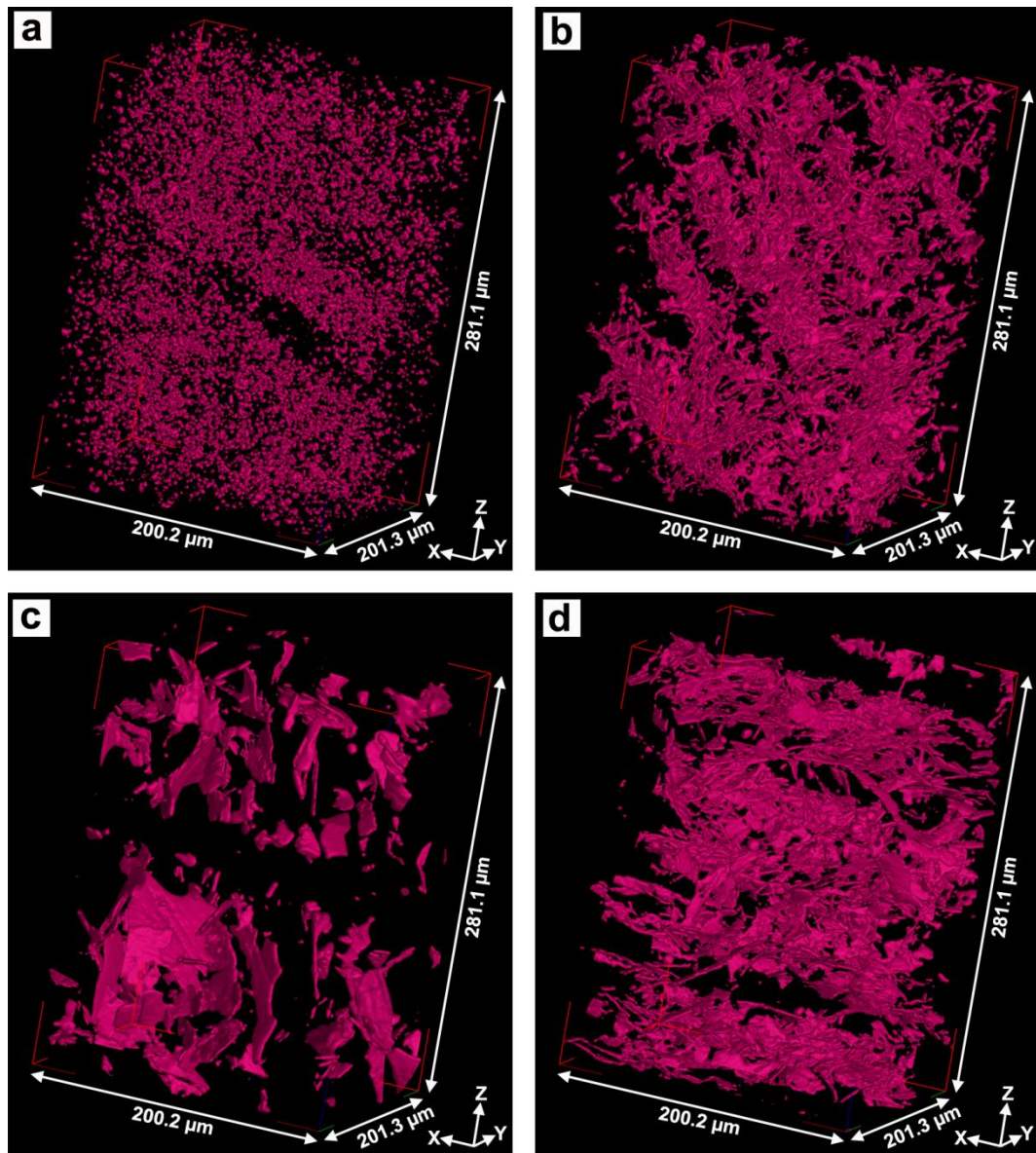


Fig. 5.19. Three-dimensional visualization of the intermetallics (magenta) of as-cast alloys by ex-situ synchrotron tomography in (a) the pure alloy; (b) the modified pure alloy; (c) the commercial alloy and (d) the modified commercial alloy.

5 Results

synchrotron tomography resolution. Despite this problem, it can still be observed that the δ phases interconnect through the whole sample in the modified pure alloy and the modified commercial alloy. The interconnected δ phases in the modified pure alloy look more fragmented than in the modified commercial alloy, but this is probably due to the thinner and shorter δ phases in the modified pure alloy.

Figure 5.19 exhibits the 3D morphology of the intermetallic phases of every alloy in the volume of $200.2 \times 201.3 \times 281.1 \mu\text{m}^3$. Because of their huge sizes, δ and β platelets and α and γ phases are clearly visible in the commercial alloy (c). These intermetallic phases do not interconnect, anyway. In the modified pure alloy (b) and the modified commercial alloy (d) the interconnection of the intermetallics is enhanced.

5.3 Three-dimensional visualization of intermetallic phases (in-situ tomography)

In this part, the microstructure is characterized by in-situ X-ray synchrotron tomography. Real time in-situ experiments were performed on all four alloys at different cooling rates: 1 K/min, 9 K/min, 30 K/min and 400 K/min.

Fig. 5.20 shows typical images of completely solidified samples obtained at 480°C by in-situ synchrotron tomography at slow cooling rates of 1 K/min, 9 K/min and 30 K/min. The visualized slices presented in Fig. 5.20 were extracted from the middle of the samples. The microstructure of all samples consists of coarse intermetallic phases displayed in dark color and finer eutectic Si phase appearing light grey. Eutectic Al phase is imaged in grey color. In the high-purity alloy, the eutectic Si phase at the cooling rates of 9 K/min and 30 K/min is finer than that in the sample cooled at 1 K/min. In the Sr modified sample the eutectic Si phase exhibits a mixture of coarse and fine morphology at cooling rates 1 K/min and 9 K/min, while at 30 K/min it is uniformly fine. This indicates that eutectic Si is completely modified only at a cooling rate of 30 K/min. In the commercial alloy, the morphology of the eutectic Si phase is coarse in all samples indicating their formation independent of cooling rate. In Sr-modified commercial samples, the eutectic Si phase is coarse at a cooling rate of 1 K/min, while at cooling rates 9 K/min and 30 K/min the eutectic Si phase exhibits a mixture of coarse and fine morphology, which indicates that the eutectic Si phase is only partly modified.

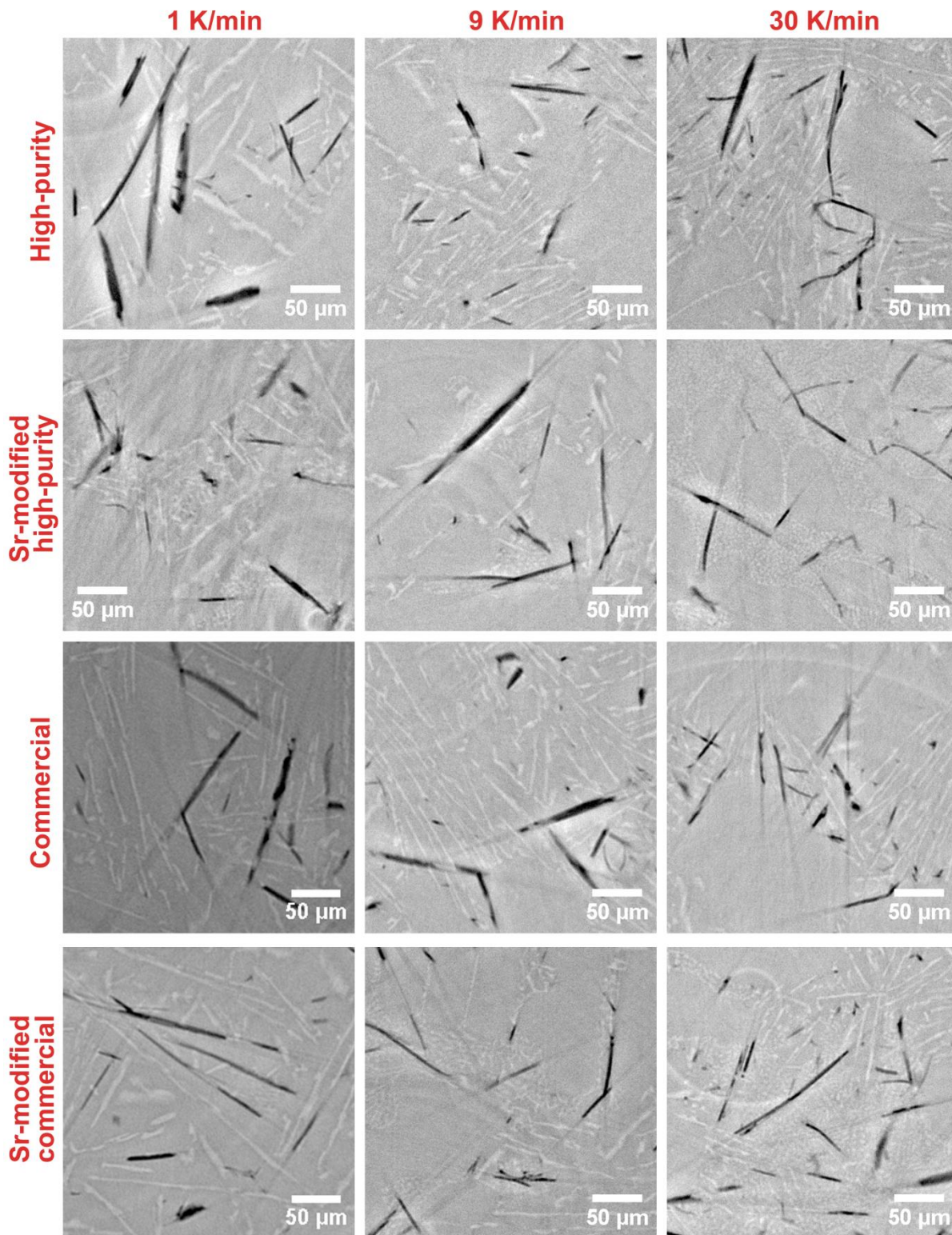


Fig. 5.20 Typical microstructure of fully solidified alloys obtained at 480 °C by in-situ synchrotron tomography: high-purity, commercial, unmodified, Sr-modified alloys as indicated at slow cooling rates of 1 K/min, 9 K/min, 30 K/min.

Intermetallic phases in all investigated alloys are not significantly distinct, only the size of intermetallics varies slightly. A three-dimensional visualization of intermetallic phases for all samples solidified at a cooling rate of 30 K/min is shown in Fig. 5.21. In all four alloys, the number density of intermetallic phases appears to be equal within the same investigated volume $\sim 200 \times 200 \times 280 \mu\text{m}^3$. Therefore, the studies were concentrated mainly on the nucleation and growth of intermetallic phases of only one alloy, namely the unmodified commercial alloy at cooling rate of 1K/min, which is representative for all other alloys.

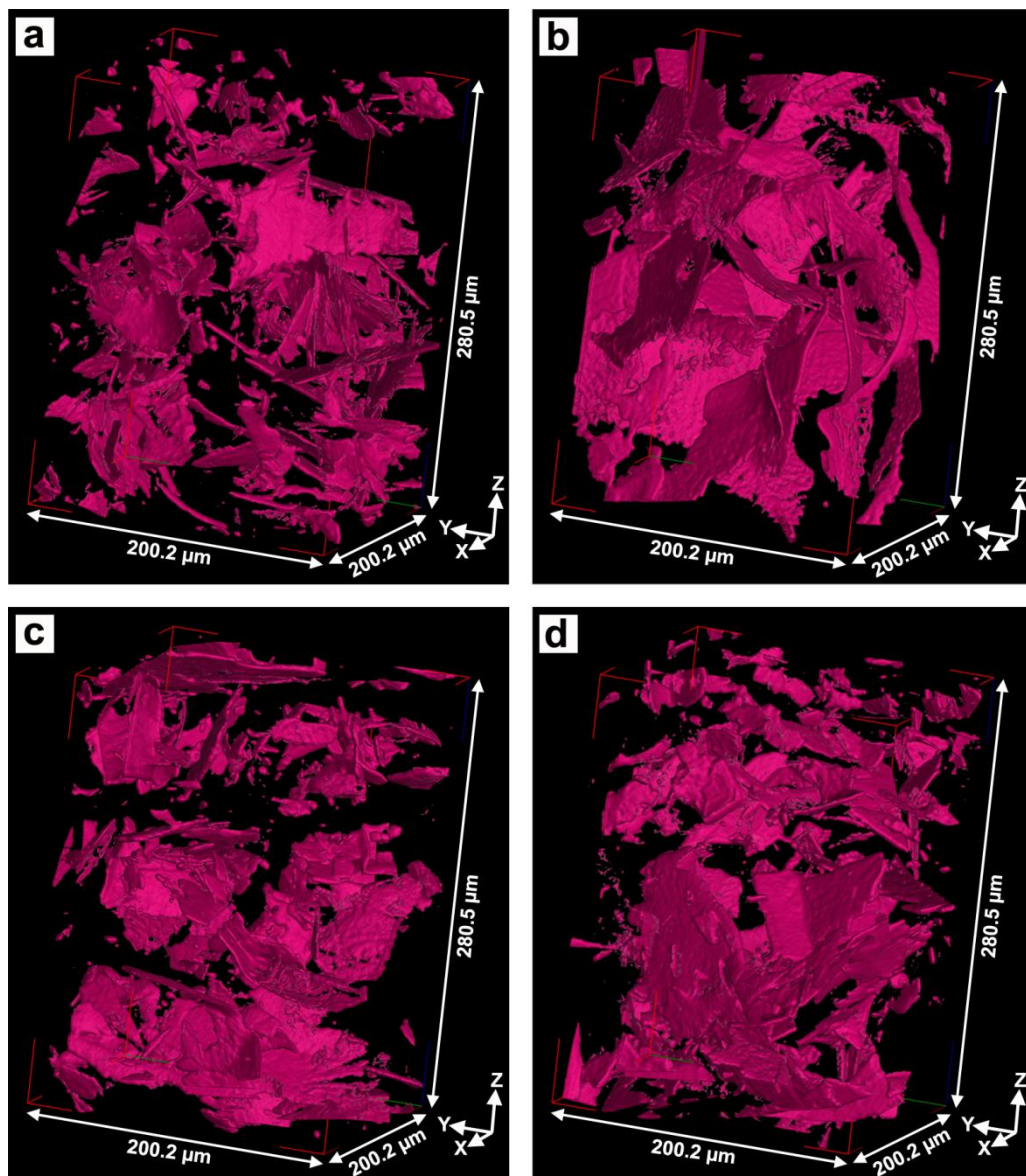


Fig. 5.21. Three-dimensional synchrotron tomographic visualization of the intermetallics (magenta) solidified at the cooling rate of 30 K/min in (a) the pure alloy; (b) the Sr modified pure alloy; (c) the commercial alloy and (d) the Sr modified commercial alloy.

5.3.1 Phase separation in the unmodified commercial alloy

The microstructural evolution during solidification was imaged by 3D synchrotron X-ray tomography. Special attention was paid to the formation of intermetallic phases. The solidification of the Al dendrites and eutectic Si was also studied, but to a smaller extent.

The cylindrical samples (1.5 mm diameter and 3.2 mm length) were heated to a temperature of 666° C in the furnace. Images of the microstructure by synchrotron radiation were obtained only from a part of the whole sample (1.5 mm diameter and about 1.8 mm length). The oxide skin surrounding the sample during melting supports the melt and keeps it stable.

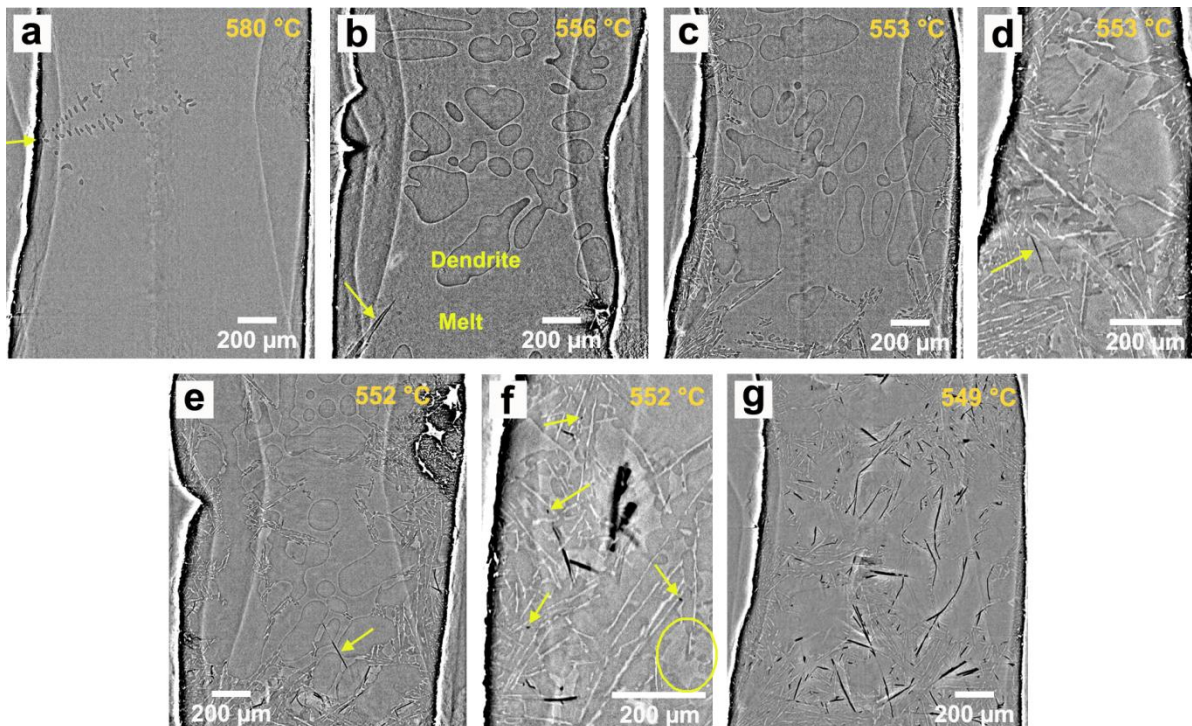


Fig. 5.22 2D vertical slices extracted from the reconstructed synchrotron tomography volume of the unmodified commercial alloy showing phases separation during solidification at different temperatures: (a) α -Al dendrites at 580°C; (b) Al-Si eutectic (as marked by arrow) at 556°C; (c) eutectic formed along the bottom and the oxide skin of the sample toward the center at 553°C; (d) δ phase at 553°C (image taken near the surface); (e) β phase at 552°C; (f) α or γ phase at 552°C and liquid "cell" marked by a circle; (g) state after approaching the end of phase separation at 549°C.

The sequence of events that happen during solidification from the melt is demonstrated in Fig. 5.22 by two-dimensional vertical slices extracted of the specimens at different solidification temperatures, from 580°C down to 549°C. The slices presented in Fig. 5.22 are

extracted from the middle of the sample as well as near the surface. It should be noted that the position of the extracted slices shown in the images is not the same in all the images.

The first observed solidification event is the appearance of the primary aluminum dendrites at ~ 580 °C as illustrated in Fig. 5.22a. Dendrites can be distinguished from the melt by a slightly darker contrast than the melt due to its lower X-ray attenuation. The dewdrop-like shapes in a line in Fig. 5.22a seem to grow radially from the oxide skin surface towards the center of the sample. A similar observation of dendrite growth in in-situ experiment has been reported previously in detail [39]. With decreasing temperature the aluminum dendrites grow to large sizes as can be seen in Fig. 5.22b. A second phenomenon is visible in the same image at ~ 556 °C, namely the formation of the eutectic Si phase (marked by arrow). The eutectic Si phase starts to grow at the surface of the sample bottom which is connected to a stick fixed on the rotation stage. At 553 °C (only 3 K lower) in the nearby area of the surface (oxide skin) many regions with eutectic Si and Al phases are visible (see Fig. 5.22c). The needle-like eutectic Si appears slightly brighter than the melt, while the eutectic Al surrounding the eutectic Si is slightly darker than the melt. The slice imaged in Fig. 5.22c has been extracted from the middle of the sample. The evidence that the eutectic phases first start to grow at the surface can be clearly seen in Fig. 5.22d in the slice extracted near the surface. A third event can be seen in this slice (Fig. 5.22d). The dark imaged needle-like phase (marked by an arrow) is the δ phase that forms in the eutectic network near/at the oxide skin at ~ 553 °C.

A fourth observed event is visible in Fig. 5.22e and 5.22f at ~ 552 °C, namely the formation of the β phase and α and γ phases. Figure 5.22e shows a slice extracted from the middle of the sample and Fig. 5.22f is situated near the surface. The β phase appears in the melt, is attached to the Al dendrite edge in the center of the sample and touches neither the eutectic Si nor the oxide skin. At this temperature some small globular intermetallic phases, appearing in dark contrast and with a size ranging between 7 and 10 μm , were found in the region of the eutectic Al-Si. Some of these intermetallics were found in the melt without being surrounded by the eutectic Si phase. These types of intermetallics have been identified as α and γ phases based on the features described above. The observations indicate that the growth of both phases is already completed at the current temperature (552° C). At this point it should be noted that the description of the phases and their surrounding areas is based on the observation of the three-dimensional images and not on the two dimensional slices shown in Fig. 5.22. Figure 5.22g shows the microstructure at ~ 548 °C where the volume fraction of the intermetallic phases has reached a maximum. No significant changes during in-situ tomographic observation take place below this temperature.

5 Results

In summary, the solidification of the phases was observed in a temperature range at which the dendrites start to grow, i.e. 580°C, down to a 549°C where the melt has completely solidified. The dendrites continue growing till ~550°C, whereas the solidification of eutectic Si has largely finished. Only a tiny part of them finally finish their growth at ~549°C.

It has been observed that only some dendrites touch the oxide skin of the sample during phase evolution. In-situ microstructure observation indicates a temperature gradient across the specimen, i.e. the bottom and the surface of the sample are colder than the center. Eutectic Si grows from the bottom to the top, along the oxide skin, and at the same time from the oxide skin towards the center of the sample. In this study, the eutectic phases do not nucleate at or nearby the surface of the dendrites, which is different to previous observations [40, 41] where it was observed that the eutectic phases began to form on the oxide surface.

As mentioned above, the δ phase was first found in the eutectic network near or at the oxide skin. The growth of the δ phase is always associated with the formation of eutectic phases [10]. Therefore the δ phase can be found both at the surface close to the oxide skin and in the center of the sample. Solidification of the δ phase was completed almost at the same time eutectic solidification terminated.

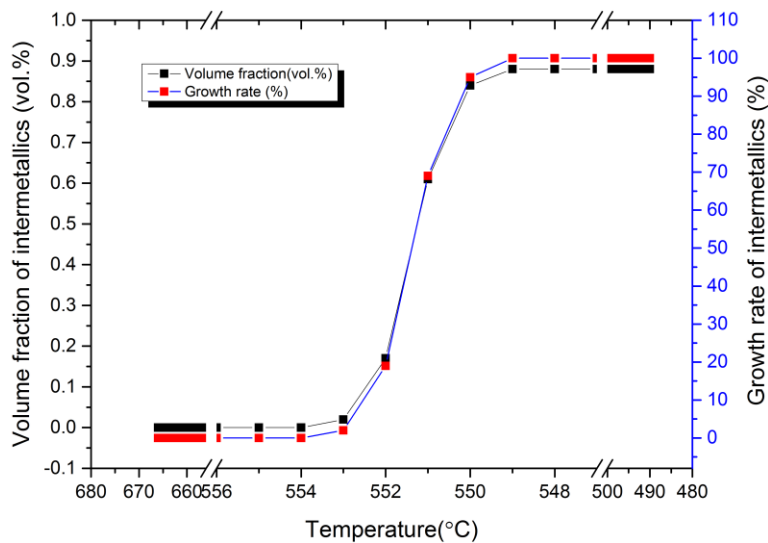


Fig. 5.23. The evolution and growth rate of volume fraction of intermetallics with decreasing temperature.

No β intermetallic has been observed to nucleate and grow on the oxide skin of the sample, which is different to observations reported previously [40, 42]. Based on the current observation in 3D the β phase appears to form in the gap between the neighboring tips of the dendrites arms and then grow into the melt until it impinges on the other dendrites. Both, the β phase as well as the dendrites nucleate at temperature well above the Al-Si eutectic. It

cannot be ruled out that the formation of both phases, β and dendrites, is weakly coupled, as has also been previously reported in Ref. [40, 42]. It has not been observed that the eutectic Si nucleates on neither β intermetallics nor on δ intermetallics, but eutectic Al was always found around the β or δ intermetallic phases.

Due to the limitation of spatial resolution, small-scaled α and γ phases can rarely be discerned in these measurements and the finer β and δ plates are also hard to observe. Therefore, the formation of α and γ phases will not be discussed in the following.

The volume fraction of all intermetallics reaches a maximum at ~ 549 °C and is 0.88 vol.% in the investigated unmodified commercial alloy. The volume fraction of the intermetallics and the growth rate as a function of temperature is shown in Fig. 5.23. It can be seen that the intermetallics form in a narrow temperature range. About 97.95 vol.% of the intermetallics nucleate and grow in the temperature range between ~ 553 °C and ~ 550 °C.

5.3.2 Evolution of β - and δ -intermetallics

The intermetallic β and δ phases are plates in 3D. The present sample contains a large number of both phases. The intermetallic phases are rarely alone; most of them are interconnected with each other and form branched formations. Figure 5.24 shows a series of reconstructed images of sample at 552°C, 551°C and 550°C of three independent groups of intermetallic phases. Only a part of the sample at 552°C, 551°C and 550°C with a few β and δ phases along with the oxide skin is presented from three different angles. The intermetallic phases can be classified into three groups, as indicated in Fig. 5.24b1: group 1 indicates the intermetallics with dark green color, which have been identified as δ phases. Group 2 indicates intermetallics in magenta color in the middle position, which have been identified as β phase. Group 3 indicates intermetallics within a group of plates with numerous colors, which are also identified as δ phases. The oxide skin is represented in gray. Only the branched plates in group 1 are observed to form at the oxide skin. Careful observation of the evolution of the intermetallic phases of group 1 indicates that the growth of the plates has already finished at ~ 552 °C and therefore, this group will not be further analyzed. However, the branched plates in groups 2 and 3 have just nucleated at ~ 552 °C and grow during the cooling of the melt. The plates of both groups finally impinge together at ~ 551 °C.

The branched plates of the β - or δ - phases were extracted from the reconstructed volume and analyzed separately at each temperature step.

- Evolution of the β intermetallics

A series of reconstructed images of the branched plates of the β intermetallic phases in magenta (named group 2 in Fig. 5.24b1) is presented in Fig. 5.25. The β phase extracted for

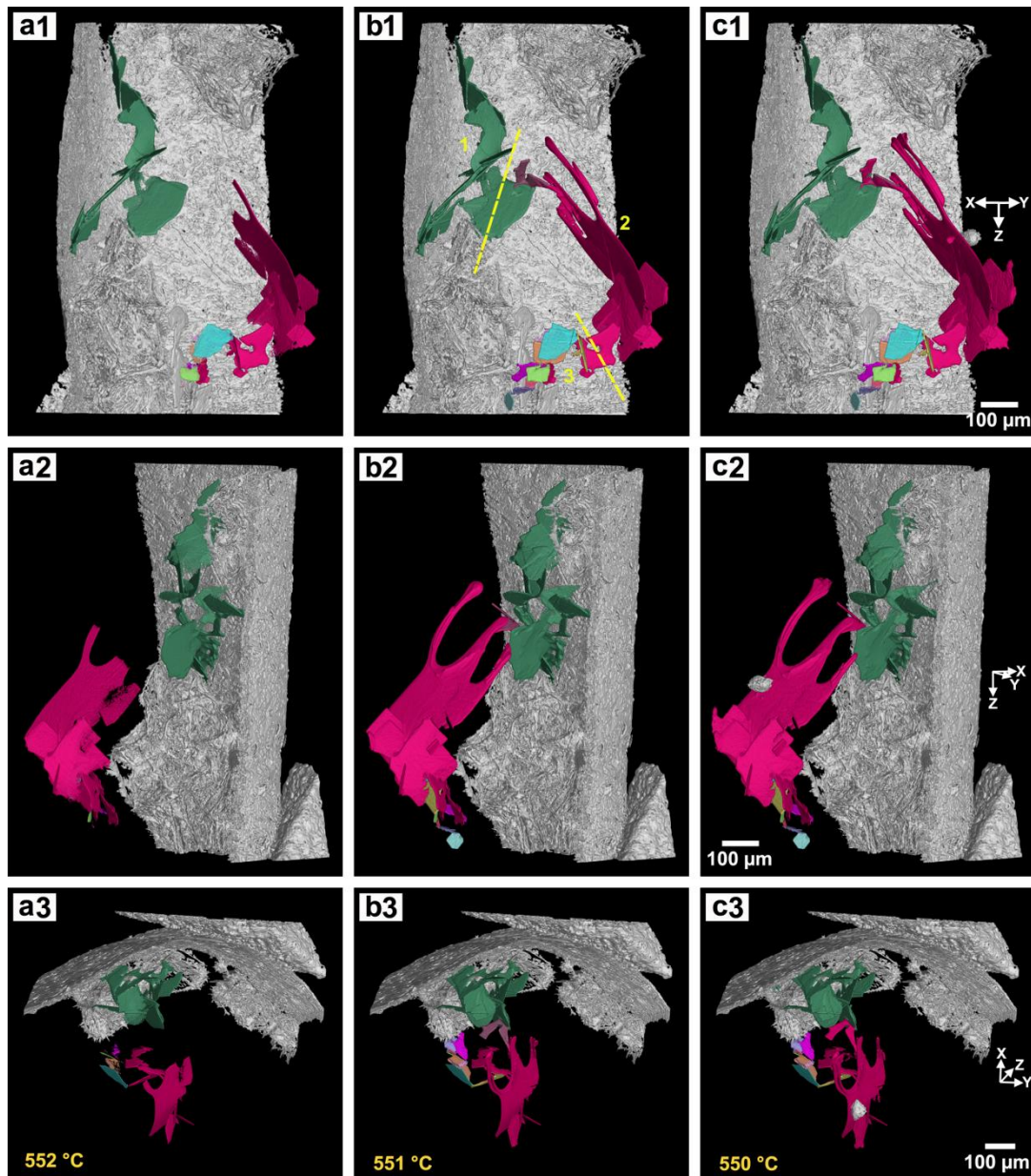


Fig. 5.24 Visualization of the evolution of the intermetallic β and δ phases and part of the corresponding oxide skin at (a1-a3) 552°C, (b1-b3) at 551°C and (c1-c3) at 550°C. Gray color represents the oxide skin, the other colors represent the different intermetallics (Al and Si transparent; β in magenta; δ in green and other colors).

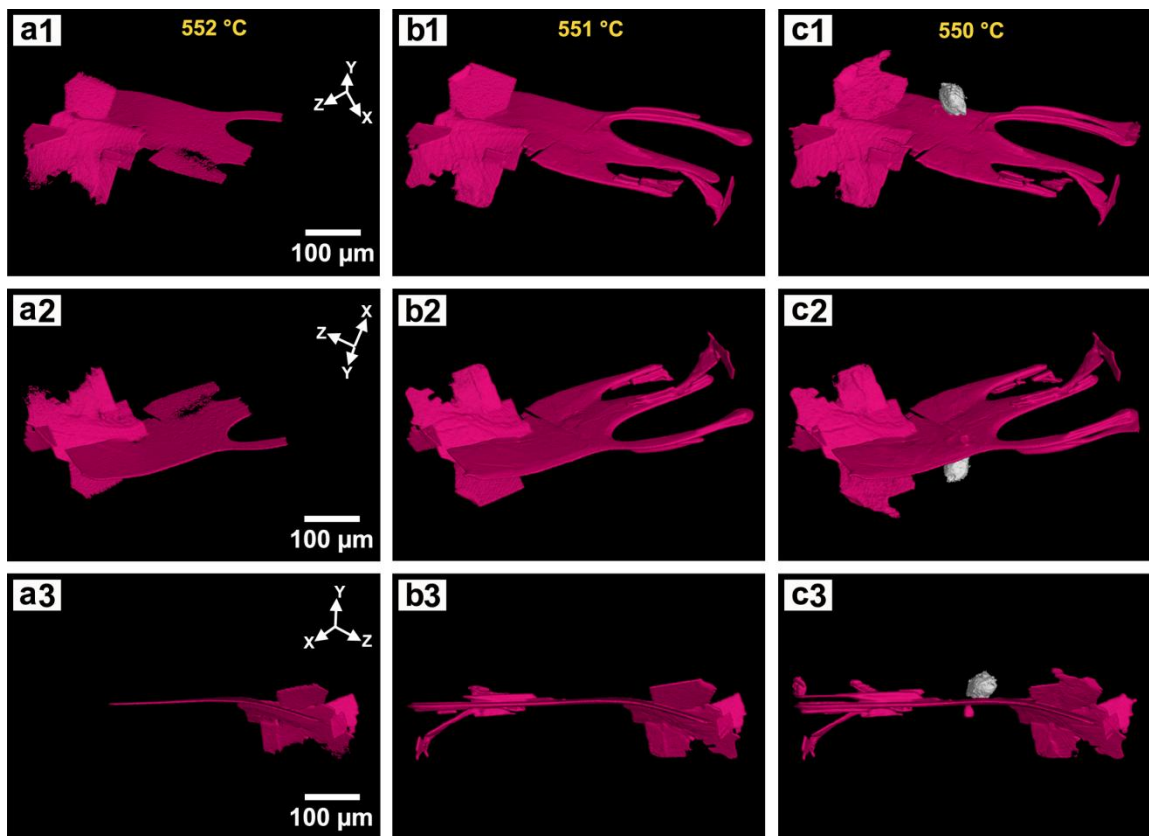


Fig. 5.25 Evolution of β phases demonstrated by 3-D images taken at 552°C, 551°C, 550°C (intermetallics in magenta; pore in gray).

characterization is visible as a needle in the 2D image in Fig. 5.22e and marked by an arrow. It is located between dendrites. However, the morphology of this phase in 3D from three different views as shown in Fig. 5.25a1-5.25a3 is much more complicated. The needle in 2D is indeed a network of branched plates in 3D. At the initial state the plate-like β phase nucleates and grows within the interdendritic liquid. With time the main plate grows, increases in size and impinges on the dendrites as can already be seen in Fig. 5.25a1-a2. The β plate wraps around two dendrite arms creating oval holes. The plate continues to grow but at a much lower velocity. Most likely the growth of the plate is blocked by the dendrite wall. Comparison of the images a3, b3 and c3 in Fig. 5.25 (left side of the image) reveals the formation of the new branched plates. The growth rate of the β phase has been evaluated by quantifying the plate length and the thickness during its evolution. The β phase evolves from 553°C to 550°C as seen in Fig. 5.25. The growth rate of the β intermetallics can be classified into three regimes: a rapid growth stage of the β plates occurs during the initial time step (553°C-552°C), where the recorded initial lateral growth rate is $\sim 5.8 \mu\text{m/s}$ and the measured

plate thickening rate is maximum $0.06 \mu\text{m/s}$. During the second time step (552°C - 551°C), the measured lateral growth rate is $\sim 2.68 \mu\text{m/s}$, and the measured plate thickening rate is $\sim 0.06 \mu\text{m/s}$. During the third time step (551°C - 550°C), the measured lateral growth rate is $\sim 1.72 \mu\text{m/s}$. The maximum recorded lateral growth rate in the present work is much lower than that reported in [40, 42]. The reason for this is probably that the supposed initial step in this work was recorded too late. The large size of the branched plates in Fig. 5.25 is an evidence for that. The lateral growth rate is always faster than the thickening rate, which is in agreement with previous observations [40, 99].

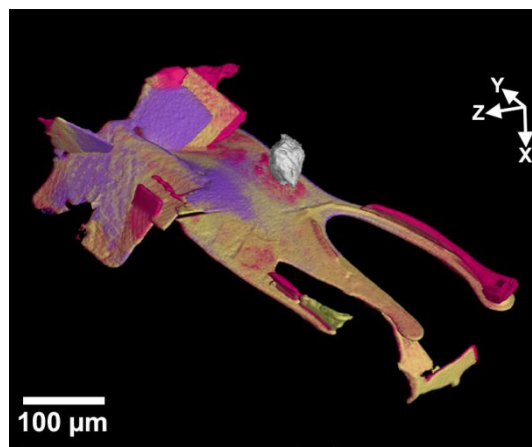


Fig. 5.26 Evolution of β phases shown as overlay of Fig. 5.25a1, b1, c1 in different colors: 552°C in purple, 551°C in yellow, 550°C in magenta.

At $\sim 550^\circ\text{C}$ (c1-c3), a spherical pore imaged in gray with a diameter of $\sim 53 \mu\text{m}$ is created on the surface of β plate.

Evolution of the branched β plates (552°C in purple, 551°C in yellow, 550°C in magenta) shown in Fig. 5.26 demonstrates growth of β plates at different stages.

- Evolution of the δ -intermetallics

The evolution of the δ intermetallic phases is demonstrated on group 3 marked in Fig. 5.24b1 and extracted in Fig. 5.27. As mentioned above, the morphology of the δ phase in 2D is needle-like and plate-like in 3D. The growth of the δ phases is very rapid: they nucleate at $\sim 552^\circ\text{C}$ and finish already at 551°C . Branched plates are formed within a very narrow time range. The branched δ plates are located in one or two channels between two or three eutectic Al-Si areas. As mentioned above, the formation of the δ phase is coupled with the

nucleation and growth of the eutectic Al-Si phases. The δ phases shown in Fig. 5.27 are much smaller than the β phases. It has to be noted that the environment in which the δ and β phases are formed is different, and this difference affects the size of the phases.

The formation of the δ phase can be explained as follows. The dendrites and the eutectic Al-Si grow during solidification and roughly separate the whole melt into many small areas which can be called small droplets or cells (see Fig. 5.22f). The word "cell" is defined here as small melt areas surrounded by eutectic Al-Si. Inside this irregularly shaped cell encircled by solidified phases, the δ phase nucleates and grows towards the outer layer of the existing eutectic Al-Si areas that have solidified before. The growth of the δ phase is finally blocked by the newly formed eutectic Al-Si phases. It has been observed that the δ phase can also nucleate and grow at the surface of pores and oxides in the cell, following the same mechanism. Growth and interaction of the δ intermetallics rapidly evolve in the lateral direction.

Since the δ plates only evolve from 553°C-551°C as seen in Fig. 5.27, their growth rate can be classified into two periods. At each time step, rapid growth spurts of the δ plates happen at the initial time step (553°C-552°C). The maximum recorded initial lateral growth rate is $\sim 2.35 \mu\text{m/s}$ and the average initial lateral growth rate is $\sim 1.22 \mu\text{m/s}$. The maximum measured plate thickening rate is $0.1 \mu\text{m/s}$ and the average thickening rate is $\sim 0.07 \mu\text{m/sec}$. At the second time step (552°C-551°C), the maximum measured lateral growth rate is $\sim 0.95 \mu\text{m/s}$ and the average lateral growth rate is $\sim 0.33 \mu\text{m/s}$. The measured maximum plate thickening rate is $\sim 0.05 \mu\text{m/s}$ and the average plate thickening rate is $\sim 0.025 \mu\text{m/s}$. These growth rates are all in good agreement with previous observations [40, 42].

The formation of imprints such as depressions on the δ plates can be explained when the growth of the thickness of the δ phases follows the surface of the already existing eutectic Si.

With the continuous solidification of the cell towards the enclosed melt of the cell, new δ phases can nucleate and grow on the newly solidified eutectic Al-Si and impinge with the previously formed δ phase in this cell. This process, during which several branches of δ phases are produced, repeats itself until the whole cell has fully solidified. It is worth noting that the nucleation and formation of δ and β plates in the same cell is possible if the solidification of dendrites and eutectic Al-Si are both involved in the cell formation.

The existing δ phase also influences the melt environment, the solidification areas and the solidification process in such a way that later formed δ plates impinge mainly on earlier formed δ plates or that simultaneously formed δ plates impinge on each other. During that

5 Results

period simple and complex branching can be generated as shown in Fig. 5.27-5.29, if there are no newly formed Al-Si eutectic blocks. Formation of curved, bent or fractured δ plates is mainly determined by already existing and newly formed Al-Si eutectic.

Plates branch at various angles, i.e. high, medium and low. The angles greatly depend on the initial direction of nucleation and growth with the cell solidifying from the outside to the inside. The eutectic Al-Si always surrounds the growing branch both at the branching point and on the two sides of plates, but branching occurrence and plate orientation do not fully depend on physical obstructions, unlike previously proposed [40, 42]. The orientation is mainly dictated by the liquid channel and the nucleation sites in the evolving cell. However, branching is mainly determined by the orientation of the δ plates involved and the blocks of solidifying eutectic Al-Si. Figure 5.29e shows the final impingement of three δ plates. Their growth was blocked by eutectic Si during solidification.

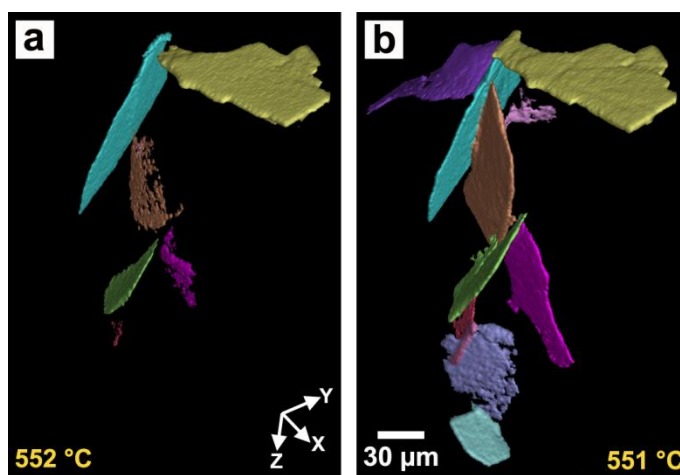


Fig. 5.27 Evolution of δ -intermetallics extracted from Fig. 5.24 (group 3). (Each color corresponds to an individually nucleated plate)

The situation in Fig. 5.29e has formerly wrongly been interpreted as a new δ plate nucleating on an existing δ plate [40, 42]. This has happened mainly because of the rapid nucleation and the impingement of the intermetallics, which sometimes exceed the 3D image boundaries and the capture interval. The complexity will be explained using the example of Fig. 5.29e. The presence of some very thin δ plates in the original 2D images suggests that all three plates nucleate independently and grow. However, the plate located in the middle of Fig. 5.29e (light purple) nucleates separately on the eutectic Si phase with two thin plates. These two thin plates then grow together and finally impinge with the light-magenta plates on the left-hand side. After impingement the middle plate (light purple) still grows slightly and at

the same time the light-cyan plate on the right-hand side nucleates on the eutectic Al phase and further impinges on the side of the middle plate.

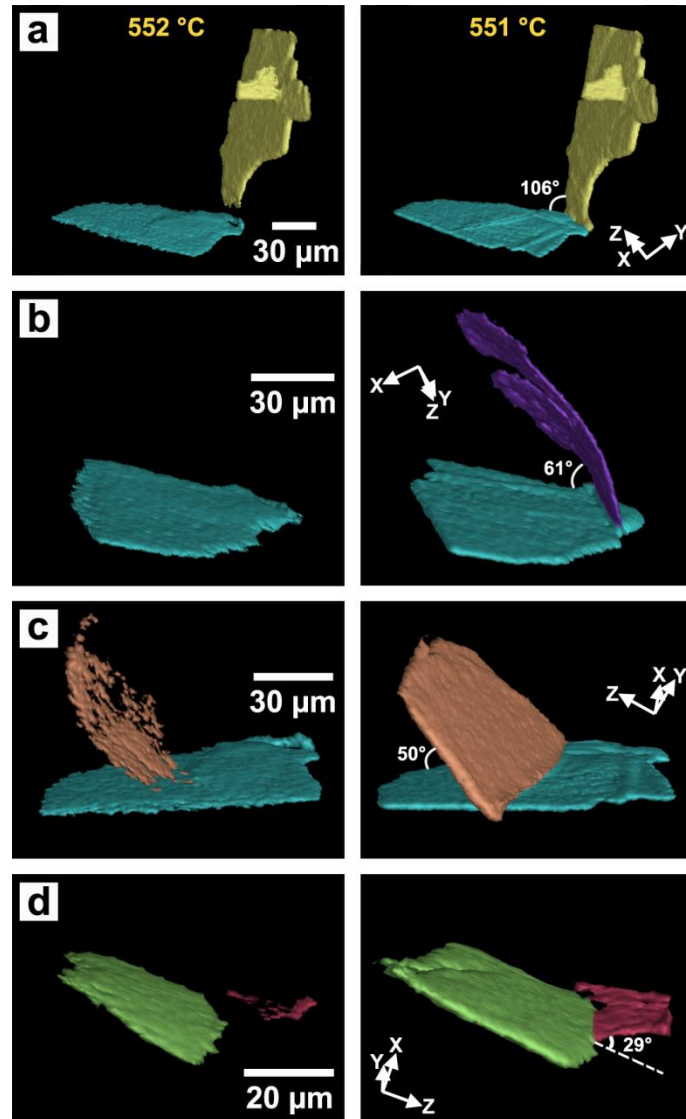


Fig. 5.28 Visualization of growth and interaction of single δ -intermetallics (extracted from Fig. 5.27; each color corresponds to a single formed plate).

It has also been observed in the original 2D images that the upper plates in Fig. 5.29a initially form as one highly curved plate. The orange and the purple-pink plates in Fig. 5.29a are indeed the same curved plate. Some of the light magenta plates are not visible in 3D. During growth the middle part impinges on the existing blue plate. Because of the impingement and the need of the plates for growing straight, the original curved plate has grown into three parts: The middle part (light magenta) grows parallel to the blue plate, whereas the two side parts (orange and light magenta) form an angle with the middle part

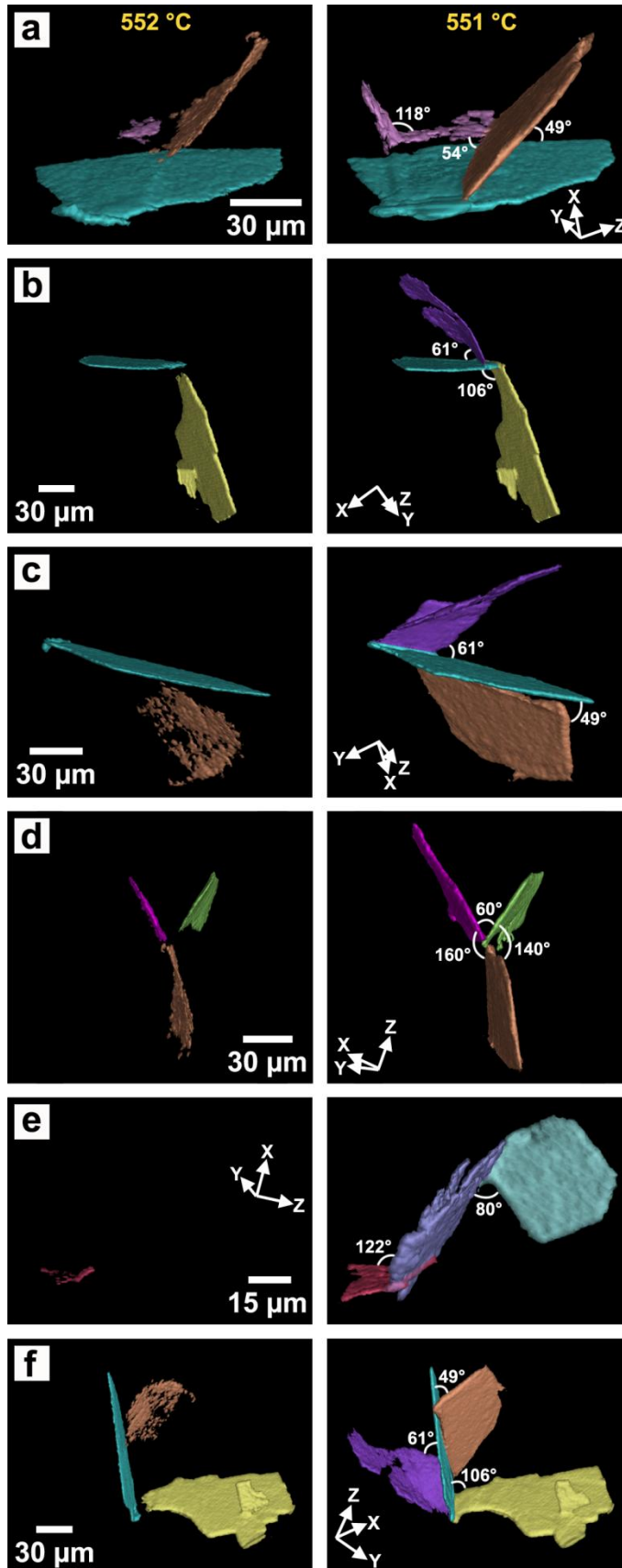


Fig. 5.29 Complex growth and interaction of single δ -intermetallics (extracted from Fig. 5.27; each color corresponds to a single formed plate)

and still grow a little. No eutectic Al-Si is involved during this straightening process. According to the current observations, no new δ phase directly nucleates on the existing δ phases and no eutectic Al-Si phase nucleate directly on the δ phases.

6. Discussion

Based on the results presented in Chapter 5 and using the basics explained in Chapter 2, the understanding of the microstructure in Al-10Si-0.3Fe -based alloys was further developed. In particular, the influence of impurities, of Sr additions and of cooling rates of the melt on the nucleation and growth of intermetallic phases during solidification has been described and discussed in detail.

6.1 In-situ synchrotron tomography / slow cooling

6.1.1 Effect of slow solidification on microstructure

The difference between the microstructure of the casting alloys shown in Fig. 5.2 and the microstructure produced during solidification at slow cooling rates (1 K/min, 9 K/min and 30 K/min) of all investigated alloys is shown in Fig. 5.20 and is quite obvious. At all slow cooling rates all samples exhibit coarse intermetallic phases (dark). The eutectic Si phase (light grey), solidified at the cooling rate of 1 K/min, in the high purity, the commercial and the Sr modified commercial alloys is shown in Fig. 5.20. It is coarse and comparable to that observed in the commercial alloy shown in Fig. 5.2c. In addition, the modification of the eutectic Si phase by Sr is totally absent in the commercial alloy, and only a partial modification is visible in the high purity alloy. The mixed structure of the eutectic Si phase, consisting of both plates and fibrous elements, indicates the low Sr amount in the alloy, as has been reported in Ref. [19]. Indeed, the level of Sr in the mentioned study was measured to be 62 ppm [19], whereas a well modified structure of eutectic Si can be achieved at Sr levels in the range of 80 - 120 ppm [100]. The loss of Sr in the in-situ investigated alloys can be due to the low cooling rate. At cooling rates of 1 K/min, 9 K/min and 30 K/min the melt was obviously kept at high temperatures for too long. The reduction of Sr from 62 ppm to 1 ppm was measured in the hypoeutectic Al-Si alloy after a 120 min melt holding time [19]. The reason for the Sr loss in the alloys is its evaporation during long melt holding times and due to its oxidation, as has been reported previously [101]. During solidification the Sr can evaporate up to the melt surface of the casting container, thus forming SrO with the oxygen

6 Discussion

at the vicinity of the melt surface [101]. Unfortunately, there are no systematic measurements in the literature about the loss rate of Sr during the different holding times. However, in order to provide an estimation of the remaining Sr amount in the present study during solidification at slow cooling, the data from Ref. [19] was used. The Sr oxidation rate in the melt can be expressed by the kinetic equation (1), as has been reported in Ref. [101]:

$$\frac{dc}{dt} = -kcn \quad (1)$$

where c is the Sr concentration in the melt at the t ; k is the reaction rate constant; n is the order of reaction. When “ kn ” is set as “ m ”, in which m is still constant, then equation (1) becomes:

$$\frac{dc}{dt} = -mc \quad (2)$$

When $t=0$, c_0 is the initial concentration of Sr, and we can obtain equation (3):

$$\ln \frac{c_0}{c} = mt \quad (3)$$

According to equation (3), the reaction rate constant of Sr can be calculated for different holding conditions. Based on the data from Ref. [19] (in which the alloys' compositions are similar to the current alloys), i.e. the reduction of Sr from its initial concentration of 100 ppm down to 62 ppm after a melt holding time of 5 min at the 720°C, the constant m can be calculated and used for estimation of the remaining Sr at different cooling rates of 1 K/min, 9 K/min and 30 K/min.

The high temperature state must thus be kept as short as possible. According to Ref. [19] the Sr modification time will be as follows: the cooling time from 720°C to 540°C, at a cooling rate of 390 K/min, corresponds to 0.46 min. Together with the 5 min holding time it equals to 5.46 min, which was rounded to 6 min for simplification. The 62 ppm of Sr after 5 min holding time [19] were measured by inductively coupled plasma-atomic emission spectroscopy (ICP-AES). By introducing an initial composition of Sr $c_0 = 100$ ppm and $c_l = 62$ ppm after ~ 6 min, the constant m in the equation (3) is calculated to be $m = 0.08$. First we checked the value of the remaining Sr, which is < 1 ppm after 121 min (whole cooling time), measured by ICP-AES, as reported in Ref. [19]. The remaining concentration of Sr was calculated to be $c_l = 0.95$ ppm, which is less than 1 ppm and in good agreement with the analysis in Ref. [19].

During the in-situ experiments the samples in the current work were heated to 666°C and cooled down to 540°C (fully solidified state). The holding time of 5 min at the highest temperature was kept constant for all samples in order to obtain a homogeneous alloy.

For the current study and with an initial value of 200 ppm Sr, the remaining Sr at different cooling rates is calculated to be: $c_1 = 0.006$ ppm at 1K/min (131 min), $c_2 = 44$ ppm at 9K/min (19 min) and $c_3 = 98$ ppm at 30K/min (9 min). The calculated amount of remaining Sr is also listed in Table 6.1.

Table 6.1 Some parameters describing the Sr amount during solidification.

cooling rate (K/min)	calculated solidification initial-end temperature / °C	holding time /min	whole solidification time /min	Remaining Sr amount /ppm
390	720-540	5	~ 6	62 [19] (measured)
390	720-540	120	~ 121	< 1 [19] (measured)
1	666-540	5	131	< 1 (calculated)
9	666-540	5	19	~ 44 (calculated)
30	666-540	5	~ 9	~ 98 (calculated)

As discussed above the Sr amount of 44 ppm at 9 K/min cooling rate is not enough to modify the eutectic Si phase completely [100], which is in good agreement with the microstructure shown in Fig 5.20 where the mixed structure of eutectic Si plates and fibres is observed in both the modified high purity and the modified commercial alloy.

Contrary to expectations, a mixed structure of the eutectic Si phase is present in the modified commercial sample even at a cooling rate of 30 K/min, even though the calculated value of Sr (98 ppm) should be enough for modification according to [100]. The modified high purity sample, however, shows complete modification of the eutectic Si. These results indicate that the calculated Sr content as listed in Table 6.1 is probably not accurate enough, which is due to the complex experimental conditions. However, it is important anyway to estimate the Sr value in order to explain the microstructure images observed by synchrotron tomography. The comparison of the microstructure of both the Sr-modified high-purity and the

commercial alloys at all cooling rates indicates that the modification of the eutectic Si in the commercial alloys is less pronounced than in the high-purity alloys. This is obvious when comparing the microstructure observed in Fig. 5.20, especially at 1 K/min and 30 K/min cooling rate. The modification of the eutectic Si phase in the commercial alloy is completely absent at 1 K/min cooling rate which is expected according to the estimated value of Sr < 1 ppm. In contrast, the eutectic Si in the high-purity alloy is partially modified. At the cooling rate of 30 K/min only a mixed structure of eutectic Si has been observed in the commercial alloy while the high-purity alloy exhibits a complete modification of the eutectic Si phase at the same cooling rate. Indeed, the given Sr value for modification, i.e. in the range of 80 - 120 ppm in Ref. [100], is a range of about 40 ppm and not a constant value, which can probably vary from one alloy to another depending on its composition. The conclusion based on the results of the present work is that the impurities in the commercial alloys induce evaporation of Sr.

The Fe-rich intermetallic phases shown in Fig 5.20 exhibit a similar coarse plate morphology in all investigated alloys. They are not significantly distinct and differ only slightly by their size. This observation indicates that the intermetallics follow a similar formation mechanism at slow cooling rates (1 K/min, 9 K/min, 30 K/min), regardless of Sr addition and impurities in the alloys.

The Fe-rich intermetallics β and δ in the in-situ investigated samples can be identified easily because of their large sizes. In contrast, the small-sized Fe-rich intermetallics α and γ are difficult to identify here due to the limited spatial resolution of synchrotron tomography, which is in the range of 1 μm . However, at some locations of the tomograms, Fe-rich phases of other morphologies than plates have been observed, and they are believed to correspond to these smaller-sized types of precipitates. Since the average size of the α and the γ phase is beyond the current resolution limit for in-situ tomography, only β and δ phases will be discussed in the following sections.

6.1.2 Nucleation and growth of the Fe-rich intermetallic β phase

A few words must be said about the sequence of the solidified phases in the alloys. As mentioned in section 5.3 the first solidified phase at 580°C are primary α -Al dendrites, which appear slightly darker than the surrounding melt due to their lower X-ray attenuation. They start to nucleate near the oxide skin surface and grow radially to the center of the sample as can be seen in Fig. 5.22a. As the temperature decreases ($T = 556^\circ\text{C}$) coarsening of

the α -Al dendrites proceeds, as can be seen in Fig. 5.22b. This result is not new; in the previous studies [39-42] α -Al dendrites being the first solidifying phase have also been reported. The second solidification event is the eutectic Si phase, which has also been observed near the oxide skin surface at the bottom of the sample. Thus, both phases have been observed to nucleate near the surface. This indicates the presence of a thermal gradient across the sample since the surface is colder than the center. Similar observations of in-situ solidification experiments have also been reported in Ref's [40, 42].

The next solidification event is the formation of the β phase. In this work, only a few apparently independently nucleating β plates were observed in the volume of $\sim 1.5 \text{ mm}^3$. Terzi et al. [42] have suggested that the low nucleation of the β phase is attributed to the slower cooling rate (1.4 K/min), since the only difference between their work and previous research (20 K/min) [102] was the cooling rate. However, based on the results in the present work, it can be suggested that the low number of nucleating β phase is not only due to the lower cooling rate (1 K/min), which decelerates heterogeneous nucleation, but probably also due to the low Fe amount and thereby a low ratio of Fe to Si, since the formation of the β phase is strongly linked to the Fe and Si content [29].

The current observations indicate that the β plate shown in Fig. 5.22e and Fig. 5.24 forms in the melt and is attached to the dendrite edge in the center of the sample without touching neither the eutectic nor the oxide surface. No independent β intermetallics have been observed to nucleate and grow on the oxide surface of the sample. This observation is different from previous reports [42] with which we share a similar experimental environment at the ESRF in Grenoble, even though the alloy compositions (0.8 wt.% Fe in Ref. [42] compared to only 0.3 wt.% Fe in the current work) between these two experiments are different. In the result of Terzi et al. [42], all four observed β intermetallics initiate on or near the oxide surface, suggesting that aluminium oxide is an active nucleant for β intermetallics, which is in good agreement with reports [63, 68]. Puncreobutr et al. [40] have also observed the nucleation of β plates on the oxide surface and oxide skin of pores using synchrotron X-ray tomography. A nucleation of the β phase on the externally wetted surfaces of the oxide films (called double oxide films or bi-films), which are entrained into the melts during casting, has been reported by Cao et al. [62]. The typical center-line cracks, commonly observed in their work, have not been found in the current study. Furthermore, it is still under discussion whether γ - Al_2O_3 or α - Al_2O_3 (skin surface oxide) is proposed as a potential nucleant for the β phase formation [5, 62, 63, 67, 68].

6 Discussion

As can be seen in Fig. 5.22e the observed β plate initiates from the gap between two arms of the neighboring dendrites and then intrudes towards the outer sides of the melt until it impinges on the other dendrites. The schematic 2D illustration of the 3D formation of the β intermetallics is presented in Fig. 6.1, which is basically derived from the 2D original sample section.

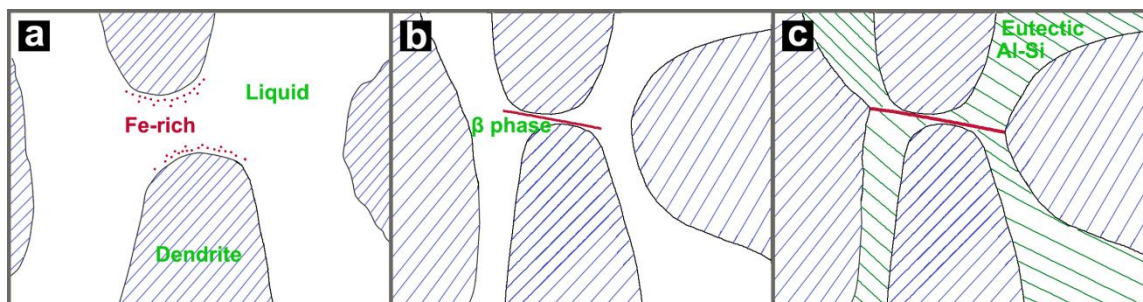


Fig. 6.1 Schematic 2D illustration of the in-situ 3D formation of the β intermetallics in the unmodified commercial alloy.

As illustrated in Fig. 6.1, during solidification the front of the growing dendrites at the solid-liquid interfaces is highly enriched in Fe, due to the dendrites' rejection of Fe. The typical β intermetallics nucleate at the front interfaces of the growing dendrites, and further grow tangentially in the narrow space that the dendrites arms are surrounded by until they impinge on obstacles such as dendrites, other existing/growing intermetallics, or even the eutectic. This narrow space among the dendrites contains a supersaturated solution of Fe and the other impurities, which is a prerequisite for the formation of β intermetallics. The low concentration of Fe in the current alloys (0.3 wt.%) and thereby the low amount of Fe in the supersaturated solution during the early stages of solidification is one of the reasons for the low number of β phases forming in the current alloy.

Since the number of β phases in the present experiment is low, it cannot be ruled out that β intermetallics can form in other regions, as mentioned in Ref. [103], which suggests that the β intermetallics form between adjacent interdendritic arms.

Kim et al. [69] have suggested that the β phase and the α -Al dendrite nucleate and grow together in the mode of a eutectic couple, based on their in-situ radiography observations. The observation that β phases tend to be parallel to the nearby arms of the α -Al dendrites

also points towards the fact that the β phase nucleates because of the supersaturation in solute atoms in the melt.

Recently, Puncreobutr et al. [40] quantitatively investigated the morphological texture of the β intermetallics nucleating on/near the α -Al dendrites, indicating that a majority of β plates grows parallel to the secondary dendrite arms, which supports our observations.

Unlike the results of Terzi et al. [42], who claimed that the β intermetallics only form on or near the oxide surface of sample, Puncreobutr et al. [40] suggested that the β intermetallics can nucleate 1) on the oxide surface; 2) on the α -Al dendrites; 3) by self-nucleation; 4) on the oxide skin of the pores. Furthermore, it was proposed that aluminium phosphide is a potential nucleation site for β intermetallics [65, 66]. Since the aluminium phosphide nuclei are beyond the resolution limit of synchrotron tomography, their presence in the “supersaturated solution” cannot be detected in the present study. According to Puncreobutr et al. [40] the nucleation on or near the α -Al dendrites is the dominant mechanism (~66 % of the cases) for the formation of β intermetallics. The other β phases (~34 %) nucleate at the oxides in the specimen or at pore surfaces via branching or via the presence of other active nucleation sites such as aluminium phosphide. Although the current study could not confirm all of the above mechanisms due to the limited number of β intermetallics formed in the used alloys, there is no doubt that there is more than one nucleation site for the formation of β intermetallics based on the knowledge of heterogeneous nucleation as described in Ref. [104].

The initially rapid growth after nucleation of the β phase in the lateral direction is followed by a slow growth and a slow thickening rate during later stages of solidification. This observation is confirmed by previous in-situ 3D synchrotron X-ray tomography investigations [40, 42, 103]. However, in the present study, the average growth velocity of the β phase at the beginning of solidification was found to be $\sim 5.8 \mu\text{m/s}$, which is much lower than the one measured in Ref. [42], i.e. $12.5 \mu\text{m/s}$ at 1.4°C/min cooling rate or $34 \mu\text{m/s}$ at 20°C/min cooling rate; and $30 \mu\text{m/s}$ at 3°C/min cooling rate as reported in Ref. [40]. The large difference in these values to those in the present study is probably due to the different alloy compositions and the late start of measurement of the growth kinetics in the present study. The initial tremendous burst of speed is mainly due to the release of accumulated growth energy based on the undercooling as has been confirmed in Ref. [40]. However, the sufficient solute diffusion at the growth front of the β plate is also considered an important factor for influencing the growth velocity and the growth behavior of the β plates [40, 42]. The growth velocity at the end of solidification in the present study, ~ 1.7

$\mu\text{m/s}$, is comparable to that measured in [40, 42]. The decrease of the growth velocity can be explained by the solute depletion and the blocking caused by surrounding $\alpha\text{-Al}$ dendrites, which is in agreement with the results observed in Ref. [40, 42]. Indeed, the β plate located in the center of the sample (see Fig. 5.24) was found to grow from the bottom to the upper part of the sample, further growing in an oval shaped frame around the dendrite arms. Based on the images in Fig. 5.25 it is evident that the growth of the β plate is restricted by the constrained space, which in this case are the dendrite arms.

Terzi et al. [42] suggested that the $\alpha\text{-Al}$ and the β phase grow with an irregular eutectic growth in a coupled or an uncoupled way. Puncreobutr et al. [40] suggested that the $\alpha\text{-Al}$ and the β phase exhibit weakly coupled growth. The observations in the present study lead to the conclusion that $\alpha\text{-Al}$ and the β phase have indeed a weakly coupled growth since the Fe-rich plate-like intermetallic β phase has been found to nucleate inside the Fe-supersaturated melt near or between the $\alpha\text{-Al}$ dendrite arms. Based on the experimental observations it can be suggested that the nucleation of the β phase occurs mainly via a binary eutectic reaction, i.e. $L \rightarrow \alpha\text{-Al} + \beta\text{-Al}_5\text{FeSi}$. Similar in-situ observations have been reported on the alloy Al-7.5Si-3.5Cu-0.6Fe (wt.%), where nearly 90% of the total volume of the β phase forms via a binary eutectic reaction [40]. In contrast to this, Refs [28, 42, 102] claim that nucleation of the β phase forms via a ternary eutectic reaction, i.e. $L \rightarrow \alpha\text{-Al} + \text{Al-Si} + \beta\text{-Al}_5\text{FeSi}$. The latter observations are not supported by the present experiment, even though imprints of eutectic Si are visible on the β plate as shown in Fig. 5.25. The presence of these unique imprints of eutectic Si on the β plate can be explained as follows: as the growth of both phases ($\alpha\text{-Al}$ and $\beta\text{-Al}_5\text{FeSi}$) proceeds during further solidification, the eutectic Si start to nucleate and grow rapidly in such a way that the Si plates touch the β phase and leaves imprints.

The formation of β plates during eutectic solidification is believed to be responsible for sponge-like pores [28]. A detailed examination of the microstructure development vs. time in the present study revealed that the pores shown in Fig. 5.24 and Fig. 5.25 have been formed in the last stage of local solidification near the β plate. This pore is also surrounded by $\alpha\text{-Al}$ and eutectic Al-Si. Some mechanisms have been proposed in order to interpret the influence of the β plate on pore formation:

- 1) blockage of the interdendritic flow by the β plate [28, 33, 103, 105-108];
- 2) blockage of the hydrogen diffusion paths by the β plate [33, 105];
- 3) β plate acts as a nuclei [33, 103, 106];

4) growth behavior affected by the β plate and/or other phases [103, 105].

The interdendritic flow and the growth behavior being affected by the β plate has been directly observed by in-situ tomography [105]. It has also been observed [105] that the growth of a pore is physically constrained by several β intermetallics, primary dendrites and the Al-Si eutectic. It has been suggested [103, 105] that accelerated pore growth along the surface of a Fe-rich β plate is due to a lower interfacial energy of the intermetallics–gas interface than that of the gas-liquid or the gas- α -Al interfaces. The pore observed in the current study (Fig 5.24, and Fig 5.25) is located near the β plate. The pore grew very fast within less than 1°C and therefore its evolution or coarsening could not be followed. Based on the current results it is suggested that the growth of the pore is completed at already 550 °C due to the solidification of the surrounding phases. Preferential pore growth along the planar surfaces of the β phase has also been observed previously [105]. Puncreobutr et al. [105] suggested that the β phases do not nucleate the pore directly during solidification, but instead they block the interdendritic channels and reduce the permeability of hydrogen resulting in its local supersaturation.

Besides the β phase no other Fe-rich intermetallic phases have been found in the recently published in-situ experiments [39-42, 102]. In contrast to these, in the present work all Fe-rich intermetallic phases (α , β , δ and γ) are present, as has been supported by the subsequent examination of the in-situ samples by TEM investigations.

6.1.3 Nucleation and growth of the Fe-rich intermetallic δ phase

The second intermetallic phase formed in the alloys during solidification was found to be the δ phase. This was surprising, because formation of δ phase during solidification experiments has not yet been reported in in-situ experiment [40, 42]. This is probably because of their plate-like morphology, which is similar to that of the β phase, and thus they can easily be mistakenly identified as the β phase. Since both phases have a similar chemical composition it is hard to distinguish between them by SEM/EDX [18]. It has often been reported that the β phase can nucleate via binary and ternary eutectic reactions depending on the Fe content in the alloy [28]. The β phase via binary reaction has been observed in an as-cast alloy with 0.7 wt% Fe, the β phase via ternary reaction in one with 0.3 wt% Fe (which is the same amount as in the current study) [28]. Therefore, it seems likely that the δ phase has been misidentified as a ternary β phase in previous research, forming via eutectic reaction $L \rightarrow \alpha\text{-Al} + \text{Al-Si} + \beta\text{-Al}_5\text{FeSi}$ [76, 108]. In fact, the $\beta\text{-Al}_5\text{FeSi}$ phase should be $\delta\text{-Al}_4\text{FeSi}_2$, because the δ

6 Discussion

phase mainly forms as a secondary phase while the β phase forms independently as a primary phase. Wang et al. [102] observed the formation of a binary β phase at a cooling rate of 0.33°C/s (comparable to the present study, 1 K/s) but with $0.8\text{ wt.}\%$ Fe in the alloy. Based on the present results it can be suggested that the plate-like intermetallic δ phase nucleated via a quadruple eutectic reaction, i.e. $L \rightarrow \alpha\text{-Al} + \beta\text{ Al}_5\text{FeSi} + \text{Al-Si} + \delta\text{-Al}_4\text{FeSi}_2$.

The δ phase was usually found in Al-Si alloys with high Si content [5, 57, 98, 104] and including Sr additions [10, 19, 98]. It has been proposed [5, 57, 104] that δ is the dominant phase at high Si contents and high cooling rates while β is dominant at a high Fe content and low cooling rates. This conclusion is not supported by the present results because the δ phase has also been found to form at a high Si content and at low cooling rates.

The nucleation of the δ phase can be understood by a detailed examination of the areas between the eutectic Al-Si cells vs. time evolution. In-situ synchrotron tomography has been performed at the cooling rate of 1K/min . The low cooling rate is necessary to ensure that the microstructure does not evolve too fast during image acquisition, implying that each important evolution of the microstructure can be effectively recorded during each scanning step. 4D visualization allows for an insight into the morphology of the precipitates and their spatial arrangement during time. During solidification the δ phase nucleates from $\sim 553^\circ\text{C}$ to $\sim 551^\circ\text{C}$ while the eutectic Si evolves from $\sim 556^\circ\text{C}$ to $\sim 549^\circ\text{C}$. Each δ plate nucleates and

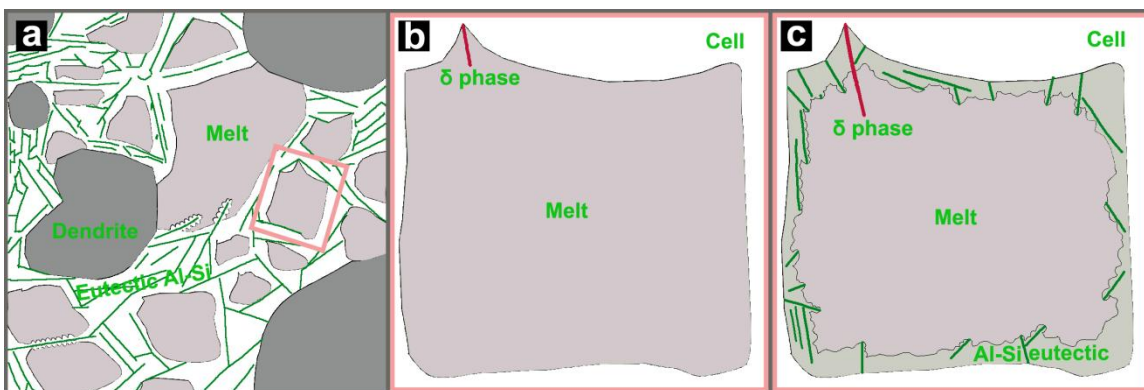


Fig. 6.2 Schematic representation of the formation mechanism of the δ intermetallics in the unmodified commercial Al-10Si-0.3Fe alloy: a) growing eutectic and dendrites roughly separate melt into many cells during solidification; b) in detailed insight into the region marked by a red box where δ intermetallics just initiates; c) growing of specified cell during solidification (melt in different colours indicates solidification proceed toward inner cell).

grows in a temperature range of $\sim 1^\circ\text{C}$, i.e. from 553°C - 552°C or 552°C - 551°C as can be seen in Fig. 5.27. It is apparent that the time range of δ phase formation is basically covered by the eutectic formation time range, and the time range of the eutectic formation has a longer time span than the formation of the δ phase. Thus, the formation of the δ intermetallics should be significantly influenced by the formation of the eutectic Al-Si.

The formation mechanism of the δ phase is presented schematically in Fig. 6.2. The melt areas surrounding the eutectic Al-Si cells and the α -Al dendrites are shown in Fig. 6.2a. One of the melt areas is extracted and examined in detail. The extracted area is surrounded by solidified eutectic Al-Si cell (see Fig 6.2b). During solidification of the eutectic Al-Si, the enclosed melt is enriched in Fe due to the rejection of Fe towards the solid-liquid interfaces. The δ phase nucleates on the supersaturation front pushed by the growth of the eutectic, i.e. in the places where Fe and other solutes are locally abundant in the eutectic (Fig. 6.2c).

The observed δ plate initiates at the eutectic Si, probably due to the enrichment in supersaturated Fe and other solutes or impurities that are potential nucleants. It should be noted that there might be more than one event initiated simultaneously at each growing cell wall. This schematic drawing in Fig. 6.2 only exhibits one event for each growing cell wall progressing towards the cell center for the sake of simplicity. The diameter of the cells surrounded by the eutectic can take any value but mainly ranges from some tens to a few hundreds of micrometers.

When the growth of the δ phase is completed, the surrounding solidifying melt has formed mainly eutectic Al. The average size of the plate-like δ phase is much lower than that of the β phase. This is because of the limited melt areas between the eutectic Al-Si phases. Nucleation and growth of the δ phase has already been described in detail in chapter 5.3. However, it should be noted that this phase has not been observed in the as-cast commercial alloy, but only in the Sr-modified commercial and high-purity alloys. The only difference in the production process of the cast samples and the in-situ samples of the commercial alloys is the cooling rate. This means that a lower cooling rate promotes formation of the δ phase. In order to be sure that the δ phase really exists in the solidified sample after the in-situ synchrotron tomography experiment, the sample has been investigated by SEM and TEM. Both the coarse β and the fine δ phase could be identified.

The δ plates observed by synchrotron tomography in this work nucleate not only on the eutectic (as shown in Fig. 6.2), but also on the surface of the pores and the aluminium oxide in the cell which is located around or containing these areas (not shown in Fig 6.2, but it

6 Discussion

follows a similar mechanism). These observations indicate that the δ phase follows the heterogeneous nucleation theory. It was previously proposed that the δ phase can nucleate on oxide bi-films [62]. Khalifa et al. [104] investigated a series of inclusions that might be a potential nucleation substrate, and they found that the δ phase can nucleate on extensive inclusions such as CaO, TiB₂ or α -Al₂O₃. There are three simultaneous necessary conditions for the nucleation of intermetallics [104]:

- 1) a certain solute concentration that corresponds to the composition of the phase in the melt;
- 2) the necessary nucleation temperature;
- 3) an appropriate nucleation substrate.

It has been suggested [104] that nucleation of the δ phase as a secondary phase is highly affected by the solute concentration, rather more than by the potency of the substrate. Furthermore, heterogeneous nucleation of a phase on a nucleant in a melt requires a certain amount of undercooling to activate the nucleation events if the nucleation sites are not potent enough [104]. Here, the role of substrates in the nucleation of the intermetallic phases is largely limited by the satisfaction of the solute concentration and the nucleation temperature requirements [104]. Keeping that in mind, the current nucleation events on the eutectic, the pores and the oxides can be understood. It is obvious that the eutectic is a potent nucleation substrate for the formation of the δ phase in this alloy. Pores and oxides are only second choices for nucleation since the vast majority of δ phase nucleation is observed on the eutectic, especially on eutectic Si.

As reported in the literature [40, 42] thin evolving β plates can undergo deformation, bending or fracture during growth, which is a result of physical interactions with contacting dendrites. The deformation of δ plates due to internal strains and contact with eutectic Al-Si and solidified α -Al dendrites has also been observed in the present study. A small movement of the outer oxide skin and of the dendrites can occur during shrinkage of the sample. This can locally change the growth orientation of the δ plate. A δ plate can straighten itself when a curved δ plate grows closer to an adjacent straight δ plate. Here as seen in Fig. 5.29a it probably happened because the curved δ plate was pinned by the eutectic Al-Si and the solidified α -Al dendrite.

β plates as well as δ plates can never be found alone; they are always branched. Branching and interaction of the β plates can be mainly classified into two types via an impingement mechanism and a nucleation mechanism (new β plates nucleate on existing β plates) [40]. In the present study, only one mechanism could be observed, namely growth process of the

impingement of the δ plates. Initially, δ plates nucleate and grow independently. Later during rapid lateral growth they collide as can be seen in Fig. 5.29. The nucleation of new δ plates on existing δ plates has never been observed in the current experiment.

6.2 Ex-situ observations of the microstructure in the as-cast alloys / fast cooling

The microstructure of high-purity and commercial-purity Al-10Si-0.3Fe-based casting alloys with and without Sr additions was compared and discussed in terms of the impurities' influence on the microstructure evolution using different microscopic (OM, SEM, TEM) and tomographic (FIB and synchrotron) techniques.

6.2.1 Effect of Sr on Al-10Si-0.3Fe-based alloy

The eutectic microstructure of the as-cast alloys shown in Fig. 5.1 indicates different evolution mechanisms during solidification. The typical eutectic Si of unmodified commercial alloys as shown in Fig. 5.1c is coarse with large space between the Si flakes. In comparison, the eutectic Si in the unmodified high-purity alloy (see Fig. 5.1a) is very fine, containing short Si flakes with little space between them. The modified eutectic Si of both alloys shown in Fig. 5.1b and 5.1d is the result of Sr additions, which implies the fibrous structure of the eutectic Si. Modification of eutectic Si by Sr was attributed to the high undercooling [110], observed from the typical cooling curves of similar investigated alloys [71] and shown in Fig. 2.9.

In contrast to the commercial alloy, the high-purity alloy without Sr shows a much higher undercooling which is comparable to that of both alloys with Sr addition. Mc Donald et al. [71] suggested that the undercooling is not directly linked to modification but to the growth of the eutectic grains. Indeed, the size of the eutectic grains (except in the unmodified commercial alloy) [71] is almost identical for the high-purity alloy with and without Sr and for the Sr-modified commercial alloy. Recent research with atom probe tomography and transmission electron microscopy [35, 36, 72, 73] clearly demonstrates that the modification of the eutectic Si is attributed to nanometer-sized Al-Si-Sr segregations located within the eutectic Si, and that it is not attributed to individual atoms absorbed at the eutectic Si growth interface [111]. The commercial alloy has a much higher density of eutectic grains, which are much smaller than in the Sr modified alloy [71]. The large number of eutectic grains in

6 Discussion

the commercial alloy is due to the major role of impurities which act as active nucleants in the eutectic solidification. However, Sr additions markedly decrease the nucleation of eutectic grains. The refined Al-Si eutectic can be explained by an increase of the growth rate and interface velocity of coupled Al and Si eutectic phases.

Since Sr-modification has an effect on the eutectic grains, a model has been proposed recently by Timpel et al. [10], explaining how intermetallic phases form in the eutectic grain in the Sr-modified Al-10Si-0.1Fe alloy, which indicates that the addition of Sr leads to an heterogeneous distribution of secondary intermetallic phases within the eutectic grains of the Al-Si alloys. The modified eutectic grains can be categorized into three regions:

- 1) well-modified central regions with fine fibers and free of intermetallics;
- 2) transition region, where the α phase precipitates in isolated pockets next to the pre-existing primary Al dendrites in the eutectic grain;
- 3) outer region, where the δ phase forms after a severe segregation of Fe in a Si-rich melt during a second interval of nucleation.

McDonald et al. [55] presented a similar grain cell structure, in which numerous β phases and isolated pores are observed only in the outer region (region 3). The development of the radial eutectic grain structure during solidification, which has been previously reported [10, 55], is not supported by the present study. Based on the current synchrotron tomography results it has been concluded that the flake-fibrous transition in the Si morphology at the cell boundaries mentioned in Ref. [10, 55] is probably due to different local orientations of the eutectic Si fibers within the neighbor cells.

Addition of Sr to the high-purity alloy does change the intermetallic types, sizes and density as well as their morphology. In general the growth mode of the eutectic Al-Si is changed from the uncoupled mode in the unmodified to the coupled mode in the Sr modified alloys. The coupled and identical growth rate of eutectic Si and Al results in the creation of a smooth solid-liquid interface, which is responsible for the absence of isolated pockets, in which usually the α phase or the γ phase precipitate. Moreover, the isolated pockets are very small and therefore the size and the number density of the α or the γ phase is strongly reduced. This is supported by the results in Table 5.3 where, e.g., the number of α phases in the unmodified alloy decreases from 68 to 4 in the Sr-modified high-purity alloy.

However, Sr promotes formation of the δ phase, which was found to form at the boundaries of the eutectic cells.

Sr modification of the eutectic Si in the commercial alloy increases the number density of δ phases but their average sizes are smaller. However, Sr was found to suppress the formation of the β phase. According to typical cooling curves of similar alloys [71], the addition of Sr to a commercial alloy results in an increase in recalescence, which is probably the reason that the β phase cannot form in the current Sr modified commercial alloy. This is similar to another report [28], which claims that Sr slightly depresses the precipitation temperature of the binary reaction β phase.

6.2.2 Effect of impurities on Al-10Si-0.3Fe-based alloys

In comparison to the unmodified high-purity alloy and the unmodified commercial alloy, impurities indeed have an effect, not only on the types of intermetallics, but also on their sizes. The sizes of the intermetallic phases are much larger in the commercial alloy than in the high-purity alloy as illustrated in Fig. 5.18a and 5.18c, Fig. 5.19a and 5.19c. As discussed in section 6.2.1, the impurities seem to play an effective role in the nucleation of the eutectic grains, which seems to be advantageous for the formation of the coarse β phase. The nucleation of the β phase occurs prior to the eutectic Al-Si solidification, as has been already discussed in section 6.1 based on the in-situ observations. The β phase nucleates at a higher temperature than the eutectic Al-Si phases. Growth of the β phase is initially very rapid up to the point where it is retarded by surrounding phases as already shown in section 6.1. Sr additions change the growth mode of the eutectic Al-Si and thereby also the nucleation of the β phase in such a way that formation of the δ phase is favored to the β phase.

There is no significant difference between the Sr-modified high-purity alloy and the Sr-modified commercial alloy. Only the sizes of the intermetallics in the Sr-modified commercial alloy are larger than in the Sr-modified high-purity alloy. These results indicate that the Sr in the high-purity alloy and the commercial alloy does not have a distinct effect on the intermetallics despite the presence of impurities in the commercial alloy.

It was reported previously [62, 63, 66] that oxides or oxide bi-films are the nucleation sites for the eutectic Si. Others reported that AlP particles cause the nucleation of the eutectic Si in Al-Si alloys. However, in a recent study [111], no increase in the number of β plates was observed with the addition of P, nor were AlP particles found along the β plates not even at

100 ppm P in the alloy. It has also been reported that in small concentrations the modifier Sr can deactivate AlP as a nucleant for Si, and in larger concentrations it can even deactivate the oxides, leaving Si to be formed by an unknown nucleus at significantly lower temperatures [25]. Campbell has claimed that “these mechanisms suggest the interesting prediction that for clean metal containing neither P nor oxides, the Al-Si alloys will be automatically modified without the intervention of Na or Sr” [25]. However, based on the comparison of the current alloys in this work, the eutectic Si in the unmodified high-purity alloy is still plate-like, unlike fine fibers or a coral structure, which is also supported by the previous study [71]. Campbell’s suggestion [25] is not consistent with the experiment reported here.

6.2.3 Formation of α and γ intermetallics

It should be mentioned that the γ intermetallic phase was found to be new and its structure was calculated in details for the first time in the present work in sections 5.1.3.1.1 and 5.1.3.1.2. The phase called τ_2 [46], known in the literature, is of similar composition but has another structure. The Fe-rich γ phase was determined to have a trigonal R-centered crystal structure with hexagonal lattice parameters $a = 1.034(5)$ nm, $c = 1.983(8)$ nm, $V = 1.836(25)$ nm³.

It is reported that the α phase exhibits a separate blocky structure and a convoluted branched structure in 3D [19, 29, 34]. Dinnis et al. [34] explain that the blocky structure of the α phase forms before the Al dendrites begin to solidify while the convoluted branched structure of the α phase forms after the Al dendrites have begun to solidify. In addition, Gorny et al [29] observe two distinct morphologies of the α phase: a large and bulky morphology and a finer “Chinese script” morphology. Their explanation is that the α phase, which exhibits a large and bulky morphology, forms prior to the eutectic reaction and the α phase, which exhibits the finer “Chinese script” morphology, forms during the eutectic reaction. Based on the observation that the α phase exhibits thin sheets aligned along the surfaces of the Si plates and often connects different Si plates along the interfaces of two eutectic Al grains, Timpel et al. [19] proposed that the α phase forms in isolated pockets among adjacent eutectic Al-Si plates in the last solidification stage, and the morphology of the α phase depends on the flat Si interface and the necking caused by the growing polycrystalline Al–Al interfaces.

Beside the α / γ intermetallic phases with “Chines script” morphology, much larger intermetallic phases of blocky structure have been found in the present work. Observation of

the modified commercial alloy by FIB tomography indicates four possible locations of the α / γ intermetallics:

- 1) inside the eutectic Si;
- 2) partially embedded in the eutectic Si;
- 3) attached to the eutectic Si;
- 4) embedded in the eutectic Al.

These observations strongly indicate there is some time span between the formation of the α / γ intermetallics. It is suggested that all four types of α / γ phases nucleate at the earlier stages of solidification, prior to the nucleation of the eutectic Al-Si phases. However, those types of α / γ phases with blocky morphology shown in Fig. 5.17 are not dominant in all investigated alloys.

It is hard to say whether the intermetallics formed at the earlier stages of the eutectic Si are γ phases or not since the number of γ phase in all four alloys observed by FIB tomography is low. This seems to be consistent with observation by TEM.

6.2.4 Formation of δ intermetallics

The δ phase is not always observed to form in all four investigated alloys. At a low cooling rate such as 1 K/min, the δ phase nucleates in the Fe-rich region rejected by the eutectic in the cell encircled by the eutectic Al-Si, during which the eutectic is growing simultaneously in the cell. The growing of the δ phase is probably constrained by the growing of the eutectic. The in-situ synchrotron observations in 4D, which shows that the eutectic Si restricts the growth of the δ platelets, is in good agreement with the results obtained by FIB tomography, which display the eutectic Si always surrounded by δ platelets. If there is a slight difference, it might be because formation process is much faster at high cooling rates since features such as collision impressions of the δ phase and the eutectic are more pronounced.

Another interesting observed phenomenon is that the eutectic Si, which is surrounded from two sides by δ plates, has a higher tendency to orientation in the Sr-modified high-purity alloy than in the Sr-modified commercial alloy, which is probably due to different nucleation mechanisms of the eutectic Si in the Sr modified commercial alloy. The latter has more diversity than in the Sr-modified high-purity alloy.

Some pores and Al lines can be frequently found in the δ plates as shown in Fig. 5.16. The diameter of Al crack lines in Fig 5.16 is less than 200 nm. In contrast, the estimated size of the eutectic Al is more than 400 nm, thus it does not seem as if the eutectic Al penetrate the δ plates. It can be suggested that the Al crack lines or pores are formed during casting due to shrinkage or hot tear, structural shrinking stress or thermal stress. As long as the surrounding part is still liquid, Al fills these cracks, but after the surrounding part has solidified, the crack will become a pore. Casting porosity and shrinkage defects have also been observed by Lu and Dahle [111]. Their interpretation is that the porosity is strong dependent on the composition of the alloy and the cooling rate. The high Fe level leads to a higher porosity and the high amount of Si suppresses the formation of coarse intermetallics and increases the volume fraction of eutectic Si and thereby improves castability [111]. The hypothesis [111] that the pores form at the end of the solidification is supported by the current work as described in section 6.1.

6.2.5 Formation of β intermetallics

As presented in chapter 5.1, the Fe-rich β phase was found in the as-cast unmodified commercial alloy only. The effect of impurities has already been discussed in section 6.2.2, since the difference between the commercial alloy and the high-purity alloy is the presence of impurities. The growth rate of eutectic Al-Si grains is most likely the reason for the absence of the β phase in the unmodified high purity alloy. Sr can suppress the formation of the β phase by increasing the recalescence and depressing the precipitation temperature of the binary β phase.

6.3 Effect of cooling rates on the formation of the intermetallic phases

Cooling conditions can also influence the formation of intermetallics. It has been reported [112, 113] that the formation of Fe-containing intermetallics in Al-Si alloys can be suppressed, refined or modified using rapid solidification processes, which is supported by the present results when ex-situ and in-situ solidification experiments are compared. Fig. 5.19 and Fig. 5.21 show the distinct sizes of Fe-rich intermetallics formed at a fast cooling and a slow cooling rate, respectively. The predominant difference between the fast cooling rate and the slow cooling rate in this work is the refinement and the suppression of the Fe-rich intermetallics during fast cooling.

Liu et al. [108] reported that the smaller dendritic arm spacing (DAS) obtained at a high cooling rate could physically restrict the growth of an intermetallic in the interdendritic spaces, reducing the final length of the intermetallics. However, the short diffusion time during fast cooling does not play a minor role in the size of the intermetallics. The diffusion length x can be easily estimated from the following equation:

$$x = 2(Dt)^{1/2} \quad (4)$$

where $D = D_0 \exp(-Q/RT)$, $Q = 276$ kJ/mol, $R = 8.314$ J/molK (gas constant), $D_0 = 2.34 \times 10^{22}$ /s [114] and t is the time at a the given temperature.

At high cooling rates, segregation and diffusion of Fe is limited by time and thus the sizes of the intermetallics are expected to be smaller. The estimated diffusion length of Fe in the alloy, calculated according to equation (4) at 570°C after 1 min for a slow cooling rate of 1 K/min, exceeds 640 nm. At a high cooling rate of about 400 K/min it is only 32 nm, which is 20 times slower. Thus, the growth velocity and the final size of the intermetallic is controlled by the cooling rate.

At fast cooling conditions, as seen in Fig. 5.19, the formation of intermetallics in the investigated alloys is also influenced by impurities and Sr addition. In contrast, at slow cooling rates as seen in Fig. 5.21, the formation of intermetallics is similar for all investigated alloys, which is probably due to the long diffusion time, regardless of impurities and Sr modification.

7. Summary

Extensive microscopic investigations were performed on four Al-10Si-0.3Fe-based casting alloys (high-purity alloy with and without addition of 200 ppm Sr and the corresponding commercial alloys). The main goal of this study was to find out how the impurities and the addition of Sr influence the formation of Fe-rich intermetallic phases and the formation of the eutectic Si phase. A further objective of this study was to understand the influence of the cooling rate on the formation of intermetallic phases. The experimental work was focused on the three-dimensional analysis of Fe-rich intermetallic phases using tomographic methods on the micrometer scale such as imaging with a focused ion beam and with synchrotron X-ray tomography. The 3D analyses were supported by 2D studies using a combination of optical microscopy, scanning electron microscopy and transmission electron microscopy.

The experimental work was divided into three parts:

In the first part of the work all intermetallic phases were examined for their crystal structure and chemical composition. The crystal structure of the Fe-rich intermetallic phases was identified using selected-area electron diffraction in TEM and the chemical composition was measured using energy-dispersive X-ray spectroscopy. In total, four Fe-rich intermetallic phases (α , γ , δ , and β) have been identified.

The location and the distribution of the Fe-rich intermetallic phases within the eutectic Al-Si grains have been also investigated.

The results obtained in the first part with respect to the Fe-rich intermetallic phases and eutectic Al-Si in Al-10Si-0.3Fe casting alloys can be summarized as follows:

1. Beside the well-known bcc α intermetallic phase and tetragonal δ phase **a new γ phase** was found. The composition of the γ phase is $\text{Al}_{4.35}\text{FeSi}$, which is close to that of the β phase ($\text{Al}_{4.5}\text{FeSi}$), but the morphology of the γ phase looks like the one of the α intermetallic phase. It features a trigonal R-centred crystal structure with hexagonal lattice parameters $a = 1.034(5)$ nm, $c = 1.983(8)$ nm and $V = 1.836(25)$ nm³.

7 Summary

2. In the unmodified high-purity alloy, the dominant phase is the α phase. The γ phase was also found but with a lower density. α phases are distributed homogeneously in the eutectic Al-Si. No other intermetallic phases were found in this alloy.
3. In the Sr-modified high-purity alloy the dominant phase is the δ phase. However, both α and γ phases are also present in this alloy, with low number density.
4. No β phase was found in any of the high-purity alloys.
5. In the commercial alloy, all phases (α , γ , δ , and β) are present. The crystal structure of the β phase was found monoclinic, with lattice parameters $a = 0.6148$ nm, $b = 0.6145$ nm and $c = 2.0808$ nm and $\beta = 91^\circ$, and their composition was $\text{Al}_{4.7}\text{FeSi}$. However, no β phase was found in the commercial alloy with additions of Sr.
6. The eutectic Si in the unmodified high-purity alloy appears needle-like in 2D and is very fine, while in the unmodified commercial alloy it exhibits coarse needles of much larger sizes. Sr additions transform the eutectic Si to a very fine morphology in both the pure and the commercial modified alloys.

In the second part of the work, the morphology, size and location of the intermetallic phases have been investigated using FIB and X-ray synchrotron tomography. Ex-situ FIB and synchrotron tomographic measurements of all casting alloys were carried out at room temperature. The cooling rate of the castings was about 400 K/min.

FIB tomography results:

1. The real shape and morphology of the α and γ phases as investigated by FIB tomography show thin interconnected sheets inside the eutectic microstructure.
2. The individual α phases with a blocky morphology has also been identified, but with a lower number density than the thin interconnected sheets. Some of these phases have been found located closely to the eutectic Si or embedded into the eutectic Si phase.
3. The δ phase appears as platelets and is located at the boundaries of the eutectic Al-Si cells in the Sr-modified alloys.
4. The β phase has not been visualized by FIB tomography because of its large size.

Synchrotron tomography results:

1. The α and γ phases are very fine in the unmodified high-purity alloy.
2. Large δ and β platelets and much smaller α and γ phases have been found in the commercial alloy. The intermetallic phases in this alloy are not interconnected with each other.

3. In the Sr-modified high-purity and commercial alloys the number density of the Fe-rich intermetallic phases is much higher than in the commercial alloy. The modification of both the pure and the commercial alloys enhances the interconnection of the intermetallic phases.

The third part of the work deals with in-situ synchrotron tomographic measurements. Primarily, the nucleation and growth of the Fe-rich intermetallic β and δ phases has been followed during solidification by in-situ synchrotron measurements.

The samples were heated up to a processing temperature 666°C and slowly cooled down to 450°C . In order to follow the nucleation and growth of the Al dendrites, the intermetallic phases and the eutectic Al-Si phases, the cooling rate was decided to be as low as possible. All alloys were measured at low cooling rates: 1 K/min, 9 K/min and 30 K/min. Measurements with the higher cooling rate of 400 K/min, which nearly corresponds to the cooling rate during the commercial casting procedure, have also been performed. Unfortunately the nucleation and growth of the phases was too fast, in such a way that within ~ 0.5 minutes all events had occurred. Surprisingly, in all four alloys, the intermetallic phases are not significantly different at cooling rates between 1 K/min and 30 K/min. The intermetallic phases are coarse at all (1 K/min, 9 K/min, 30 K/min) cooling rates. However, modification of the eutectic Si with Sr additions was found to depend not only on the cooling rate, but also strongly on the composition of the alloy. While the commercial alloy at 1 K/min cooling rate shows no modification of the eutectic Si, the high-purity alloy indicates a mixed (flakes and fibrous) structure. The reason is most probably the evaporation of Sr during the slow cooling of the melt because the samples were kept for too long at high temperatures. The slower the cooling rate the higher evaporation and oxidation of the Sr is as estimated in this study.

However, the main goal of the present work focused on the formation of the intermetallic phases. Because all investigated samples indicated similar sizes, distributions and densities of the intermetallic phases, the studies concentrated on nucleation and growth of the β and δ phases during solidification in the commercial alloy only, because it is representative for all other alloys. The results of the in-situ tomographic measurements at slow cooling rates (1 K/min-30 K/min) are as follows:

1. The first phase which starts to solidify in the melt are α -Al dendrites.
2. The second solidified phase is the β phase which nucleates near the Al dendrite arms and not at the oxidised surface.

7 Summary

3. The next solidified phases are the eutectic Si and the eutectic Al, the last solidified around the eutectic Si phase.
4. The δ phase solidified in the supersaturated melt between the eutectic Al-Si grains. The existence of the **δ phase** was found **for the first time**. In the literature this phase was mistakenly treated as β phase.
5. The β and the δ phases initially nucleate as independent, individual plates; with time and due to their fast growth they collide and build a branched interconnected structure of the plates.
6. Due to the limitation of spatial resolution, small scaled α and γ phases can rarely be discerned in these measurements.
7. The initial growth rate of the Fe-rich intermetallic β and δ phases is very high within a narrow temperature range. It decreases significantly at the end of solidification because of their impingement with surrounding phases like α -Al dendrites or eutectic Al-Si or the outer oxide skin.

Another main attention of this study lay on the nucleation and growth behavior of the β phase. These are the main points of this study:

1. Generally, formation of the β phase depends on the cooling rate, the composition and the addition of a modifier (Sr).
2. A slow cooling rate promotes nucleation of the β phase in the high-purity alloy, in the commercial alloy and in the corresponding alloys with Sr addition. The β phase is coarse and independent of the alloy composition.
3. A fast cooling rate refines the β phase in the commercial alloy. No β phase was found in neither the high-purity nor the Sr-modified (high-purity and commercial) alloys.
4. Nucleation of the β phase takes place mainly in the supersaturated solute near or between the α -Al dendrite arms.
5. The importance of AIP as a nucleant for the β phase formation was not confirmed.
6. The β phase is not the direct nucleant for pore formation; however, they are necessary contributors for the formation of pores.
7. The impurities in the commercial alloy promote a faster evaporation and oxidation of Sr. The commercial alloys need a higher amount of Sr than the high-purity alloys in order to modify the eutectic Si.

Since the coarse β phases markedly degrade mechanical properties and give rise to casting defects the main conclusion from this study is:

The finer the β phase the fewer pores (defects) can form and the density of the pores is lower. This is due to the melt's permeability for hydrogen (source of the pore) during solidification, which is an important factor for the industry.

References

- [1] J.R. Davis (editor) (1993) Aluminum and aluminum alloys. ASM International, Ohio
- [2] T. Hosch, R.E. Napolitano, The effect of the flake to fiber transition in silicon morphology on the tensile properties of Al–Si eutectic alloys, *Mater. Sci. Eng. A* 528 (2010) 226-232
- [3] A. Couture, Iron in aluminum casting alloys - A literature survey. *AFS Int. J. Cast. Met.* 6 (1981) 9-17
- [4] L. Bäckerud, G. Chai, J. Tamminen, Solidification Characteristics of Aluminum Alloys, *Foundry Alloys*, vol. 2, AFS/Skanaluminum (1990) 71-84
- [5] W. Khalifa, F.H. Samuel, J.E. Gruzleski, Iron intermetallic phases in the corner of the Al-Si-Fe system, *Metall. Mater. Trans. A* 34A (2003) 807-825
- [6] J.A. Taylor, G.B. Schaffer, D.H. StJohn, The role of iron in the formation of porosity in Al-Si-Cu-based casting alloys: Part I. Initial experimental observations, *Metall. Mater. Trans. A* 30A (1999) 1643-1650
- [7] S. Yaneva, N. Stoichev, Z. Kamenova and S. Budurov, Quaternary Iron-Containing Phases in Al-Si Cast Alloys, *Z. Metallkd.* 75 (1984) 395-398
- [8] S.P. Gupta, Intermetallic compound formation in Fe-Al-Si ternary system: Part I. *Mater. Charact.* 49 (2003) 269-291
- [9] T. Maitra, S.P. Gupta, Intermetallic compound formation in Fe-Al-Si ternary system: Part II. *Mater. Charact.* 49 (2003) 293–311
- [10] M. Timpel, N. Wanderka, R. Grothausmann, J. Banhart, Distribution of Fe-rich phases in eutectic grains of Sr-modified Al-10wt%Si-0.1wt% Fe casting alloy, *J. Alloy & Comp.* 558 (2013) 18-25

References

- [11] M.V. Kral, A crystallographic identification of intermetallic phases in Al-Si alloys, *Mater. Lett.* 59 (2005) 2271-2276
- [12] J. Murray, A.J. McAlister, The Al-Si (aluminum-silicon) system. *Bull Alloy Phase Diagr.* 5 (1984) 74-84
- [13] A.K. Dahle, K. Nogita, S.D. McDonald, C. Dinnis, L. Lu, Eutectic modification and microstructure development in Al-Si Alloys, *Mat. Sci. & Eng. A* 413-414 (2005) 243-248
- [14] J.A. Taylor, Iron-Containing Intermetallic Phases in Al-Si Based Casting Alloys, *Procedia Mater. Sci.* 1 (2012) 19-33
- [15] J.E. Tibballs, Al-Si substitution in Al(Fe, Mn)Si phases, *Key Eng. Mater.* 44-45 (1990) 233-246
- [16] M.H. Mulazimoglu, A. Zaluska, J.E. Gruzleski, F. Paray, Electron Microscope study of Al-Fe-Si intermetallics in 6201 Aluminum Alloy, *Metall. Mater. Trans. A* 27A (1996) 929-936
- [17] J.G. Zheng, R. Vincent, J.W. Steeds, Crystal structure of an orthorhombic phase in β -(Al-Fe-Si) precipitates determined by convergent-beam electron diffraction, *Philos. Mag. A* 80 (2000) 493-500
- [18] M.V. Kral, H.R. McIntyre, M.J. Smillie, Identification of intermetallic phases in a eutectic Al-Si casting alloy using electron backscatter diffraction pattern analysis, *Scripta Mater.* 51 (2004) 215-219
- [19] M. Timpel, N. Wanderka, B.S. Murty, J. Banhart, Three-dimensional visualization of the microstructure development of Sr-modified Al-15Si casting alloy using FIB-EsB tomography, *Acta Mater.* 58 (2010) 6600-6608
- [20] M.G. Day, A. Hellawell, The Microstructure and Crystallography of Aluminium-Silicon Eutectic Alloys, *P. Roy. Soc. A* (1968) 473-491
- [21] C. Rømming, V. Hansen, J. Gjønnes, Crystal Structure of β -Al_{4.5}FeSi, *Acta Crystallogr. B* 50 (1994) 307-312
- [22] V. Hansen, B. Hauback, M. Sundberg, Chr. Rømming, J. Gjønnes, β -Al_{4.5}FeSi: A combined synchrotron powder diffraction, electron diffraction, high-Resolution electron microscopy and single-crystal X-ray diffraction study of a faulted structure, *Acta Crystallogr. B* 54 (1998) 351-357

- [23] P.J. Black, XLIX. Brillouin Zones of some intermetallic compounds, *Philos. Mag.* 46 (1955) 401-409
- [24] G.J.C. Carpenter, V.L. Page, Revised cell data for the β -FeAlSi phase in aluminum alloys, *Scr. Metall. Mater.* 28 (1993) 733–736
- [25] J. Campbell, Discussion of “effect of strontium and phosphorus on eutectic Al-Si nucleation and formation of β -Al₅FeSi in hypoeutectic Al-Si foundry alloys”, *Metall. Mater. Trans. A* 40A (2009) 1009-1010
- [26] S. G. Shabestari, M. Mamudi, M. Emamy, J. Campbell, Effect of Mn and Sr on intermetallics in Fe-rich eutectic Al-Si alloy. *Int. J. Cast. Met. Res.* 15 (2002) 17-24
- [27] A.M. Samuel, A. Pennors, C. Villeneuve, F.H. Samuel, H.W. Doty, S. Valtierra, Effect of cooling rate and Sr-modification on porosity and Fe-intermetallics formation in Al-6.5% Si-3.5% Cu-Fe alloys. *Int. J. Cast, Met. Res.* 13 (4) (2000)231-253
- [28] L. Lu, A.K. Dahle, Iron-rich intermetallic phases and their role in casting defect formation in hypoeutectic Al-Si alloys, *Metall. Mater. Trans. A* 36A (2005) 819-835
- [29] A. Gorny, J. Manickaraj, Z. Cai, S. Shankar, Evolution of Fe based intermetallic phases in Al–Si hypoeutectic casting alloys: Influence of the Si and Fe concentrations, and solidification rate, *J. Alloys & Comp.* 577 (2013) 103–124
- [30] A.L. Dons, Superstructures in alpha-Al(Mn,Fe,Cr)Si, *Z. Metallkd.* 76(2) (1985) 151-153
- [31] S.G. Shabestari, J.E. Gruzleski, Modification of iron intermetallics by strontium in 413 aluminum alloys, *AFS Trans.* 103 (1995) 285-293
- [32] F.H. Samuel, A.M. Samuel, H.W. Doty, S. Valtierra, Decomposition of Fe-intermetallics in Sr-modified cast 6XXX type aluminum alloys for automotive Skin. *Metall. Mater. Trans. A* 32A (2001) 2061-2075
- [33] A. Samuel, F. Samuel, H. Doty, S. Valtierra, Metallographic observations of β -AlFeSi phase and its role in porosity formation in Al–7%Si alloys, *Int. J. Cast. Met. Res.* 19 (2006) 156-166
- [34] C.M. Dinnis, J.A. Taylor, A.K Dahle, As-cast morphology of iron-intermetallics in Al–Si foundry alloys, *Scripta Mater.* 53 (2005) 955-958

References

- [35] F. Lasagni, A. Lasagni, C. Holzappel, F. Mücklich, H.P. Degischer, Three dimensional characterization of unmodified and Sr-modified Al-Si eutectics by FIB and FIB/EDX tomography, *Advanc. Eng. Mater.* 8 (2006) 719-723
- [36] F. Lasagni, A. Lasagni, E. Marks, C. Holzappel, F. Mücklich, H.P. Degischer. Three dimensional characterization of “as-cast” and solution-treated AlSi12(Sr) alloys by high-resolution FIB tomography, *Acta Mater* 55 (2007) 3875-3882
- [37] J.M. Yu, N.Wanderka, G. Miede, J. Banhart, Intermetallic phases in high-purity Al-10Si-0.3Fe cast alloys with and without Sr modification studied by FIB tomography and TEM, *Intermetallics*, 72 (2016) 53-61
- [38] P. Mikołajczak, L. Ratke, X-ray tomography investigations of Fe-rich intermetallics in AlSi alloys, *Archives of Foundry Eng.* 13 (2013) 79-82
- [39] N. Limodin, L. Salvo, E. Boller, M. Suéry, M. Felberbaum, S. Gaillière, K. Madi, In-situ and real-time 3-D microtomography investigation of dendritic solidification in an Al-10 wt.% Cu alloy, *Acta Mater.* 57 (2009) 2300-2310
- [40] C. Puncreobutr, A.B. Phillion, J.L. Fife, P. Rockett, A.P. Horsfield, P.D. Lee, In-situ quantification of the nucleation and growth of Fe-rich intermetallics during Al alloy solidification, *Acta Mater.* 79 (2014) 292–303
- [41] R. H. Mathiesen, L. Arnberg, Y. Li, V. Meier, P. Schaffer, I. Snigireva, A. Snigirev, A.K. Dahle. X-Ray videomicroscopy studies of eutectic Al-Si solidification in Al-Si-Cu, *Metall. Mater. Trans. A* 42A (2011) 170-180
- [42] S. Terzi, J.A. Taylor, Y.H. Cho, L. Salvo, M. Suéry, E. Boller, A.K. Dahle. In-situ study of nucleation and growth of the irregular α -Al/ β -Al₃FeSi eutectic by 3-D synchrotron X-ray microtomography, *Acta Mater.* 58 (2010) 5370–5380
- [43] C. Kammer: *Aluminium-Taschenbuch*. Düsseldorf: Aluminium-Verlag, 2002
- [44] Z. Liu, Y.A. Chang, Thermodynamic Assessment of the Al-Fe-Si system, *Metall. Mater. Trans. A* 30A (1999) 1081-1095
- [45] Y. Du, J. C. Schuster, Z. Liu, R. Hu, P. Nash, W. Sun, etc. A thermodynamic description of the AlFeSi system over the whole composition and temperature ranges via a hybrid approach of CALPHAD and key experiments, *Intermetallics* 16 (2008) 554-570

-
- [46] N. Krendelsberger, F. Weitzer, J. C. Schuster, On the Reaction Scheme and Liquidus Surface in the Ternary System Al-Fe-Si, *Metall. Mater. Trans. A* 38A (2007) 1681-1691
- [47] V. Raghavan, Al-Fe-Si (Aluminum-Iron-Silicon), *J. Phase Equilibria and Diffusion* 23 (2002) 362–366
- [48] H.P. Takeda and K. Mutuzaki, The Equilibrium Diagram of the Iron-Aluminium-Silicon System, *Tetsu to Hagane*, 26 (1940) 335-361
- [49] V. Rivlin, G.V. Raynor, Critical evaluation of constitution of aluminium–iron–silicon system, *Int. Met. Rev.* 3 (1981) 133–152
- [50] S. Pontevichi, F. Bosselet, F. Barbeau, M. Peronnet, J.C. Viala, Solid-Liquid Phase Equilibria in the Al-Fe-Si System at 727 °C, *J. Phase Equilibria & Diffusion* 25 (2004) 528-537
- [51] G. Ghosh and MSIT, Al-Fe-Si Ternary Phase Diagram Evaluation, in: G. Effenberg (ed.) *MSI Eureka in Springer Materials* (2007)
- [52] M. Rappaz, Modelling of microstructure formation in solidification processes, *International Materials Reviews* 34 (1989) 93–123
- [53] S.D. McDonald, Eutectic Solidification and Porosity Formation in Unmodified and Modified Hypoeutectic Aluminium-Silicon Alloys, PhD thesis, Queensland, Australia, 2002
- [54] P. Thevoz, J. L. Desbiolles, M. Rappaz, Modeling of equiaxed microstructure formation in casting, *Metall. Trans. A* 20 (1989) 311–322
- [55] S.D. McDonald, A.K. Dahle, J.A. Taylor, D.H. StJohn, Eutectic Grains in Unmodified and Strontium-modified Hypoeutectic Aluminum-Silicon Alloys, *Metall. Mater. Trans. A* 35A (2004) 1829–1837
- [56] X.-G. Chen, Crystallization of the aluminum-silicon-eutectic and application of the thermal analysis for controlling the processing, PhD thesis, RWTH Aachen, Germany, 1990
- [57] Y.S. Choi, J.S. Lee, W.T.Kim, H.Y. Ra, Solidification behaviour of Al-Si-Fe alloys and phase transformation of metastable intermetallic compound by heat treatment, *J. Mater. Sci.* 34 (1999) 2163-2168
- [58] M. Cooper, K. Robinson, The crystal structure of the ternary alloy α (AlMnSi), *Acta Crystallogr.* 20 (1966) 614-617

References

- [59] H.W.L. Phillips, Annotated equilibrium diagrams of some aluminium alloy systems (monograph No.25), London (Inst. Metals) (1959) 25
- [60] K. Robinson, P. J. Black, An X-ray examination of an α (Al-Fe-Si) ternary compound, *Phil. Mag.* 44 (1953) 1392-1397
- [61] V. Elser, C.L. Henley, Crystal and quasicrystal structures in Al-Mn-Si alloys, *Phys. Rev. Lett.* 55 (1985) 2883
- [62] X. Cao, J. Campbell, The nucleation of Fe-rich phases on oxide films in Al-11.5Si-0.4Mg cast alloys, *Metall. Mater. Trans. A* 34A (2003)1409-1420
- [63] L.A. Narayanan, F.H. Samuel, J.E. Gruzleski, Crystallization behavior of iron-containing intermetallic compounds in 319 aluminum alloy. *Metall Mater Trans A* 25A (1994) 1761-1773
- [64] W. Rosenhain, S.L. Archbutt. D. Hanson. Eleventh Report to the Alloys Research Committee of the Institution of Mechanical Engineers. Alloys Research Committee; National Physical Laboratory (Great Britain) (1921)
- [65] G. Sigworth, J. Campbell, The modification of Al-Si casting alloys: important practical and theoretical aspects. *Int. J. Metalcast.* 3 (2009) 65-74
- [66] Y.H. Cho, H.C. Lee, K.H. Oh, A.K. Dahle, Effect of Strontium and Phosphorus on Eutectic Al-Si Nucleation and Formation of β -Al₅FeSi in Hypoeutectic Al-Si Foundry Alloys. *Metall. Mater. Trans. A*, 39A (2008) 2008-2435
- [67] D.N. Miller, L. Lu, A.K. Dahle, The role of oxides in the formation of primary iron intermetallics in an Al-11.6Si-0.37Mg Alloy. *Metall. Mater. Trans. B* 37B (2006) 873-878
- [68] A.M. Samuel, F.H. Samuel, H.W. Doty, Observations on the formation of β -Al₅FeSi phase in 319 type Al-Si alloys. *J. Mater. Sci.* 31(1996) 5529-5539
- [69] B. Kim, S. Lee, S. Lee, H. Yasuda, Real-time radiographic observation of solidification of solidification behavior of Al-Si-Cu casting alloys with the variation of iron content. *Mater. Trans.* 53 (2012) 374-379
- [70] A.K. Dahle, K. Nogita, J.W. Zindel, S.D. McDonald, L.M. Hogan, Eutectic nucleation and growth in hypoeutectic Al-Si alloys at different strontium levels. *Metall. Mater. Trans. A* 32A (2001) 949-960

-
- [71] S.D. McDonald, K. Nogita, A.K. Campbell, Eutectic nucleation in Al-Si alloys. *Acta Mater.* 52 (2004) 4273-4280
- [72] M. Timpel, N. Wanderka, R. Schlesiger, T. Yamamoto, N. Lazarev, D. Isheim, G. Schmitz, S. Matsumura, J. Banhart. The role of strontium in modifying aluminium-silicon alloys, *Acta Mater.* 60 (2012) 3920-3928
- [73] M. Timpel, N. Wanderka, R. Schlesiger, T. Yamamoto, D. Isheim, G. Schmitz, S. Matsumura, J. Banhart, Sr-Al-Si co-segregated regions in eutectic Si phase of Sr-modified Al-10Si alloy. *Ultramicroscopy* 132 (2013) 216-221
- [74] J. Barrirero, M. Engstler, N. Ghafoor, N. de Jonge, M. Oden, F. Mücklich, Comparison of segregations formed in unmodified and Sr-modified Al-Si alloys studied by atom probe tomography and transmission electron microscopy. *J. Alloys & Compd.* 611 (2014) 410-421
- [75] A.M. Samuel, F.H. Samuel, C. Villeneuve, H.W. Doty and S. Valtierra, Effect of trace elements on β -Al₅FeSi characteristics, porosity and tensile properties of Al-Si-Cu (319) cast alloys. *Int. J. Cast Metals Res.* 14 (2001) 97-120
- [76] C. Villeneuve and F.H. Samuel, Modification of iron intermetallics by magnesium and strontium in Al-Si alloys. *Int. J. Cast Met. Res.* 12 (1997) 145-160
- [77] Manual Smart SEM V 5.00. Manual for the SUPRA (VP) and ULTRA Scanning Electron Microscope, (2005)
- [78] Carl Zeiss SMT-Nano technology systems division, Zeiss Ultra 55 & Ultra 60. http://www.pro-4-pro.com/media/product/12508/attachment_en-1398244596.pdf
- [79] Principle of TEM. http://www.hk-phy.org/atomic_world/tem/tem02_e.html
- [80] H. Zhang, What limits the application of TEM in the semiconductor industry?, *Thin Solid Films* 320 (1998) 77-85
- [81] Principle of Focused ion beam. https://en.wikipedia.org/wiki/Focused_ion_beam
- [82] L. Holzer and M. Cantoni. Review of FIB Tomography in Nanofabrication Using Focused Ion and Electron Beams: Principles and Applications. Oxford University Press, Oxford, UK (2012) 410-435
- [83] Template Matching and Slice Alignment- ImageJ Plugins. <http://sites.google.com/site/qingzongtseng/template-matching-ij-plugin>

References

- [84] L. A. Giannuzzi and F.A. Stevie. Introduction to Focused Ion Beams. New York, Springer, (2005)
- [85] G. Margaritondo. Elements of Synchrotron Light: For Biology, Chemistry, and Medical Research. Oxford University Press, (2002)
- [86] M. H. R. Donald, M. R. Harold, N. M. King, B. G. Loach, J. R. M. Maidment, C. W. Planner, G. H. Rees, and J. V. Trotman. A Superconducting Synchrotron Design Study at the Rutherford Laboratory. IEEE Transactions on Nuclear Science 18 (1971)
- [87] H.A. Barnett. Chemical analysis of polymer blends via synchrotron X-ray tomography. PhD Dissertation. Louisiana Tech University. (2008)
- [88] Parameters of Accelerators of ESRF. <http://www.esrf.eu/Accelerators/Accelerators/>
- [89] D. J. Thompson, R. Coisson, M. Ericksson, J. Leduff, A. Hofmann, D. Husmann, G. Mulhaupt, M. W. Poole, M. Renard, M. Sommer, V. P. Suller, S. Tazzari, and F. H. Wang. The All Wiggler Synchrotron Radiation Source. IEEE Transactions on Nuclear Science 28 (1981) 3153-3155
- [90] Salvo, L., P. Cloetens, E. Maire, S. Zabler, J.J. Blandin, J.Y. Buffiere, W. Ludwig, E. Boller, D. Bellet, and C. Josserond, X-ray micro-tomography an attractive characterisation technique in materials science. Nuclear Instruments & Methods in Physics Research Section B- Beam Interactions with Materials and Atoms 200 (2003) 273-286
- [91] P. A. Douissard, A. Cecilia, X. Rochet, X. Chapel, T. Martin T. van de Kamp, L. Helfen, T. Baumbach, L. Luquot, X. Xiao, J. Meinhardt, and A. Rack. A versatile indirect detector design for hard X-ray microimaging, Journal of Instrumentation 7 (2012) P09016, 1-26
- [92] Reconstruction program performing by pyHST (High Speed Tomography in python version) software. http://www.esrf.eu/UsersAndScience/Experiments/Imaging/ID19/micro_tomography/computing_duringexperiment/toto
- [93] A.L. Dons, Superstructures in alpha-Al(Mn,Fe,Cr)Si, Z. Metallkd. 76 (2) (1985) 151-153
- [94] Y. Komura, W.G. Sly, D.P. Shoemaker, The crystal structure of the R phase, Mo-Co-Cr, Acta Crystallogr. 13 (1960) 575-585
- [95] S. Samson, E.K. Gordon, The crystal structure of ϵ -Mg₂₃Al₃₀, Acta Crystallogr. B24 (1968) 1004-1013

-
- [96] C.B. Shoemaker, D.P. Shoemaker, Refinement of an R phase, $Mn_{85.5}Si_{14.5}$, *Acta Crystallogr. B* 34 (1978) 701-705
- [97] S. Rideout, W.D. Manly, E.L. Kamen, B.S. Lement, P.A. Beck, Intermediate Phases in Ternary Alloy Systems of Transition Elements, *Trans. Amer. Inst. Min. (Metall.) Eng.* 191 (1951) 872-876
- [98] M.V. Kral, P.N.H Nakashima, D.R.G. Mitchell, Electron Microscope studies of Al-Fe-Si intermetallics in an Al-11Pct Si alloy, *Metall. Mater. Trans. A* 37A (2006) 1987-1997
- [99] G. Sha, K. Sha, B. Cantor. Characterization of Fe-rich intermetallic phases in a 6xxx series Al alloy, *Mater. Sci. Forum* 519–521 (2006) 1721-1726
- [100] G.K. Sigworth, The modification of Al–Si casting alloys: important practical and theoretical aspects, *Int. J. Metal cast.* 2 (2008) 19–40
- [101] C. Liao, J. Chen, Y. Li, H. Chen, C. Pan, Modification performance on 4032 Al alloy by using Al-10Sr master alloys manufactured from different processes, *Progress in Natural Science: Materials International* 24 (2014) 87-96
- [102] J. Wang, P.D. Lee, R.W. Hamilton, M. Li, J. Alison, The kinetics of Fe-rich intermetallic formation in aluminium alloys: In situ observation. *Scripta Mater.* 60 (2005) 516-519
- [103] J. Wang, M. Li, J. Allison, P.D. Lee, Multiscale modeling of the influence of Fe content in a Al-Si-Cu alloy on the size distribution of intermetallic phases and micropores, *J. Appl. Phys.* 107 (2010) 061804, 1-8
- [104] W. Khalifa, F.H. Samuel, J.E. Gruzleski, H.W. Doty, S. Valtierra, Nucleation of Fe-intermetallic phases in the Al-Si-Fe alloys, *Metall Mater Trans A*, 36A (2005) 1017-1032
- [105] C. Puncreobutr, P.D. Lee, K.M. Kareh, T. Connolley, J.L. Fife, A.B. Phillion, Influence of Fe-rich intermetallics on solidification defects in Al–Si–Cu alloys. *Acta Materialia* 68 (2014) 42–51
- [106] N. Roy, A.M. Samuel, F.H. Samuel. Metall. Porosity formation in Al-9 wt Pct Cu alloy system: metallographic observations. *Mater. Trans. A* 27 (1996) 415-429.
- [107] L.A. Narayanan, F.H. Samuel, Thermal analysis studies on the effect of cooling rate on the microstructure of the 319 aluminium alloy. *AFS Trans.*, 100 (1992) 383-391.

References

- [108] L. Liu, A. M. A. Mohamed, A. M. Samuel, F. H. Samuel, H. W. Doty, S. Valtierra, Precipitation of β -Al₅FeSi phase platelets in Al-Si based casting alloys. *Metall. Mater. Trans. A* 40A (2009) 2457-2469
- [109] P. Ashtari, H. Tezuka, T. Sato, Influence of Sr and Mn additions on intermetallic compound morphologies in Al-Si-Cu-Fe cast alloys. *Mater. Trans.* 44 (2003) 2611-2616
- [110] L.M. Hogan, H. Song, Aluminium grains structures in Al-Si eutectic alloys, *Acta Metal.* 35 (1987) 677-680
- [111] S. Lu, A. Hellawell, The mechanism of Si modification in Aluminium-Silicon Alloys: Impurity induced twinning, *Metall. Mater. Trans. A* 18A (1987) 1721-1733
- [112] A. K. Srivastava, V. C. Srivastava, A. Gloter, S. N. Ojha, Microstructural features induced by spray processing and hot extrusion of an Al-18% Si-5% Fe-1.5% Cu alloy. *Acta Mater* 54 (2006) 1741-1748
- [113] J. Li, M. Zarif, P. Schumacher, TEM investigation of a novel Fe-containing phase in high purity Al-Si-Fe alloys. *BHM Berg-Huttenmann Monatsh* 155 (2010) 499-505
- [114] D. Naoi, M. Kajihara, Growth behavior of Fe₂Al₅ during reactive diffusion between Fe and Al at solid-state temperatures. *Mater. Sci. & Eng. A* 459 (2007) 375-382

Acknowledgements

I am deeply grateful to Prof. John Banhart, who gave me the opportunity to pursue my PhD at the Institute of Applied Materials of the Helmholtz-Zentrum Berlin für Materialien und Energie (HZB) and partly financial support during my PhD. I would like to thank the second examiner Prof. Dieter Herlach from German Aerospace Center (DLR), who is ready to examine my thesis. I would like to express my greatest gratitude to Dr. Nelia Wanderka, who guided me through the palace of science during my PhD. She is a great scientist. She also trained me to operate TEM with her professional skills and rich experience, and she always headed me in time when I was about to be lost with her patience, her encouragement, her enthusiasm, and her great efforts as well as her inspiration, which I really appreciate.

My sincere thanks also go to Dr. Gerhard Mieke from TU-Darmstadt for the excellent analysis of SAED patterns. I would also like to thank Dr. Anna Manzoni and Dr. Florian Vogel in our group for their kind assistance in performing synchrotron tomography experiment at ESRF. I am especially grateful to Dr. Anna Manzoni, who gave me thousand times of helps. I also would like to thank Dr. Florian Vogel, who taught me how to process images using photoshop. I would like to thank Mr. Holger Kropf for the help of FIB tomography experiment, and Mrs. Christiane Förster for the help of TEM sample preparation, and Mrs. Claudia Leistner for using cutting machine in her lab and the help of DSC experiment.

My gratitude also goes to Mr. Manuel Wüstenhagen from TU Berlin, who helped me together make an excellent programming to run macro which indeed saved a lot of time to process massive data. I also would like to thank Mr. Jörg Bajorat for always solving the computer problems in time, and Mrs Annette Friedrich and Mrs Manfred Wiencken from HZB library department for providing and ordering literatures that I needed. I would like to thank Mrs. Christiane Ciceron for the help of documents management.

I also would like to acknowledge the experiment condition provided by European Synchrotron Radiation Facility and the help from the scientists at beamline ID 19 at ESRF. Particularly, I would like to thank Dr. Alexander Rack for the help of synchrotron

Acknowledgements

tomography experiment at ESRF and all the arrangement during the period of experiment and data processing. My gratitude also goes to Dr. Remi Daudin for lots of help of data processing, and Mrs Elodie Boller for the help of this experiment, especially for optimizing parameters for in-situ measurement.

My gratitude also goes to the excellent tomography group in our institute. Particularly, I would like to thank Dr. Manke Ingo, whose group helped me perform many valuable experiments at BESSY II for synchrotron tomography and also taught me valuable methods of data processing, for which I would like to express my gratitude to Dr. Henning Markötter, Dr. Tobias Arlt, Dr. Hilger Andre, Dr Kardjilov Nikolay, Mr. Markus Osenberg. I especially would like to express my appreciation to Dr. Henning Markötter for teaching me images processing methods with his patience and enthusiasm, and Dr. Tobias Arlt for his great help in performing in-situ synchrotron tomography work at ESRF.

My deepest gratitude goes to my parents for their long standing encouragement and support as well as their incessant love. I also would like to thank my girlfriend Ms Piao Xiangzi, who gave me lots of encouragement and supports.

I would like to thank my country and the Chinese Scholarship Council for giving me financial support during my PhD.

I would also like to thank all the people who gave me helps, supports and encouragements during my PhD period.

Berlin, 2016

Jiamin Yu

Declaration

Ich erkläre hiermit, dass ich diese Dissertation selbständig verfasst habe. Die benutzten Hilfsmittel und Quellen sind in der Arbeit vollständig angegeben. Ich habe weder früher noch gleichzeitig ein Promotionsverfahren bei einem anderen Fachbereich bzw. einer anderen Hochschule beantragt. Diese Arbeit hat in gleicher oder ähnlicher Form noch keiner Prüfungsbehörde vorgelegen.

Berlin, im September 2016

